Microscopic Studies On The Response Of Bio-Molecular Systems To Perturbations

Thesis submitted for the degree of

Doctor of Philosophy (Science)

in

Physics (Theoretical)

by

Anirban Paul

Department of Physics

University of Calcutta

2025

Dedicated to

Baba ...

Acknowledgement

After five and a half years at SNBNCBS, I am pleased to present my Ph.D. thesis. This journey has been both challenging and fulfilling, and I sincerely appreciate the support and encouragement I received from many individuals who played a crucial role in this accomplishment.

First, I express my heartfelt gratitude to my supervisor, Prof. Jaydeb Chakrabarti, for introducing me to the fascinating world of molecular simulations and guiding me throughout my Ph.D. His mentorship helped me develop independent thinking and shape my research. I am also grateful for the insightful discussions with him, through which I learned a great deal about statistical mechanics and soft-matter physics. His invaluable support and persistent push toward improvement have played a crucial role in my academic growth. Without his guidance completing my Ph.D. would have been immensely difficult. I am also grateful to my thesis committee members, Dr. Suman Chakrabarty and Dr. Gautam Gangopadhyay, for their valuable comments and suggestions. I would like to give special thanks to Dr. Suman Chakrabarty for his biomolecular simulation courses during our Ph.D. coursework, which helped me immensely in my research in later years. I sincerely acknowledge Dr. Tatini Rakshit for introducing me to the crucial role of Hyaluronic Acid in various biological phenomena. The experimental results from her lab provided insights that guided our theoretical investigations. Furthermore, I would like to express my gratitude to the Technical Research Centre for the CRAY supercomputing facility, which provided me with the necessary computing power to carry out my research. Special thanks to CSIR, India for providing me the Junior and Senior Research Fellowship for Ph.D. I would like to express my gratitude towards Prof. Shubhra Ghosh Dastidar, who served as the external examiner during my SRF viva.

I sincerely appreciate the wonderful soft-matter research group members who have supported me throughout my Ph.D. journey. I am grateful to my senior, Dr. Piya Patra, for her guidance during my initial days. I extend my heartfelt thanks to Rahul Da and Dr. Edwine Tendong for their invaluable guidance as group seniors. Discussions with them and attending their presentations during group meetings greatly enriched my knowledge. I would like to especially acknowledge my senior, Abhik Da, who patiently listened and provided unwavering support during challenging times, whether it was long research hours, writing papers, or handling peer reviews. Our scientific discussions and memorable tea-break conversations led to valuable ideas that significantly contributed to my research. I also sincerely thank Kanika di for patiently listening to my endless rants during the tough final phase of thesis writing. I thank my other group members, Suravi Di, Avik, Sabuj, and Anusree, for their wonderful companionship. I will truly miss our group lunches and dinners. I wish all of you great success in your careers. I would also like to acknowledge Krishnendu for his insightful discussions.

Now, I would like to mention those people without whom my five years at SNB would have been unimaginable. I am especially grateful to my friends Manodip, Kp da, Rik, and Samir for their unwavering companionship throughout my Ph.D. life. I was fortunate to share my *emotions, joys, and sorrows with them. They stood by me through all my ups and downs. I will always cherish our time spent together during lunch, dinner, outings, short trips, and of course, our late-night addas. Words are not enough to express how much I loved and enjoyed those moments. I have also spent my favorite moments with Ramkrishna and Samrat. A special mention to Tanmoy Da, my senior from school, M.Sc., and here at SNB. He guided and helped me immensely in many ways throughout this journey. I am also grateful to Srija for her constant support during my tough days, especially while working on my first paper and beyond. I would like to thank all my friends, seniors, and juniors from SNB sports. I thank Premasis Da, Shubham, Biswajit Panda, Sayan, Arnab, and Bivas, with whom I shared both fierce competition on the field and great companionship afterward. I wish each of you great success in your careers and future endeavors. Many thanks to Utpal Da for the tea and snacks at his shop and all the staff of SNB Mess for providing delicious meals.*

I am truly blessed to have a supportive family who has played a pivotal role in my life. I am deeply indebted to Dada, Shruti Di, and Chhorda for their unwavering support throughout my academic journey. I would also like to thank Didi, Manishda, Shilpi Boudi, Priti Di, and Surya Da. I am also profoundly grateful to Kaku and Chhotoma for their unconditional love and care. Finally, my deepest appreciation, respect, and love go to Maa and Baba. I owe them not only this thesis but everything in my life. Their love, sacrifices, and support have been the driving force behind all my achievements.

Finally, I would like to express my gratitude to the developers behind the open-source and free software that greatly facilitated my Ph.D. work. I am sure there are many others whose support contributed to the completion of this thesis. I regret that I cannot mention each and every individual by name, but I sincerely appreciate their help. My heartfelt thanks to everyone who has been part of this journey.

Anirban Paul
Department of Physics of Complex Systems
S. N. Bose National Centre for Basic Sciences
Salt lake, Kolkata-700106, India
2025.

Abstract

Biomolecules like proteins, lipids, and glycans are essential for biological processes in living organisms. The structure and function of a biomolecule are often altered in presence of external perturbations such as small ligands, the environment, external fields, and so on. These perturbations are important from biological phenomena to technologically important processes.

In the thesis, we investigate the elastic response of a model Dipalmitoylphosphatidylcholine (DPPC) lipid bilayer to Hyaluronic acid (HA) using all-atom molecular dynamics simulation. We find that in presence of short HA chains, the elastic modulus of the bilayer decreases implying the softening of the bilayer. We also investigate the dynamics at the interface of the HA-water and DPPC bilayer by computing the mean squared displacements (MSD). Subdiffusive MSD is observed when water molecules or HA chains are very close to the bilayer and diffusive MSD is found when they are slightly far away from the bilayer. In the diffusive region of the interface, the translational and rotational diffusions of water and HA chains decrease as HA concentration increases, whereas they remain almost the same as HA chain size varies. The weak chain size dependence of interfacial water dynamics is attributed to the network structure and chain rigidity of HA molecules. On the other hand, the translational and rotational diffusion of the lipid molecules are controlled by bilayer elasticity and electrostatic interactions with HA respectively. We also study the dynamic heterogeneity of the interfacial water molecules in terms of the probability distribution of diffusion coefficients. For subdiffusive translation, we find a peak at a very small diffusion coefficient with a broad distribution of diffusivities, whereas for subdiffusive rotation we note multiple peaks in the distribution. In the diffusive region, HA concentration modifies the distribution significantly, whereas HA chain size has minimal impact. Our studies are important for understanding the molecular mechanisms of disease progression and advancing therapeutic development.

We also examine the effect of an external magnetic field on a model polyampholyte chain with two blocks having an equal number of positive and negative charges. In presence of the field, the chain adopts closed conformations, and its end-to-end distance decreases with increasing field strength. The translational diffusion decreases in the perpendicular plane of the field and increases along the parallel direction. The induced magnetic moment gets aligned with the field direction as field strength increases. Moreover, we observe the rotational autocorrelation time of the moment decreases with increasing field strength. Our study may aid in designing charged polymeric systems with tunable properties for targeted applications.

সারাংশ

প্রোটিন, লিপিড এবং গ্লাইক্যানের মতো বায়োমলিকিউলগুলি জীবদেহের বিভিন্ন জৈব প্রক্রিয়ার জন্য অপরিহার্য। বিভিন্ন বাহ্যিক ছোট লিগ্যান্ড মলিকিউল, পরিবেশ, বাহ্যিক ক্ষেত্র বা ফিল্ডের উপস্থিতিতে বায়োমলিকিউলের গঠন ও কার্যকারিতা পরিবর্তিত হয়। এই পরিবর্তনগুলি বিভিন্ন জৈবিক প্রক্রিয়া থেকে শুরু করে প্রযুক্তিগতভাবে প্রাসঙ্গিক বিভিন্ন ক্ষেত্রে গুরুত্বপূর্ণ ভূমিকা পালন করে।

এই থিসিসটিতে, আমরা অল-অ্যাটম মলিকুলার ডায়নামিক্স সিমুলেশন ব্যবহার করে হ্যালুরোনিক অ্যাসিড (HA)-এর উপস্থিতিতে ডাইপালমিটয়লফসফ্যাটিডাইলকোলিন (DPPC) লিপিড বাইলেয়ারের স্থিতিস্থাপক প্রতিক্রিয়া পরীক্ষা করেছি। আমরা লক্ষ্য করেছি যে ছোট HA চেইনের উপস্থিতিতে বাইলেয়ারের স্থিতিস্থাপক ধ্রুবকগুলির হ্রাস হয়, যা লিপিড বাইলেয়ারটির নরম হয়ে যাওয়ার ইঙ্গিত দেয়। এরপর আমরা HA এর জলীয় দ্রবণ এবং DPPC বাইলেয়ারের সংযোগস্থলে (বা ইন্টারফেসে) গতিশীলতা বিশ্লেষণ করেছি বিভিন্ন মলিকুলের গড় বর্গ স্থানচ্যুতি (মিন স্কোয়ার্ড ডিসপ্লেসমেন্ট বা MSD) করার মাধ্যমে। আমরা লক্ষ্য করেছি যে জল বা HA মলিকুলগুলো যখন বাইলেয়ারের খুব কাছাকাছি থাকে, তখন তারা সাব-ডিফিউসিভ MSD দেখায়, তবে যখন তারা কিছুটা দূরে থাকে, তখন তাদের ক্ষেত্রে ডিফিউসিভ MSD দেখা যায়। ডিফিউসিভ অঞ্চলে, জল এবং HA মলিকুলের অনুবর্তী (বা ট্রান্সলেশনাল) ও ঘূর্ণনশীল (বা রোটেশনাল) ডিফিউশন HA ঘনত্ব বৃদ্ধির সাথে হ্রাস পায়, তবে HA চেইনের আকার পরিবর্তনের ফলে তেমন কোনো পরিবর্তন হয় না। জলের গতিশীলতার এই দুর্বল চেইন-আকার নির্ভরতা HA অণুর নেটওয়ার্ক গঠন এবং তাদের আণবিক দৃঢ়তার সাথে সম্পর্কিত। অন্যদিকে, লিপিড অণুগুলোর ট্রান্সলেশনাল ও রোটেশনাল ডিফিউশন যথাক্রমে বাইলেয়ারের স্থিতিস্থাপকতা এবং HA-এর সাথে ইলেক্ট্রোস্ট্যাটিক ইন্টারঅ্যাকশনের মাধ্যমে নিয়ন্ত্রিত হয়। আমরা ইন্টারফেসিয়াল জলের গতিশীল বৈচিত্র্য বিশ্লেষণ করতে ব্যাপন সহগ (বা ডিফিউশন কোয়েফিসিয়েন্ট) এর সম্ভাব্যতা বন্টনও পরীক্ষা করেছি। সাব-ডিফিউসিভ ট্রান্সলেশনাল গতির জন্য, আমরা খুব ছোট ডিফিউশন কোয়েফিসিয়েন্ট এবং একটি বিস্তৃত বন্টন লক্ষ্য করেছি, অন্যদিকে সাব-ডিফিউসিভ রোটেশনের জন্য, ডিফিউশন কোয়েফিসিয়েন্ট এর সম্ভাব্যতা বন্টনে একাধিক চূড়া (বা পিক) দেখা যায়। ডিফিউসিভ অঞ্চলে, HA ঘনত্ব ডিফিউশন কোয়েফিসিয়েন্ট এর সম্ভাব্যতা বন্টনে উল্লেখযোগ্য পরিবর্তন আনে, কিন্তু HA চেইনের আকারের তেমন কোনো প্রভাব থাকে না। আমাদের গবেষণা বিভিন্ন রোগের আণবিক প্রক্রিয়া বোঝার পাশাপাশি উন্নত চিকিৎসার ক্ষেত্রে সহায়ক হতে পারে।

এরপর আমরা একটি বাহ্যিক চৌম্বক ক্ষেত্রের প্রভাবে একটি মডেল পলিঅ্যামফোলাইট মলিকুলের আচরণও পরীক্ষা করেছি, যেখানে সমান সংখ্যক ধনাত্মক ও ঋণাত্মক চার্জযুক্ত দুটি ব্লক রয়েছে। চৌম্বক ক্ষেত্রের উপস্থিতিতে, চেইনটি নিরুদ্ধ বিন্যাস (বা ক্লোস্ড কনফরমেশন) গ্রহণ করে এবং ক্ষেত্রের তীব্রতা বৃদ্ধির সাথে মলিকুলটির চক্রগতির ব্যাসার্ধ (বা রেডিয়াস অফ জাইরেশন) হ্রাস পায়। আমরা লক্ষ্য করেছি যে মলিকুলটির ট্রান্সলেশনাল ডিফিউশন প্রযুক্ত ক্ষেত্রটির লম্ব সমতলে হ্রাস পায়, তবে ক্ষেত্রের সমান্তরাল দিকে বৃদ্ধি পায়। চৌম্বক ক্ষেত্রটির তীব্রতা বাড়ার সাথে সাথে চৌম্বক ভ্রামক (বা ম্যাগনেটিক মোমেন্ট) ক্ষেত্রের দিকের সাথে সারিবদ্ধ হয়। এছাড়া, চৌম্বক ভ্রামকের ঘূর্ণন স্বয়ংসম্পর্ক সময় (বা অটোকোরিলেশন টাইম) ক্ষেত্রের তীব্রতা বৃদ্ধির সাথে হ্রাস পায়। আমাদের গবেষণা বিভিন্ন টার্গেটেড অ্যাপ্লিকেশনের জন্য চার্জযুক্ত এবং টিউনেবল পলিমারিক সিস্টেম ডিজাইনের ক্ষেত্রে সহায়ক হতে পারে।

List Of Publications

1. Debashish Paul, **Anirban Paul**, Dipanjan Mukherjee, Saroj Saroj, Manorama Ghosal, Suchetan Pal, Dulal Senapati, Jaydeb Chakrabarti, Samir Kumar Pal, and Tatini Rakshit. A mechanoelastic glimpse on hyaluronan-coated extracellular vesicles. The Journal of Physical Chemistry Letters 13, no. 36 (2022): 8564-8572. (https://doi.org/10.1021/acs.jpclett.2c01629)

2. **Anirban Paul** and Jaydeb Chakrabarti. Dynamics of an Aqueous Suspension of Short Hyaluronic Acid Chains near a DPPC Bilayer. Phys. Chem. Chem. Phys. 26 (2024): 20440–49. (https://doi.org/10.1039/D4CP01088D)

3. **Anirban Paul** and Jaydeb Chakrabarti.Dynamic heterogeneity of water at the HA-water and DPPC interface. (manuscript under preparation)

4. **Anirban Paul** and Jaydeb Chakrabarti. Structure and dynamics of a single polyampholyte chain in external magnetic field. (manuscript under preparation)

Contents

Table of Contents **2**

List of Figures **3**

List of Tables **7**

1 Introduction **8**

1.1 Elastic responses of lipid bilayer in the presence of Hyaluronic acid 10

1.2 Dynamics at the interface of aqueous solution of short Hyaluronic acid chains and DPPC bilayer 11

1.3 Dynamic Heterogeneity of water molecules at the HA-water and DPPC interface 12

1.4 Structure and dynamics of a single polyampholyte chain in magnetic field 14

2 Elastic response of DPPC lipid bilayer in presence of Hyaluronic acid **16**

2.1 Introduction 16

2.2 Methods 18

2.2.1 System preparation &simulation details 18

2.2.2 Analysis 19

2.3 Results &Discussions 21

2.3.1 Density profile of the molecular constituents 23

2.3.2 Area compressibility Modulus 24

2.3.3 Bending Modulus 25

2.3.4 Microscopic explanation of the observed results 26

2.4 Conclusion 29

3 Dynamics of aqueous suspension of short hyaluronic acid chains near DPPC bilayer **35**

3.1 Introduction 35

3.2 Methods 36

3.2.1 Force field details and MD simulation 36

3.2.2 Analysis 36

3.3 Results &Discussions 39
3.3.1 Residence time of water and HA chains 39
3.3.2 Dynamics of interfacial water molecules: 42
3.3.3 Dynamics of the interfacial HA chains: 45
3.3.4 Dynamics of the lipid head groups 47
3.3.5 Discussions 48
3.4 Conclusions 51

4 Dynamic heterogeneity of water at the HA-water and DPPC interface 52
4.1 Introduction 52
4.2 Methods 53
4.2.1 Force field details and MD simulation 53
4.2.2 Analysis 54
4.3 Results 55
4.3.1 Self van Hove functions of water molecules near lipid bilayer without HA 56
4.3.2 Self van Hove function of waters at the interface of HA-water and DPPC bilayer for varying HA concentrations 61
4.3.3 Self van Hove function of waters at HA-water and DPPC interface for varying HA chain size 66
4.4 Conclusion 71

5 Structure and dynamics of a single polyampholyte chain in external magnetic field 73
5.1 Introduction 73
5.2 Model and Simulation details 75
5.2.1 Analysis 76
5.3 Results 77
5.3.1 Polymer conformations in equilibrium for different B values 77
5.3.2 Radius of gyration and end-to-end distance of the polymer chain . 78
5.3.3 Induced magnetic moment of the polymer chain 80
5.3.4 Rotational dynamics of induced magnetic moment 82
5.3.5 Mean squared displacement of the PA chain 82
5.4 Conclusion 84

6 Outlook 86

Bibliography 88

List of Figures

1.1 Atomistic structure of HA pentamer. 9
1.2 Typical equilibrium snapshot of lipid bilayer with HA pentamers and HA decamers. 10
1.3 Equilibrium density profile of water, HA center-of-mass and phosphorus atoms of the lipid bilayer for n_{HA5}=50. 12
1.4 Typical equilibrium snapshots of the PA chain for B=0 and B=30 14

2.1 Atomic structure of HA and DPPC 17
2.2 Area per lipid and its time correlation function (inset) for different cases . 22
2.3 Typical equilibrium snapshot for different cases of HA-DPPC system . . . 22
2.4 Density profiles of water, Phosphorus atoms, and HA com along the bilayer normal. 23
2.5 Radial Distribution Function of oxygen atoms of water (OW) around P of DPPC for free and adsorbed lipids for various cases. 24
2.6 (a) Relative area ($< A >$) for different n_{HA5} . (b) for different N values. Relative area fluctuation $< \delta A^2 >$ with n_{HA5} for (c) 512 DPPC bilayer and (d) 128 DPPC bilayer. Relative compressibility modulus k_A for different (e)n_{HA5} and (f) for different N. 25
2.7 k_c calculation for n_{HA5}=50. 26
2.8 Relative Bending modulus k_C for different (a) n_{HA5} and (b) for different N 26
2.9 (a) tetrahedral order Q_{Tr} of interfacial water molecules vs n_{HA5} (b) k_A vs Q_{Tr} 27
2.10 RDF of P atoms of DPPC around heavy atoms of HA, g_{HA-P} (r) for n_{HA5} = 10 (black), 30 (red), and 50 (blue). 27
2.11 S_{CD} of sn1 and sn2 chain of free and adsorbed lipids for different n_{HA5} . . 28
2.12 (a) Mean thickness of the bilayer as a function of n_{HA5}. (b)Surface roughness of the HA-adsorbed lipids as a function of n_{HA5} 29

3.1 A schematic diagram of region A and region B in the density profile of n_{HA5}=50. 39

3.2 Survival probability of water $S_W(t)$ in region A and region B for different HA concentrations and HA chain size 40
3.3 Mean residence time of water in region A and region B for different n_{HA5} and N. 40
3.4 Survival probability and mean residence time of HA monomers at the HA-water and DPPC interface 41
3.5 Translational MSD and diffusion coefficients of interfacial water molecules for different n_{HA5} and N 42
3.6 Rotational MSD and diffusion coefficients of interfacial water molecules for different n_{HA5} and N 43
3.7 Rotational autocorrelation function of the water molecules (C(t)) in region B for different HA concentrations and HA chain sizes. 44
3.8 Translational MSD of HA chains in the plane parallel to the bilayer surface and Rotational MSD of HA chains for different n_{HA5} and different N in region B. Translational and rotational diffusion coefficients are also shown. 46
3.9 Translational MSD and translational diffusion coefficients of phosphorus atoms of the lipid bilayer 47
3.10 Rotational MSD and rotational diffusion coefficients of the PN vectors of the lipid bilayer 48
3.11 Cross-chain radial distribution of interfacial HA monomers, Histogram of persistence length (l_P) to end-to-end distance (R_e) ratio of the HA chains, Electrostatic interaction energy and number of hydrogen bonds between HA and DPPC, for different n_{HA5} and N. 49

4.1 ln$G_T(r,\Delta t)$ vs Δt plot for n_{HA5} = 0 for Δt=5ps and Δt=10ps in the subdiffusive interface. Time variation of r_c, σ^2 and λ are shown. The distribution of translational diffusivities $P(D_T)$ at Δt=5ps and Δt=10ps are also depicted 56
4.2 ln$G_T(r,\Delta t)$ vs Δt plot for n_{HA5} = 0 for Δt=10ps and Δt=20ps in the diffusive interface. Time variation of r_c, σ_1^2 and σ_2^2 are shown. The distribution of translational diffusivities $P(D_T)$ at Δt=10ps and Δt=20ps are also depicted. 57
4.3 ln$G_R(\phi,\Delta t)$ vs Δt plot for n_{HA5} = 0 for Δt=5ps Δt=10ps in the subdiffusive interface. Time variation of ϕ_c, σ^2 and λ are shown.The distribution of rotational diffusivities $P(D_R)$ at Δt=5ps and Δt=10ps are also depicted. . 59
4.4 ln$G_R(\phi,\Delta t)$ vs Δt plot for n_{HA5} = 0 for Δt=10ps Δt=20ps in the diffusive interface. Time variation of σ_1^2, σ_2^2 and λ are shown. 60
4.5 The distribution of rotational diffusivities $P(D_R)$ at Δt=10ps and Δt=20ps. 60

4.6 ln$G_T(r, \Delta t)$ vs Δt plot for different HA concentrations in the subdiffusive interface are shown. Distribution of diffusivity $P(D_T)$ for different cases at Δt=5ps and Δt=10ps are also shown. 61
4.7 ln$G_T(r, \Delta t)$ vs Δt plot for different HA concentrations in the diffusive interface are shown. Distribution of diffusivity $P(D_T)$ for different cases at Δt=10ps and Δt=20ps are also shown. 63
4.8 D_T^1, D_T^2 and $\langle D_T \rangle$ for different $\mathrm{n_{HA5}}$ 63
4.9 ln$G_R(\phi, \Delta t)$ vs Δt plot for different HA concentrations in the subdiffusive interface are shown. Distribution of diffusivity $P(D_R)$ for different cases at Δt=5ps and Δt=10ps are also illustrated. 64
4.10 ln$G_R(\phi, \Delta t)$ vs Δt plot for different HA concentrations in the diffusive interface are shown. Distribution of diffusivity $P(D_R)$ for different cases at Δt=10ps and Δt=20ps are also shown. 65
4.11 $\langle D_R \rangle$ for different $\mathrm{n_{HA5}}$ 66
4.12 ln$G_T(r, \Delta t)$ vs Δt plot for different HA chain sizes in the subdiffusive interface are shown. Distribution of diffusivity $P(D_T)$ for different cases at Δt=5ps and Δt=10ps are also shown. 67
4.13 ln$G_T(r, \Delta t)$ vs Δt plot for different HA chain sizes in the diffusive interface are shown. Distribution of diffusivity $P(D_T)$ for different cases at Δt=10ps and Δt=20ps are also shown. 68
4.14 D_T^1, D_T^2 and $\langle D_T \rangle$ for different N 68
4.15 ln$G_R(\phi, \Delta t)$ vs Δt plot for different HA chain sizes in the subdiffusive interface are shown. Distribution of diffusivity $P(D_R)$ for different cases at Δt=5ps and Δt=10ps are also shown. 69
4.16 ln$G_R(\phi, \Delta t)$ vs Δt plot for different HA chain sizes in the diffusive interface are shown. Distribution of diffusivity $P(D_R)$ for different cases at Δt=10ps and Δt=20ps are also shown. 70
4.17 $\langle D_R \rangle$ for different N 71

5.1 Potential energy and radius of gyration of the PA chain for B=0 and B=30. 77
5.2 Polymer conformations at different MD time steps. 78
5.3 Distribution and mean radius of gyration for different field strengths are shown. Distribution and mean end-to-end distance for different field strengths are also depicted. 79
5.4 Distribution of the angle θ between the two blocks of the polymer for different magnetic field strengths. 80
5.5 μ_x, μ_y and μ_z of the PA chain for different field strengths. 80
5.6 Distribution of azimuthal angle ϕ_μ for different magnetic field strengths. . 81
5.7 Distribution of polar angle θ_μ for different field strengths. 81

5.8 Rotational autocorrelation of magnetic moment $\vec{\mu}$ for different field strengths. 82
5.9 MSD of the PA chain and diffusion coefficients in perpendicular plane and parallel direction of the applied field for different field strengths. 83

List of Tables

2.1 Correlation time of $\langle A \rangle$ for different cases with 512 DPPC bilayer 22

3.1 First rank rotational autocorrelation time of water molecules, t_1^W in region B (computed from C(t) in Figure 3.7) and the product of t_1^W and rotational diffusion, D_R^W 45
3.2 First rank rotational autocorrelation time t_1^H for interfacial HA monomers 46

Chapter 1 Introduction

Biomolecules like proteins, lipids, and glycans are essential for biological processes in living organisms. Each type of biomolecule has a unique 3-dimensional structure which is linked to its specific functions. Biomolecules often interact with external ligands or respond to changes in their environment. These interactions can alter their structure and function[1,2] and are important for their biophysical activities. For example, binding a substrate to the active site of an enzyme can induce conformational changes that facilitate the catalytic process.[3,4] Interaction with polar and hydrophilic ligands like TAT polypeptide,[5] glyphosate,[6] polycations,[7] hydrophobic ligands such as polystyrene,[8] and amphipathic ligands like quercetin,[9] can cause lipid membrane to deform and alter its mechanical properties.

Biomolecules, such as proteins, are natural polyampholytes containing both positively and negatively charged amino acid residues.[10] The pH of the surrounding medium governs the overall charge of the biomolecule. The net charge vanishes at the isoelectric point (pI), while it becomes positive or negative at pH values below or above the pI, respectively. External magnetic fields can significantly influence the conformation and functionalities of biomolecules having charged moieties.[11,12] The effect of the magnetic field on charged macromolecules is also important for technological purposes. Magnetic field-induced ordering offers enhanced control over block copolymer domains,[13,14] which is crucial for achieving tunable properties.[15]

Hyaluronic acid (HA) is a negatively charged, highly hydrophilic glycan molecule. It is a long polyanionic molecule composed of repeating units of d-glucuronic acid and N-acetyl-d-glucosamine (atomistic structure is shown in Figure 1.1). HA is found in extracellular matrices (ECM), synovial fluid of joints, the vitreous humor of eyes, etc, and plays a crucial role in cellular lubrication and connection.[16] Under normal physiological conditions, HA chains typically range from 2000 to 16,000 monomers in length.[17] However, in pathological conditions such as osteoarthritis and cancer, both

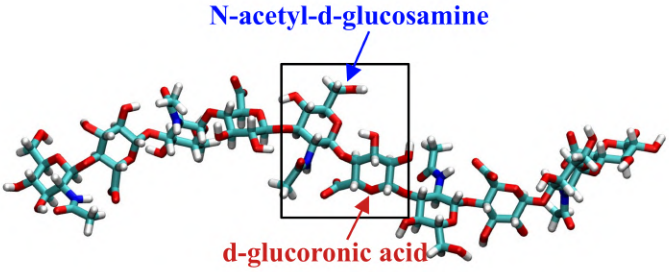

Figure 1.1: Atomistic structure of HA pentamer in Licrorice representation. HA monomer is shown in the square box. Oxygens are red, Carbons are cyan, Nitrogens are blue and Hydrogens are white.

the concentration and size of HA are altered. Invasive breast cancer cells produce an excess of HA chains, which interact with the HA receptor protein CD44, promoting increased cell motility, invasion, growth, and therapeutic resistance.[18] Similarly, colon cancer cells exhibit overexpression of HA receptor proteins, the HA-degrading enzyme hyaluronidase, and small HA chains ($\approx$ 250 monomers long).[19] Changes in HA chain size and concentration lead to significant physical modifications in cells and body fluids. In osteoarthritis, the reduction in HA concentration and molecular weight results in the loss of the viscoelastic and lubricating properties of synovial fluid.[20] Furthermore, atomic force microscopy (AFM) studies indicate that liposomes secreted by cancer cells and coated with low-molecular-weight HA exhibit significantly greater flexibility compared to those secreted by normal colon cells.[19] In this thesis, we examine in detail the elastic response and interfacial dynamics in the aqueous solution of the lipid membrane along with short HA chains.

We observe that the membrane elastic constants decrease with HA concentration and HA chain size, where chain size dependence is weaker. We also find that the interfacial dynamics slow down with increasing HA concentration and HA chain size. However, similar to the mechanical changes, here we also note that chain-size dependence is weaker. We explain the weak chain size dependence of water dynamics in terms of HA chain flexibility and its network structure at the interface. We observe dynamic heterogeneity in the translation and rotation of interfacial waters. Additionally, we find that the diffusivity of interfacial water molecules has a probability distribution that remains the same even if we change HA concentration or its chain size.

We also study a bead spring model polyampholyte (PA) chain with block arrangements of oppositely charged beads in an external magnetic field. This is a simple model for neutral polyampholytes. We observe changes in the static and dynamic properties of a polyampholyte chain in presence of external magnetic field. We find that closed polymer conformations emerge as the field is applied. The radius of gyration and end-to-end distance decreases with increasing field strength. The induced magnetic moment gets aligned with the external field. We also find that the diffusivity of the PA chain decreases in the perpendicular plane of the field and increases along the field direction.

This chapter is organized as follows: In section 1.1 we investigate the elastic response of lipid bilayer in presence of HA chains. In section 1.2 we study the dynamics at the interface of HA-water and DPPC bilayer. The dynamic heterogeneity of water molecules at the interface is discussed in section 1.3. Section 1.4 illustrates our investigation on the structure and dynamics of block PA chain in presence of magnetic field.

1.1 Elastic responses of lipid bilayer in the presence of Hyaluronic acid

Short HA chains are more abundant in cellular environment in pathological conditions. The effects of short HA chain have received very little attention. Recent AFM results show that short HA chains coated extracellular vesicles in cancer environment are more flexible than normal vesicles.[19] To understand the underlying microscopic picture we have performed an atomistic molecular dynamics (MD) simulation of the Dipalmitoylphosphatidylcholine (DPPC) bilayer in the presence of HA chains in explicit TIP3P model solvents. PC lipids are chosen in this work because of their elevated level in colon cancer cells compared to normal colon cells.[21] We study the elastic response of the bilayer for different HA concentrations (n_{HA5}) and HA chain size (N). Typical equilibrium snapshots for with HA pentamers and decamers are shown in Figure 1.2(a) and 1.2(b) respectively.

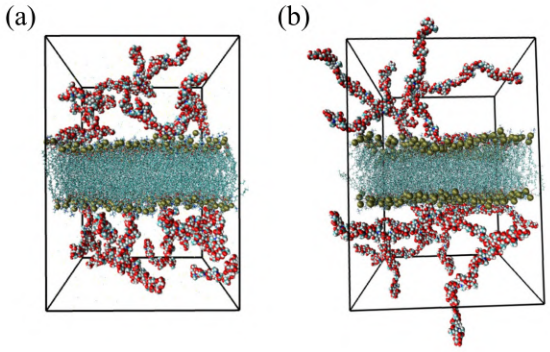

Figure 1.2: Typical equilibrium snapshot of lipid bilayer with (a) HA pentamers and (b) HA decamers. Hyaluronic acids (HA) and lipid bilayer are shown in vdw and bonds representation respectively with the following color codes: Cyan for Carbons, red for Oxygens, and blue for Nitrogens. Water molecules are not shown.

We compute the density profile of phosphorus atoms of DPPC, oxygen atoms of the water molecules, and HA center of mass along the bilayer normal. We observe that the aqueous solution of HA and the bilayer form an interface. We also find that the HA-DPPC interaction is water-mediated. We compute the average lateral area of the bilayer $\langle A \rangle$ and its fluctuation for different $\mathrm{n_{HA5}}$ and N. $\langle A \rangle$ remains the same in presence of HA chains, implying the overall bilayer structure is intact. However, we observe that the fluctuation of the bilayer area ($\langle \delta A^2 \rangle$) increases as $\mathrm{n_{HA5}}$ and N increases. We use $\langle \delta A^2 \rangle$ to compute area compressibility modulus of the bilayer, $k_A = k_B T \frac{<A>}{<\delta A^2>}$. We find that k_A decreases with $\mathrm{n_{HA5}}$ and N, where the N dependence is weaker than $\mathrm{n_{HA5}}$. In addition to the area fluctuation we also compute the bending modulus of the bilayer k_c. k_c is computed from the amplitude of the height fluctuation of the bilayer $|h_q|^2$ in Fourier space ($k_c = k_B T \frac{1}{q^4 |h_q|^2}$). We note that k_c decreases both with $\mathrm{n_{HA5}}$ and N. However, the concentration dependence is more prominent. The decreased area compressibility modulus and bending modulus indicate increased flexibility of the bilayer as HA concentration and size increase.

We show that HA-adsorbed lipids have higher tail ordering than HA-free lipids. Therefore as $\mathrm{n_{HA5}}$ increases, more HA monomers come close to the bilayer, and HA-adsorbed lipid tails become more ordered. The ordering of the tails enhances the registry between successive lipid molecules, facilitating their out-of-plane and lateral movements. Hence, the area per lipid of the bilayer shows more fluctuations and the bilayer becomes more flexible.[19]

1.2 Dynamics at the interface of aqueous solution of short Hyaluronic acid chains and DPPC bilayer

The interfacial dynamics near the cellular boundary are significantly linked with the system viscoelasticity and mechanical responses. The bulk dynamics of HA solutions are well-studied experimentally,[22,23] however, the dynamics near the lipid bilayer remain unexplored. Therefore, here we study the dynamics at the HA-water and DPPC interface.

From our atomistic simulation, we observe that the aqueous solution of HA and DPPC form an interface of width 15 Å (the shaded region of the density profile shown in Figure 1.3). We identify region A in the interface where only water molecules are present (from the peak of phosphorus(d_p) to 5Å above it along the bilayer normal), and region B where both water molecules and HA chains are present (d_p+5Å to d_p+15Å along bilayer normal).

We compute the residence time of water in both regions. In both cases, the residence time decreases with $\mathrm{n_{HA5}}$ and N, where N-dependence is weaker than $\mathrm{n_{HA5}}$. We calculate the translational mean squared displacement (MSD) ($\langle r_W^2 \rangle$) and rotational MSD ($\langle \phi_W^2 \rangle$) of the water molecules continuously residing at the interface, namely within the mean residence time. We find both $\langle r_W^2 \rangle$ and $\langle \phi_W^2 \rangle$ are subdiffusive in region A, whereas they

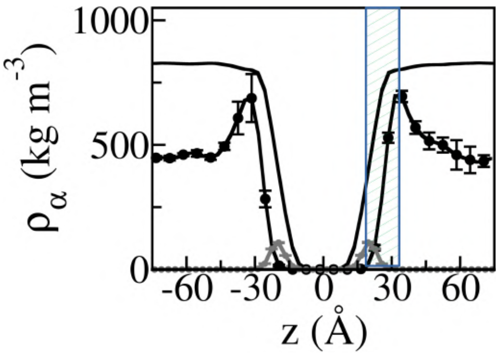

Figure 1.3: Equilibrium density profile of water (solid black line), HA center-of-mass (dotted black line) and phosphorus atoms of the lipid bilayer for n_{HA5}=50. ρ_α stands for density profiles of different molecular constituents α. The interface of HA-water and DPPC bilayer is shown as the shaded region.

are both diffusive in region B. In the diffusive B region, we compute the translational and rotational diffusion coefficients. We find that both translational and rotational diffusion coefficient decreases with n_{HA5} and N where they are both weakly dependent on N. We show that the HA network at the interface becomes more compact with increasing HA concentration. Hence water dynamics become monotonically restricted. On the other hand, with N the HA chain flexibility increases and the network structure gets weaker. Therefore, there is competition between hydrophilic interaction between HA-water and HA chain flexibility, which leads to weak N dependence.

We also investigate the dynamics of HA chains at the interface and the phosphorus atoms of the lipid bilayer. The translational motion of HA chains exhibits subdiffusive behavior, whereas their rotational dynamics remain diffusive. The rotational diffusion coefficient decreases with n_{HA5} as HA forms more compact network at the interface as n_{HA5} increases. However, it remains unchanged for larger N due to the competition between HA residence and increased chain flexibility with N. The translational diffusion coefficient of phosphorus atoms, D_T^P, increases with n_{HA5}, consistent with enhanced bilayer flexibility.[19] On the other hand, D_T^P initially increases with N before decreasing at larger N. Additionally, we note that the rotational diffusion D_R^P of the PN dipoles in lipid headgroups decreases with n_{HA5} but increases with N.

1.3 Dynamic Heterogeneity of water molecules at the HA-water and DPPC interface

The emergence of multiple close but distinct relaxation timescales in a system is known as dynamic heterogeneity. Dynamic heterogeneity regulates the viscoelastic response and diffusion near biological and inorganic interfaces.[24] It can be studied in terms of the self van-Hove correlation function (svHf), G(ξ,Δt), where G(ξ,Δt) is defined as the distribution of translational or rotational displacement ξ of the particles in the time interval Δt, mathematically G(ξ,Δt) = $\langle \frac{1}{N}\sum_{i=1}^{N}\delta[\xi - |\vec{\xi_i}(\Delta t) - \vec{\xi_i}(0)|]\rangle$, where N is the total number of tagged particles.[25] For a normal fluid, $G(\xi,\Delta t)$ follows a Gaussian distribution in ξ. However, in the presence of dynamic heterogeneity, $G(\xi,\Delta t)$ deviates from a purely Gaussian form for Δt much less than the longest relaxation time in the system such as near the interfaces. We also compute the distribution of diffusivities, $P(D_\xi)$.[26] The presence of dynamic heterogeneity is also evident in $P(D_\xi)$.

The residence time of water in the thin (width $\approx$ 5Å) subdiffusive interface (region A) $\tau_w^A \approx$10ps whereas the residence time of water in the thick (width $\approx$ 10Å) diffusive interface (region B) $\tau_w^B \approx$20ps. We compute the translational and rotational svHf in both regions for $\Delta t \lesssim \tau_w^A$ and $\Delta t \lesssim \tau_w^B$ respectively. In the subdiffusive region (region A) we find that the translational svHf $G_T(r,\Delta t)$ (r is the displacement of oxygen atoms of water along the plane perpendicular to the bilayer normal in time Δt) shows an exponential tail. The underlying diffusivity distribution $P(D_T)$ shows a sharp peak at a very small translational diffusivity D_T. The $P(D_T)$ is similar for all values of $\mathrm{n_{HA5}}$. The nature of $G_T(r,\Delta t)$ and $P(D_T)$ remains same for varying N as well. On the other hand, $G_T(r,\Delta t)$ in the diffusive region (region B) exhibits double Gaussian dependence on r for all $\mathrm{n_{HA5}}$ and N. The double Gaussian nature indicates the existence of two diffusion timescales. The underlying distribution of diffusivity $P(D_T)$ has a broad peak. We compute the average diffusion coefficient $\langle D_T\rangle$ from $P(D_T)$. As $\mathrm{n_{HA5}}$ increases we find $\langle D_T\rangle$ decreases. This implies slower translation of the interfacial water molecules as $\mathrm{n_{HA5}}$ increases. $\langle D_T\rangle$ remains the same for different N values.

Next, we study the rotational svHf $G_R(\phi,\Delta t)$ (where ϕ is the rotational displacement of water dipoles in time Δt) in the subdiffusive and diffusive regions. In the subdiffusive region, $G_R(\phi,\Delta t)$ shows an exponential tail. The distribution of rotational diffusivity $P(D_R)$ shows multiple peaks. In the diffusive region, we find that $G_R(\phi,\Delta t)$ exhibits a Gaussian tail at a large time. In the $P(D_R)$ profile, there are two prominent peaks with a small peak at a small value of rotational diffusion coefficients D_R. The nature of $G_R(\phi,\Delta t)$ and $P(D_R)$ remains same for $\mathrm{n_{HA5}}$ and N. We calculate the average diffusion coefficient $\langle D_R\rangle$ from $P(D_R)$. We find that, as $\mathrm{n_{HA5}}$ increases, $\langle D_R\rangle$ decreases and remains the same for varying N values. The dependencies of $\langle D_T\rangle$ and $\langle D_R\rangle$ on $\mathrm{n_{HA5}}$ and N are consistent with the diffusion coefficients obtained from the MSD data.[27]

1.4 Structure and dynamics of a single polyampholyte chain in magnetic field

An external magnetic field interacts with a material having charged groups.[28] Experiments show that the structure and functions of biomolecules with charged groups are affected by external magnetic fields.[11,12] One of the key technological applications of magnetic fields on polymeric materials is magnetic alignment.[15] The alignment of the block polymer is observed over a wide range of magnetic fields.[13] Using x-ray scattering experiments, the role of anisotropy of intrinsic chain susceptibility is also investigated in the self-assembly of block copolymer directed by external magnetic field.[29] There are theoretical studies on two-dimensional Yukawa systems,[30,31] Rouse dimers,[32] Nacl[33] and AgI salts,[34] etc in the presence of magnetic field. However, the effect of magnetic fields on the microscopic structure and dynamics of polymeric materials remains poorly understood.

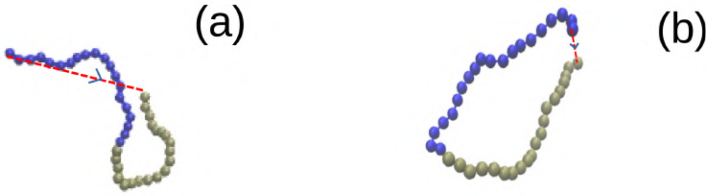

Figure 1.4: Typical equilibrium snapshots of the PA chain for (a) B=0 and (b) B=30. The arrows indicate end-to-end vectors.

Here we study a bead-spring model polyampholyte (PA) chain with an equal number of positive and negatively charged beads arranged in the block fashion (see Figure 1.4). We study the static and dynamic response of the polymer chain to an externally applied strong magnetic field. The equations of motion are derived from the Hamiltonian $H = \frac{(\vec{P}-q\vec{A})^2}{2m} + V(r)$. Here the Hamiltonian included the magnetic field $\vec{B}$ via the the magnetic vector potential $\vec{A}$, where $\vec{B} = \vec{\nabla} \times \vec{A}$.[33,35] In all cases, we consider B to be along the z-axis, hence $\vec{A} = -\frac{B}{2} y\hat{x} + \frac{B}{2} x\hat{y}$. We observe that the chain takes open conformations when there is no field, but closed conformations as the field is applied as shown in Figure 1.4. We also compute the induced magnetic moment of the PA chain in three directions μ_x,μ_y, and μ_z, all of which increase as B increases. We observe that the alignment of the moment $\vec{\mu}$ with respect to the magnetic field B improves as the field strength increases. Moreover, higher field strength leads to faster rotational relaxation of $\vec{\mu}$. Next, from the long-time MSD plot, we compute diffusivity in the perpendicular plane of the magnetic field (D$_{xy}$) and diffusivity along the field direction (D$_z$). We find D$_{xy}$ decreases as field strength increases. On the other hand D$_z$ increases with increasing field strength.

In conclusion, this thesis investigates the structural and dynamic responses of macromolecules to external perturbations. We examine the elastic response and interfacial dynamics of lipid bilayers in the presence of HA chains. Additionally, we explore the structural and dynamic behavior of a PA chain under the influence of an external magnetic field. The thesis contains the following chapters: chapter 2 contains the details of the elastic response of a model lipid bilayer to Hyaluronic acid of different HA concentrations and HA chain sizes. Chapter 3 narrates the dynamics of molecular constituents at the interface of HA-water and DPPC bilayer. The dynamic heterogeneity of water molecules at the HA-water and DPPC interface is discussed in Chapter 4. Chapter 5 describes the response of a block polyampholyte chain to an external magnetic field. We discuss possible outlook of our work in Chapter 6.

Chapter

2

Elastic response of DPPC lipid bilayer in presence of Hyaluronic acid *

2.1 Introduction

Hyaluronic acid (HA) is one of the important components of extracellular matrix (ECM) and present in all biological fluids and tissues e.g. joint synovial fluid, vitreous humor, etc.[36] HA plays a crucial role in maintaining tissue hydration, viscoelasticity of liquid connective tissues, water transport, cell signaling, wound healing, etc. It is a linear, poly-anionic, nonsulfated, highly hydrophilic, long glycosaminoglycan molecule that is made of repeating monomeric unit of β(1-4)-D-glucuronic acid- β(1-3)-N-acetyl-d-glucosamine. The chemical structure is shown in Figure 2.1(A). The physiological properties of HA typically depend on its polymeric character as well as the viscous nature of its solution.

Apart from its versatile physiological functions, HA is a biomarker for the diagnosis of different diseased states including cancer, rheumatoid arthritis, liver pathologies, etc.[36] In the malignant process, HA is known to have a significant role at multiple levels. The presence of HA around tumor cells is correlated with aggressiveness and poor prognosis of tumor tissues.[37,38] In pathological conditions like cancer and inflammation, the amount of HA is increased in cells and body fluids, which helps in cellular growth and motility. Studies also show that HA-coated extracellular vesicles (EVs) carry signals for malignant tumor growth and metastasis in cancer cells.[39]

In colon cancer cells, HA is associated with its receptor proteins such as CD44.[40] Recent literature suggests that low molecular weight(LMW) HA chains are present

---

[*] Based on the publication: Debashish Paul, **Anirban Paul**, Dipanjan Mukherjee, Saroj Saroj, Manorama Ghosal, Suchetan Pal, Dulal Senapati, Jaydeb Chakrabarti, Samir Kumar Pal, and Tatini Rakshit. A mechanoelastic glimpse on hyaluronan-coated extracellular vesicles. The Journal of Physical Chemistry Letters 13, no. 36 (2022): 8564-8572. (https://doi.org/10.1021/acs.jpclett.2c01629

significantly in colon cancer cells and play a role in tumor metastasis. Interestingly, their levels are significantly reduced after resection of the tumor cells.[41] Atomic force microscopy and spectroscopy study shows colon cancer-secreted extracellular vesicles (EVs) and normal EVs are both positive in CD9 protein, an HA receptor protein. Cancer EVs exhibit an increased surface density of HA compared to normal EVs.[42] Hence, HA-coated EVs can be used as potential biomarkers for early-stage detection of colon cancer cells. Using the single-molecule force spectroscopy method, the authors have also shown the abundance of HA in cancer EVs with contour length≈ 238nm,[19] which is supported by previous literature suggesting degradation of HA in inflammatory conditions.[17] AFM results show that HA-coated cancer EVs are significantly elastic compared to normal EVs. The Young's modulus of normal EVs is 3.30±1.80 MPa whereas Young's modulus obtained for cancer EVs is 2.11±1.70 MPa. They have also found that Hyaluronidase (HYAL) treated EVs, where HA chains are fragmented to low molecular weight HA chains (LMW-HA), show an increase in Young's modulus to 4.24±1.90 MPa. Therefore, the accumulation of LMW-HA is responsible for the flexibility of the cancer EVs.

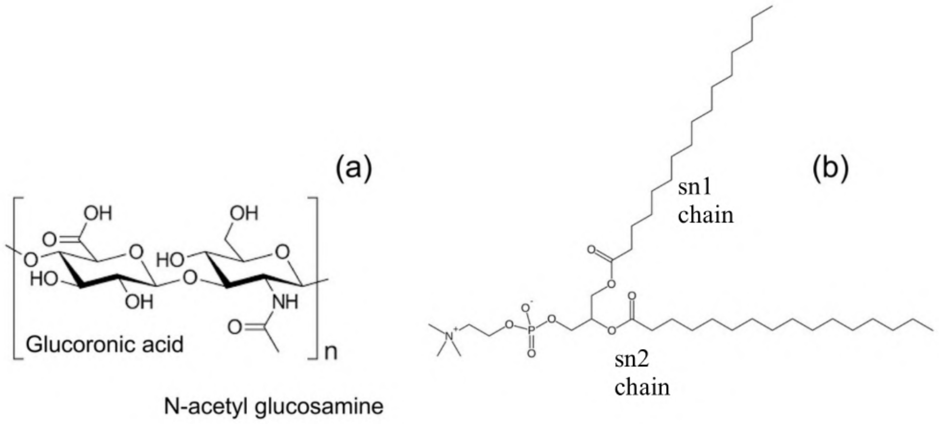

Figure 2.1: Atomic structure of (a) Hyaluronic acid (HA) and (b) Dipalmitoylphosphatidylcholine (DPPC)

Under experimental conditions, the membranes surrounding the EVs are complex in terms of lipid composition and the presence of HA receptor proteins. Additionally, the solvent dispersing the EVs contains HA of various sizes and Hyaluronidase enzymes. To qualitatively examine the role of HA in experimental findings, we study the effect of the concentration and length of HA chains on the elastic properties of a model dipalmitoylphosphatidylcholine (DPPC) lipid bilayer. The chemical structure of the DPPC molecule is shown in Figure 2.1(b). Although lipid composition affects membrane properties and elasticity,[43] we chose PC lipids to model the bilayer due to their elevated levels in colon cancer cells.[21] We perform all-atom molecular dynamics (MD) simulations and compute various elastic constants over the equilibrated portion of the trajectory. Due to the inherent limitations of computational power, we consider HA chains much shorter than those in the experiments. We keep the chain length fixed (pentamer) while varying the monomer concentration and the monomer concentration fixed while varying the chain length [more details are in Methods]. We investigate the nature of the interaction between HA and DPPC and the importance of water in the mechanism. We calculate the equilibrium area fluctuation, compressibility modulus, and bending modulus, which agree well with the experimental results. Finally, we explain our observations based on the tetrahedral ordering of interfacial water molecules and lipid tail order parameters.

2.2 Methods

2.2.1 System preparation & simulation details

The all-atom model of a lipid bilayer of a total of 512 Dipalmitoylphosphatidylcholine (DPPC) molecules (256 in each leaflet) is constructed in a simulation box of size 12.45 nm × 12.45 nm × 15.1 nm using CHARMM GUI membrane builder module.[44] The bilayer is spanned in the xy plane and the normal is along the z axis. The initial structure of Hyaluronic acid is taken from RCSB PDB id 2BVK[45] and it is modified in CHARMM GUI glycan modeler[46] to obtain Hyaluronan monomer (HA1), pentamer(HA5) and decamer(HA10) structure. HA molecules are randomly placed above the bilayer using Packmol. Sodium ions are added for electroneutrality and additional sodium-chloride salt is added to maintain the 150-millimolar physiological salt concentration. All molecular dynamics simulations (see Appendix A2.1 for details) are performed using the GROMACS package[47] where we solve the equation of motion of all the particles using *Leap-frog* algorithm using equations A2.1.1 and A2.1.2. The potential energy of interaction is modeled using CHARMM36 force-field parameters[48] (see appendix A2.2 and equation A2.2.1 for details of *force fields*). During the simulation, the periodic boundary condition is employed in all directions (see Appendix A2.3 for details). 12 Å is considered a truncation limit for both Lennard-Jones and Van-der-Waals interactions. TIP3P water model is used for solvating the system.

The system is energy minimized and followed by short NVT and NPT equilibrations with gradually removing the position and dihedral restraints. The temperature is fixed at 323 K using the Nosé–Hoover thermostat.[49] The lipid bilayer and all other components except the bilayer (i.e. HA chains, water, and ions) are separately coupled with the thermostat. The period of the temperature fluctuations is set at 1 femtosecond (fs) and the corresponding equations A2.4.1 and A2.4.2 are solved (see details in Appendix A2.4). The pressure is fixed at 1 bar using semi-isotropic pressure coupling with a Parrinello–Rahman barostat.[50] The period of the pressure fluctuations is set at 5 femtoseconds (fs). The compressibility of the system is set at 4.5×10^{-5} bar^{-1} (see

Appendix A2.5 for details). The Particle Mesh Ewald (PME) method^{51} is used to assess long-ranged electrostatic energy using equation A2.6.1 (details of *PME* is discussed in Appendix A2.6). Finally, the production runs in the NPT ensemble are executed for 600 nanoseconds with 1 femtosecond integration time step removing all restraints. The trajectory has been saved at 10 picoseconds intervals. Last 400 nanoseconds of trajectory are used for analysis.

The studies are carried out with 10, 30, and 50 HA pentamer (HA5), respectively (n_{HA5}= 10, 30, and 50), above the bilayer and HA molecules of different chain lengths: 150 HA monomer (HA1), 30 HA pentamer (HA5), and 15 HA decamer (HA10) with N = 1, 5, and 10, respectively.

2.2.2 Analysis

Density profile calculation

The density profile of water, phosphorus atoms, and the center of mass (com) of Hyaluronic acid molecules (HA) are obtained along the bilayer normal (z-axis) using the Gromacs density tool.^{52} This is defined as the density of the molecules within thin slices along the z-direction. The z-direction is binned in 50 slices. The slices have the same cross-sectional area as the bilayer lateral plane (XY plane).

Area per lipid

Area per lipid A_{PL} is obtained by dividing the lateral area of the bilayer in x-y plane by the number of lipids in each leaflet. $A_{PL}(t) = \frac{A(t)}{N}$, where N is the number of lipids per leaflet, here N=256. $A(t)$ is the lateral area of the bilayer at time t. We compute the normalized time correlation of area per lipid using the formula:

$$C(\Delta t) = \frac{\langle \delta A_{PL}(\Delta t) \delta A_{PL}(0) \rangle}{\langle \delta A_{PL}(0) \delta A_{PL}(0) \rangle} \tag{2.1}$$

where $\delta A_{PL}(\Delta t) = A_{PL}(\Delta t) - \langle A_{PL} \rangle$.

Area fluctuation and the area compressibility modulus of the lipid bilayer

The equilibrium area fluctuation is calculated using the following definition

$$\langle \delta A^2 \rangle = \langle [A(t) - \langle A \rangle]^2 \rangle. \tag{2.2}$$

Here, $\langle A \rangle$ implies the average lateral area of the bilayer. The area compressibility modulus k_A of the bilayer is computed from $\langle A \rangle$ and $\langle \delta A^2 \rangle$ using the formula:[53]

$$k_A = k_B T \frac{\langle A \rangle}{\langle \delta A^2 \rangle} \tag{2.3}$$

.

Bending modulus

The bending modulus k_c of the DPPC bilayer is calculated from the power spectrum of the equilibrium height fluctuation of the lipid bilayer using the following formula[54]

$$k_c = \frac{k_B T}{q^4 |h_q|^2} \tag{2.4}$$

Here q is the magnitude of wavevector $\vec{q}$ and $|h_q|^2$ is the power spectrum of height fluctuation. The lipids are divided into two-dimensional girds across the bilayer plane, and the height h(x,y) of each grid is calculated. The h(x,y) is then Fourier transformed in two dimensions to obtain the height spectra. Equation 2.4 holds at the limit $q \to 0$.[55] $q^4|h_q|^2$ vs q data at small q values are fitted to a constant line to obtain k_c (see Figure 2.7).

Tetrahedral order parameter of water molecules

The tetrahedral order parameter of water molecules Q_{Tr} is defined as

$$Q_{Tr} = 1 - \frac{3}{8} \sum_{j=1}^{3} \sum_{k=j+1}^{4} (cos\psi_{jk} + \frac{1}{3})^2 \tag{2.5}$$

where ψ_{jk} is the angle between bond vectors joining the oxygen atom of the water molecules under consideration and its nearest neighbor oxygen atoms j and k.[56] Here, Q_{Tr} is obtained for only those water molecules which are at the interface of HA-water and DPPC bilayer.

Radial distribution function

The radial distribution function (RDF), $g(r)$, is defined as the probability of finding a particle (type B) at a distance r from a reference particle (type A).

Mathematically, it is defined as:

$$g_{AB}(r) = \frac{1}{\rho_B N_A} \left\langle \sum_{i=1}^{N_A} \sum_{j=1}^{N_B} \delta(r - |\mathbf{r}_i - \mathbf{r}_j|) \right\rangle , \tag{2.6}$$

where: ρ_B is the number density of type B particles, N_A is the total number of A type particles, $\mathbf{r}_i$ and $\mathbf{r}_j$ are the positions of particles i and j, δ is the Dirac delta function, $|\mathbf{r}_i - \mathbf{r}_j|$ is the distance between particles i and j, The angular brackets $\langle\ \rangle$ represent an ensemble average.

Acyl chain order parameters of the lipid molecules

Acyl chain order parameters of the lipid molecules, S_{CD} is defined as

$$|S_{CD}| = \frac{1}{2}\langle 3cos^2\theta - 1\rangle \tag{2.7}$$

where θ is the angle between bilayer normal and C-H bond vectors.[57] The angular bracket denotes the average over time and molecules.

Mean thickness and average roughness of the bilayer

The mean thickness of the bilayer (d_{P-P}) is calculated using the following equation:[58]

$$d_{P-P} = \langle z_u\rangle - \langle z_l\rangle \tag{2.8}$$

where $\langle z_u >$ and $\langle z_l\rangle$ are the time-averaged z-coordinate of Phosphorus atoms of DPPC molecules of the upper and lower leaflets respectively. The roughness of the lipid surface is obtained from the route mean squared deviation of z-coordinates of phosphorus atoms using the formula[59]

$$\langle \Delta z\rangle = \sqrt{(\frac{\sum_i^N z_i - \langle z\rangle^2}{N})} \tag{2.9}$$

where z_i indicates the z-coordinate of i'th lipid molecule and $\langle z\rangle$ is the average z position of the lipid molecules.

2.3 Results & Discussions

The equilibration of each system in the MD simulation was ensured through the convergence of the area per lipid $\langle A_{PL}\rangle$ of the DPPC bilayer with time (Figure 2.2). We show $C(\Delta t)$ of the respective system in the insets. From exponential fitting to $C(\Delta t)$ vs Δt plot, we find the correlation times of $C(\Delta t)$ are close to 1ns to 2 ns for each system (Table 2.1), which is consistent with previous reports.[53] We divide the equilibrium trajectory into eight equal windows consisting of snapshots of 50 ns. The time interval is sufficiently large to ensure the decay of $C(\Delta t)$, and the blocks can be treated as independent ones to estimate mean and standard error of the mean of different quantities. The equilibrium snapshots of different systems are shown in Figure 2.3.

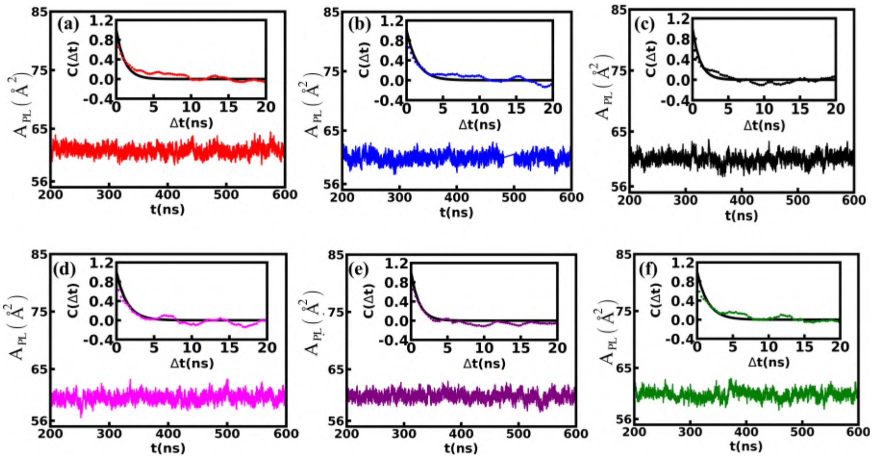

Figure 2.2: Area per lipid and its time correlation function (inset) of (a) DPPC 512 (b) DPPC 512 + 10 HA5 (n_{HA5}=10) (c) DPPC 512 + 30 HA5 (n_{HA5}=30) (d) DPPC 512 + 50 HA5 (n_{HA5}=50) (e) DPPC 512 + 150 HA1 (N=1) (f) DPPC 512 + 15 HA10 (N=10)

system	correlation time (ns)
n_{HA5}=0	1.3
n_{HA5}=10	1.5
n_{HA5}= 30	1.3
n_{HA5}= 50	1.8
N=1	1.5
N=5	1.3
N=10	1.7

Table 2.1: Correlation time of $\langle A \rangle$ for different cases with 512 DPPC bilayer

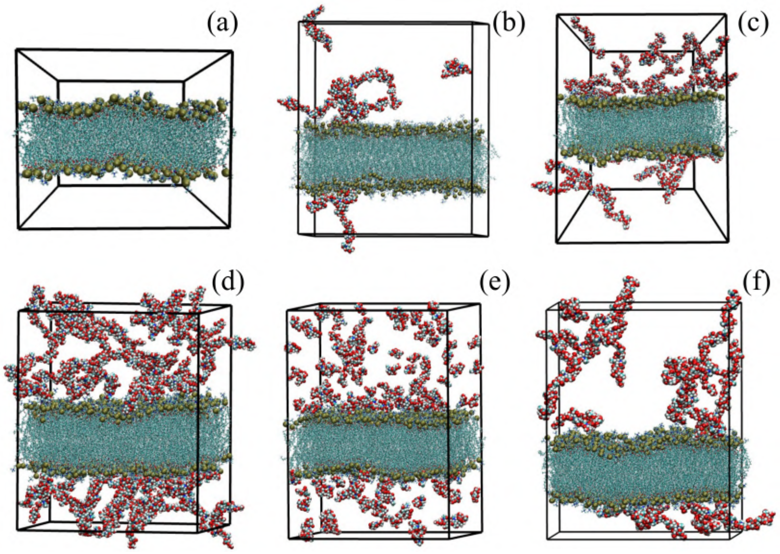

Figure 2.3: Typical equilibrium snapshot of (a) n_{HA5}=0 (b) n_{HA5}=10 (c) n_{HA5}=30 (d) n_{HA5}=50 (e) N=1 (f) N=10. Water molecules are not shown for clarity.

2.3.1 Density profile of the molecular constituents

Density profiles of the molecular constituents describe the preferred location of the molecules in the system. We calculate the density profile of the oxygen atoms of the water molecules($\rho_w(z)$), phosphorus atoms of DPPC bilayer ($\rho_P(z)$) and the center of mass (com) of the Hyaluronic acid chains ($\rho_{HA}(z)$) along the normal direction to the bilayer plane (z-axis in our case) with origin at the bilayer center.

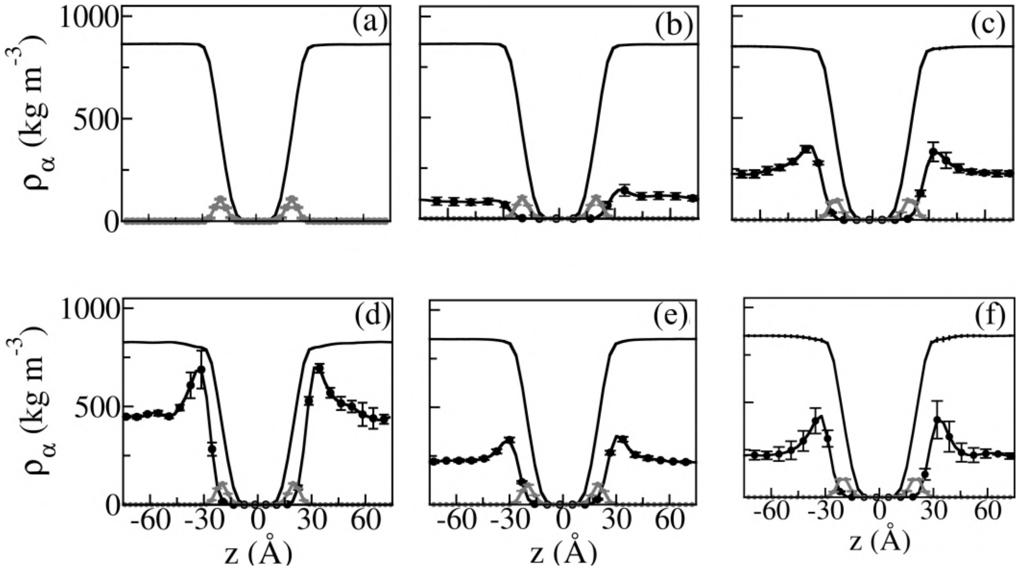

Figure 2.4: Density profile of water (ρ_w) [*solid black* line], Phosphorus atoms (ρ_P) [*solid gray* line] and HA (ρ_{HA}, scaled up with a factor of 5.0) [*dotted black* line] for (a) n_{HA5} =0, (b) n_{HA5} =10, (c) n_{HA5} =30 (d)n_{HA5}=50, (e) N=1 and (f) N=10. α stands for w(water),P(phosphorus atoms) or HA(HA com).

Figure 2.4(a)-(d) shows $\rho_P(z)$, $\rho_W(z)$ and $\rho_{HA}(z)$ (scaled up with a factor of 5.0 for better data visualization) for different n_{HA5}. The peak observed in the $\rho_P(z)$ profile at a distance of 20 Å from the bilayer center indicates bilayer separation of about 40 Å, which is consistent with known bilayer thickness.[60] $\rho_W(z)$ vanishes at the bilayer center, as water does not enter the hydrophobic core of the membrane. It increases rapidly in the DPPC-water interfacial region and reaches the bulk water density at $\approx$ 15Å far from the peak of $\rho_P(z)$. For $\rho_{HA}(z)$ we observe peaks at about $\approx$ 15Å far from the peak of $\rho_P(z)$, almost where the bulk density of water sets in. The peak location of ρ_{HA}(z) indicates the accumulation of HA molecules and the formation of an interface between HA-water and the DPPC bilayer. Figure 2.4(e)-(f) show the density profiles of the same molecules for different N, which is similar to what we obtain for different n_{HA5}. We note that the water density profile is sensitive neither to HA concentration (n_{HA5}) nor HA aggregation state (N). Thus, the HA molecules interact with the lipid molecules indirectly via water molecules.

To ensure the role of water in HA-DPPC interaction, we further calculate the radial

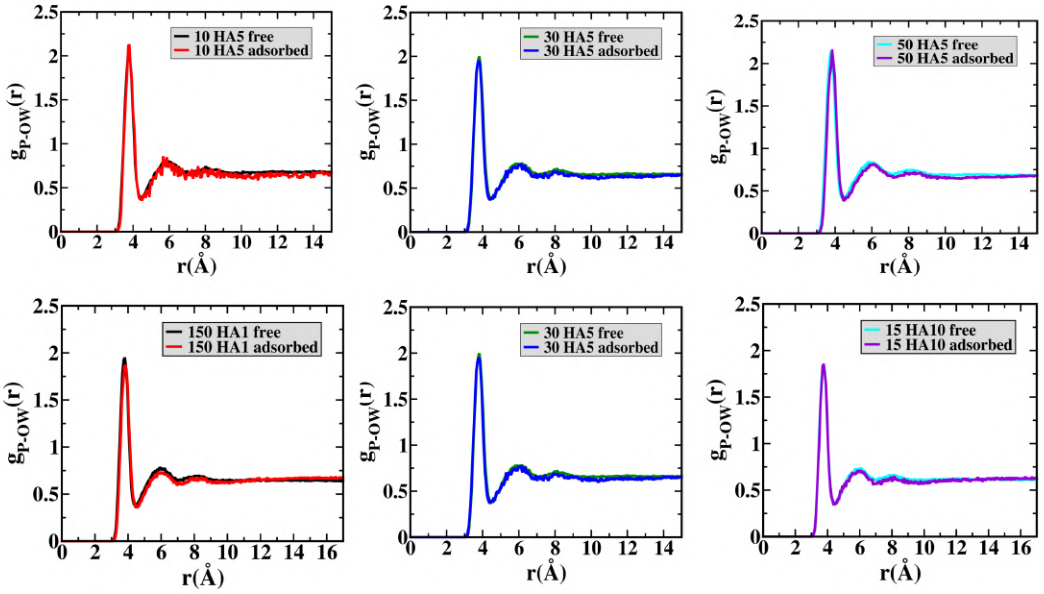

Figure 2.5: Radial Distribution Function of oxygen atoms of water (OW) around P of DPPC for free and adsorbed lipids for various cases indicated in the legends.

distribution function (rdf) of OW atoms of water around P atoms, $g_{P-OW}(r)$, for free and adsorbed lipids (shown in Figure 2.5), where r is the distance between P and OW atoms. Here the lipid molecules are categorized into free lipids if the P atoms of the molecules are not within a cutoff distance of 7Å from any heavy atoms of HA molecules. Inside this cutoff, lipids are labeled as adsorbed lipids. Our calculations show that $g_{P-OW}(r)$ remains the same for both free and adsorbed lipids, across different systems. This implies that HA molecules do not alter the hydration nature of the DPPC molecules and, thus, emphasizes the importance of water-mediated interaction between HA and DPPC. The data are consistent with earlier reports.[59]

2.3.2 Area compressibility Modulus

Next, we proceed to study if HA chains have any effect on the elastic properties of the bilayer. To that end, we calculate the area compressibility modulus k_A using equation 2.3 of the lipid bilayer. Figure 2.6(a) and 2.6(b) show the lipid bilayer area $\langle A \rangle$ (relative to the area of the bilayer for n_{HA5}=0) for different n_{HA5} and N respectively. We find that the $\langle A \rangle$ remains almost unchanged for different n_{HA5} and N. Hence the overall structure of the bilayer remains intact in presence of HA chains.

As $\langle A \rangle$ is not affected by n_{HA5} or N, the dependence of k_A on n_{HA5} and N is completely determined by $\langle \delta A^2 \rangle$. This leads us to consider $\langle \delta A^2 \rangle$ in detail. To investigate if there is any system size dependence of the equilibrium fluctuation $\langle \delta A^2 \rangle$, we compute the $\langle \delta A^2 \rangle$

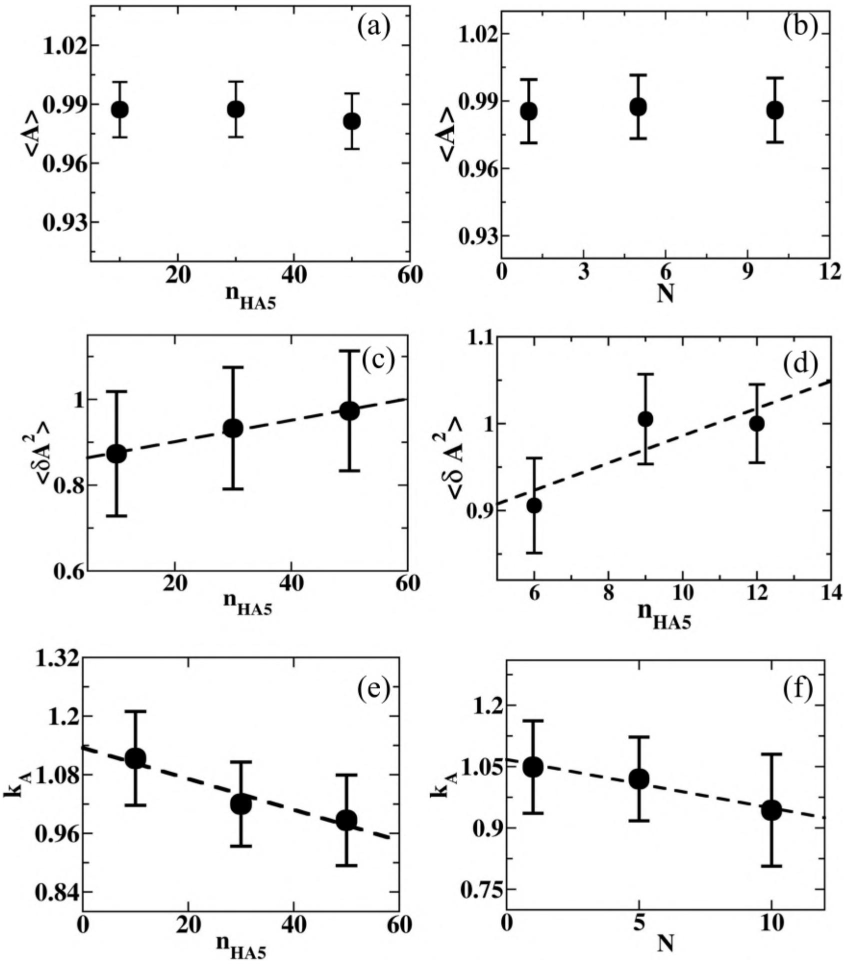

Figure 2.6: (a) Relative area ($< A >$) for different n$_{\text{HA5}}$. (b) for different N values. Relative area fluctuation $< \delta A^2 >$ with n$_{\text{HA5}}$ for (c) 512 DPPC bilayer and (d) 128 DPPC bilayer. Relative compressibility modulus k_A for different (e)n$_{\text{HA5}}$ and (f) for different N.

of the bilayers of 512 and 128 DPPC molecules, respectively. For 128 DPPC molecules, we consider 6,9 and 12 HA pentamers (namely, n$_{\text{HA5}}$=6,9 and 12). We show the relative variation of $\langle \delta A^2 \rangle$ with respect to HA-free cases for different n$_{\text{HA5}}$ in Figure 2.6(c) and 2.6(d) respectively for both systems. We find $\langle \delta A^2 \rangle$ increases linearly with n$_{\text{HA5}}$, hence the trend is independent of the system size.

Figure 2.6(e) shows the variation of k_A with n$_{\text{HA5}}$. k_A drops linearly with n_{HA5}. Figure 2.6(f) shows a linear decline in k_A with N, in similar to the dependency on n$_{\text{HA5}}$. The reduction in k_A with n$_{\text{HA5}}$ and N, implies that the membrane exhibits improved elastic flexibility as HA concentration and HA chain size increase.

2.3.3 Bending Modulus

We also calculate the bending modulus, k_c of the DPPC bilayer for different cases from the equilibrium height fluctuation of the bilayer using equation 2.4 (see details in *Methods*).

We note that equation 2.4 is valid in the limit of $q \rightarrow 0$. For a small system, where

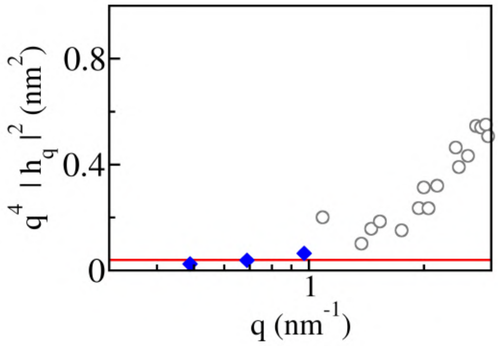

Figure 2.7: k$_c$ calculation for n$_{\mathrm{HA5}}$=50. $q^4|h_q|^2$ data at small q values (points shown by triangles) are fitted with a constant line (the red line) to obtain k_c

the bilayer thickness is comparable to the box size and the bilayer cannot be assumed as a "thin sheet", this equation does not hold.[55] We show a typical $q^4|h_q|^2$ vs q plot for n$_{\mathrm{HA5}}$=50 in Figure 2.7. The data corresponds to a constant value at small q values from where one can extract k_c.[54]

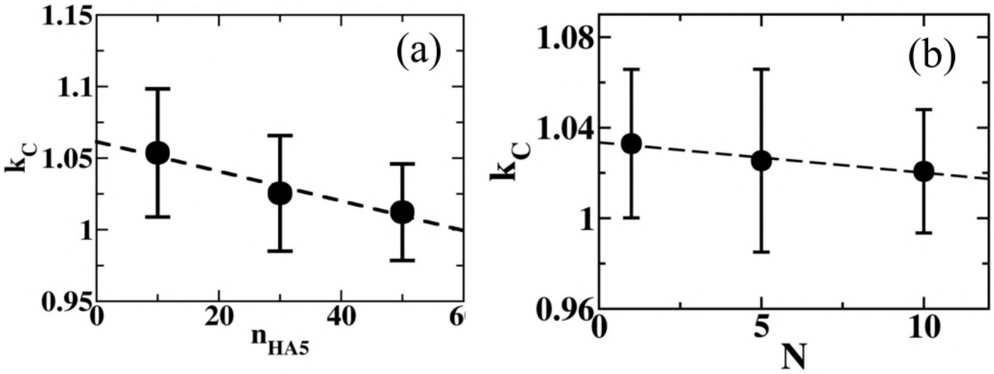

Figure 2.8: Relative Bending modulus k_C for different (a) n$_{\mathrm{HA5}}$ and (b) for different N

Figure 2.8(a) shows relative bending modulus k_c versus n$_{\mathrm{HA5}}$, and k_c versus N data are shown in Figure 2.8(b). We find k_c decreases with increasing n$_{\mathrm{HA5}}$ and N within the error bars. The qualitative trends are similar to those of k_A. Thus, k_A and k_c of a DPPC lipid bilayer decrease with increase in both n$_{\mathrm{HA5}}$ and N, suggesting softening of the bilayer. This is qualitatively similar to the experimental observations.[19] The effects of n$_{\mathrm{HA5}}$ appears to be stronger than those of N.

2.3.4 Microscopic explanation of the observed results

We find that the interaction between HA molecules and the DPPC bilayer is mediated via water. Therefore, we investigate whether the interfacial water molecules respond to the variation in n_{HA5}. Here, we only focus on n_{HA5} because of the strong dependence of elastic modulus on n_{HA5} rather than on N. We compute the tetrahedral order parameter Q_{Tr} of water molecules (see details in *Methods* section) at the HA-DPPC interface for different n_{HA5}. The HA-water and DPPC interface is spanned along the bilayer normal from the peak of $\rho_P(z)$ up to the peak of $\rho_{HA}(z)$, which is ≈ 15 Å above and below of the peak of $\rho_P(z)$. Figure 2.9(a) illustrates the variation of Q_{Tr} (averaged over all interfacial waters) with n_{HA5}. We find that the Q_{Tr} decreases as n_{HA5} increases. The physical reason is as follows: HA pentamers take random orientation at the interface and at the same time form hydrogen bonds with the interfacial water molecules. Hence, the water molecules hydrating the HA molecules become disordered and it increases with HA concentration. In figure 2.9(b) we describe the variation of k_A with Q_{Tr}. We find that k_A increases as Q_{Tr} increases. Thus, the disorder in the tetrahedral network helps the membrane to fluctuate more.

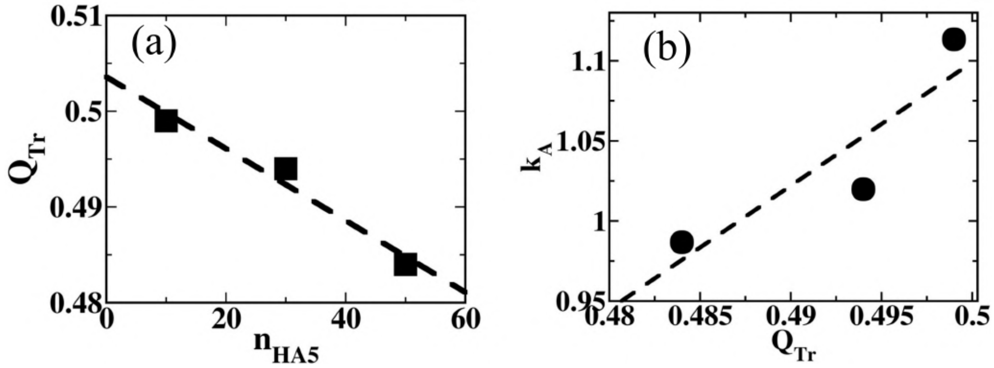

Figure 2.9: (a) tetrahedral order Q_{Tr} of interfacial water molecules vs n_{HA5} (b) k_A vs Q_{Tr}

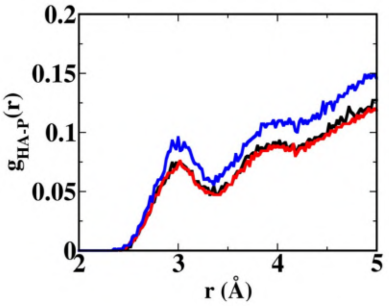

Figure 2.10: RDF of P atoms of DPPC around heavy atoms of HA, g_{HA-P} (r) for n_{HA5} = 10 (black), 30 (red), and 50 (blue).

We further investigate the mechanistic picture leading to this behavior. We calculate the rdf of P atoms around the heavy atoms of HA ($g_{HA-P}(r)$), where r is the distance between P and any heavy atoms of HA. The data in Figure 2.10 show the first peak around r = 3 Å , and the peak height increases with n_{HA5}. This behavior along with Q_{Tr} data in figure 2.9(a) suggests that the disorder in the tetrahedral network of water helps the HA to approach the P atoms better.

Next, we compute the order parameter of acyl chains (S_{CD}) for both HA-free lipids and HA-adsorbed lipids (see section 2.3.1 for their definitions). Lipid hydrocarbon chains are defined as sn1 and sn2 chains for chains attached to the sn1 and sn2 positions of the glycerol moiety (see Figure 2.1(b)). We calculate S_{CD} for both the chains and show S_{CD} of both free and adsorbed lipid species for varying n_{HA5} in Figure 2.11. Our calculations show an increase in S_{CD} of both lipid chains when HA is adsorbed to the DPPC molecules, suggesting an increase of order in the lipid tails.

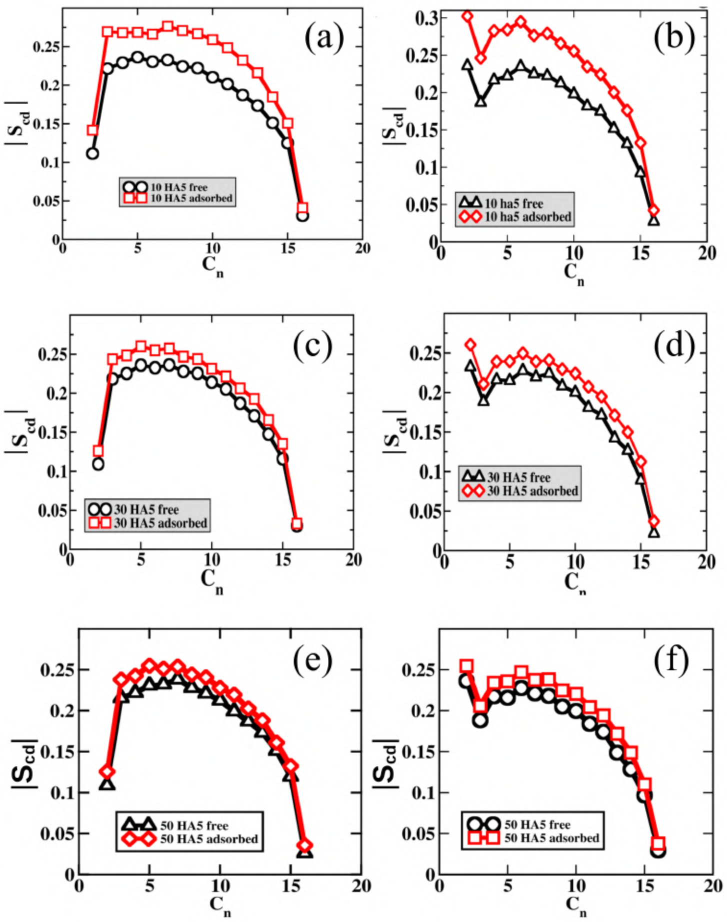

Figure 2.11: S_{CD} of sn1 and sn2 chain of free (black) and adsorbed lipids (red) for n_{HA5} = 10 (a:sn1, b:sn2), n_{HA5} = 30 (c:sn1, d:sn2), n_{HA5} = 50 (e:sn1, f:sn2).

We also compute the mean thickness of the membrane (d_{P-P}) and the roughness Δ_z of the HA-adsorbed lipids for different n_{HA5}. We show the variation of d_{P-P} and Δ_z with n_{HA5} in figure 2.12(a) and 2.12(b) respectively. We find both d_{P-P} and Δ_z increase with increasing n_{HA5}. Thus, the ordering of the tails enhances the registry between successive lipid molecules facilitating both out-of-plane and lateral movements so that

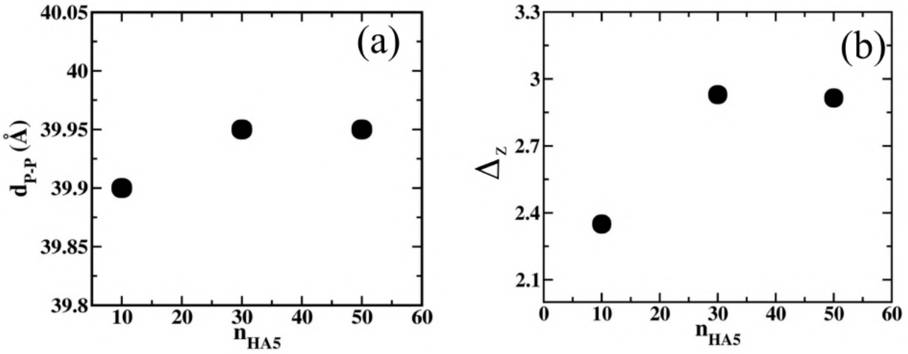

Figure 2.12: (a) Mean thickness of the bilayer as a function of n_{HA5}. (b)Surface roughness of the HA-adsorbed lipids as a function of n_{HA5}

the area per lipid shows more fluctuations.

AFM experiments show that the rigidity of HA-coated cancer extracellular vesicles (EVs), where HA molecules are abundant, decreases in comparison to normal EVs. Similarly, the photophysical hydration dynamics data show that as HA chains are externally added to the Hyaluronidase enzyme-treated EVs, a flexible environment is induced around the EVs.[19] These two experimental results are qualitatively consistent with the simulation results showing the reduction of k_A with increasing n_{HA5}. Experimentally we further observe that the EV membrane becomes less flexible by adding hyaluronidase, which promotes HA degradation. This is also consistent qualitatively with the decrease of k_A with increasing N observed in the simulations.

It may be noted that the polar and hydrophilic ligands like TAT polypeptide,[5] glyphosphate,[6] polycation,[7] hydronium ions,[61] and diols[62] stay in the vicinity of the headgroups of the lipid bilayer, while hydrophobic ligands like polystyrene[8] or amphipathic ligands like quercetin[9] penetrates into the bilayer. In such cases the bilayer shows substantial deformation and changes in elastic properties. However, the water-mediated elastic response of the bilayer without a prominent structural deformation in the presence of HA has not been reported so far to the best of our knowledge. Our primary experimental observations on the elastic response of the EV membrane induced by HA can be understood in the light of water-mediated interaction between HA and bilayers.

2.4 Conclusion

In this chapter, we have investigated the elastic response of a DPPC bilayer to hyaluronic acid (HA) chains of varying concentrations and sizes. Our findings indicate that the elastic properties of the bilayer, such as the area compressibility modulus (k_A) and bending modulus (k_c), decrease with increasing HA concentration and chain size. This implies that the bilayer becomes more flexible with HA concentration and chain size where the effect of HA concentration is stronger than HA chain size. We note that the increase in HA concentration leads to the disordering of interfacial water molecules while enhancing the lipid chain ordering in HA-adsorbed lipids. As a result, there is an increase in the fluctuation of area per lipid and overall elasticity of the bilayer.

Our results are in qualitative agreement with atomic force microscopy (AFM) experiments and could be relevant in applications such as the design of HA-coated liposomes and in biomedical fields like arthritis treatment and cancer therapy. However, we note that our atomistic model is a simplified representation of the physiological environment. To capture a more realistic picture, future studies could incorporate HA-receptor proteins and longer HA chains where employing a coarse-grained modeling approach would likely prove effective.

Appendix

A2.1 Molecular dynamics simulation

Molecular dynamics (MD) simulation is a computational technique used to calculate both static and dynamic properties of classical many-body systems.[63] In MD, we start with a model system and simulate their behavior by solving Newton's equations of motion. Through the 'Force' part of Newton's equation of motion, we account for the interactions between particles via an interparticle potential. By solving the equations of motion, we generate trajectories of all particles in the phase space.

Consider a system having N particles in 3-dimension. We denote the mass, position, and momenta of the i'th particle as m_i, $\vec{r_i}$ and $\vec{p_i}$ respectively. These particles interact via the potential energy $V(r_{ij})$ where $r_{ij} = |\vec{r_i} - \vec{r_j}|$, $|\vec{r_i}$ being the position vector of the i'th particle. In reality, systems like polymers or peptides in solution have complex interaction energy terms that can be bonded and non-bonded (more on these in the next section *'Force fields for molecular simulation'*). In MD, we obtain force on the i'th particles F_i due to all other particles by taking the gradient of the interacting potential i.e. $\vec{F_i} = \sum_{j=1}^{N} \nabla_j V(r_{ij})$. Subjected to the force and given the initial positions and momenta at time t_0, we integrate Newton's equation of motion and get the position and momenta for any later time. To integrate the equation of motion we follow the *leap-frog* algorithm.

The leap-frog algorithm uses positions $\vec{r}$ at time t and velocities $\vec{v}$ at time $t - \frac{\Delta t}{2}$. From the positions at time t, it computes acceleration at time t, $\vec{a_i}(t) = \vec{F_i}[\vec{r_i}(t)]/m_i$. Finally, it updates the positions at time $t + \Delta t$ and velocities at $t + \frac{\Delta t}{2}$. Mathematically, using Taylor series expansion the equations for updating position and velocity are as follows:

$$\vec{v_i}(t + \frac{\Delta t}{2}) = \vec{v_i}(t) + \frac{\Delta t}{2}\vec{a_i}(t) + \mathcal{O}(\Delta t^2)$$

$$\implies \boxed{\vec{v}_i(t+\frac{\Delta t}{2}) = \vec{v}_i(t-\frac{\Delta t}{2}) + \Delta t \vec{a}_i(t) + \mathcal{O}(\Delta t^2)} \tag{A2.1.1}$$

$$\vec{r}_i(t+\Delta t) = \vec{r}_i(t) + \Delta t \vec{v}_i(t) + \frac{\Delta t^2}{2}\vec{a}_i(t) + \mathcal{O}(\Delta t^3)$$

$$\implies \boxed{\vec{r}_i(t+\Delta t) = \vec{r}_i(t) + \Delta t \vec{v}_i(t+\frac{\Delta t}{2}) + \mathcal{O}(\Delta t^3)} \tag{A2.1.2}$$

A2.2 Force fields for molecular simulation

In molecular modeling, a force field is a collection of equations and associated constants used to model the bonden and non-bonded potential energy of a system. Examples of widely used force fields in molecular simulations include *CHARMM*(all-atom foce-field), *OPLS*(all-atom force-field), *GROMOS*(united-atom force-field), etc. which are designed to reproduce the molecular geometry and various properties of systems. The parameters of the force field are derived based on semi-empirical quantum mechanical calculations or by fitting experimental data like X-Ray, neutron and electron diffraction, NMR etc.

A general form of a force field includes both bonded and non-bonded terms and can be expressed as follows:

$$U_{\text{total}} = U_{\text{bonded}} + U_{\text{non-bonded}} \tag{A2.2.1}$$

where

$$U_{\text{bonded}} = \sum_{\text{bonds}} k_b(r-r_0)^2 + \sum_{\text{angles}} k_\theta(\theta-\theta_0)^2 + \sum_{\text{dihedrals}} k_\phi\left(1+\cos(n\phi-\delta)\right)$$

represents the bonded interactions, which include bond stretching, angle bending, and dihedral (torsional) interactions. Here, k_b, k_θ, and k_ϕ are force constants, r_0 and θ_0 are equilibrium bond length and angle, ϕ is the dihedral angle, n is the periodicity, and δ is the phase angle.

The non-bonded interactions are given by

$$U_{\text{non-bonded}} = \sum_{i<j}\left(\frac{A_{ij}}{r_{ij}^{12}} - \frac{B_{ij}}{r_{ij}^{6}}\right) + \sum_{i<j}\frac{q_i q_j}{4\pi\epsilon_0 r_{ij}}$$

where the first term represents van der Waals interactions, while the second term represents electrostatic interactions. A_{ij} and B_{ij} are the Lennard-Jones parameters, r_{ij} is the distance between particles i and j, q_i and q_j are the partial charges on the particles, and ϵ_0 is the permittivity of free space.

A2.3 Periodic boundary condition and minimum image convention

In MD simulations, the system is initially confined within a finite simulation box. To mimic an infinite bulk system, periodic boundary conditions (PBC) are applied in all directions. With PBC, the finite box of length L is effectively surrounded by an infinite array of its own replicas, allowing atoms that exit one side of the box to re-enter from the opposite side. This setup mitigates surface effects, which otherwise would cause particles near the boundaries to experience different forces than those in the bulk region.

During the simulation, PBC is combined with the minimum image convention,[63] which ensures that each particle interacts with the closest image of any other particle, whether in the primary box or a neighboring replica. To further reduce computational cost, a cutoff distance r_c (where $r_c < L/2$) is applied to truncate long-range interactions. This cutoff prevents a particle in the central box from interacting with its own periodic images in adjacent replica boxes, thus reducing the computational cost. This approach helps in minimizing the computational expense while preserving the bulk properties of the system.

A2.4 Controlling the temperature

In MD simulations, it is essential to maintain the system at a constant temperature and pressure to accurately mimic real-world conditions. To control the temperature throughout our simulations, we employed the Nosé-Hoover thermostat.[49] Here the system is extended by introducing a fictitious dynamical variable $\tilde{s}$ with associated mass parameter Q and velocity $\dot{\tilde{s}}$. The magnitude of Q determines the coupling between the reservoir and the real system. Due to the additional variable, the extended system has $(3N+1)$ degrees of freedom, where N is the number of particles in the system. Particle coordinates remain the same in the extended system as in the real system; $\tilde{r} = r$, while the role of $\tilde{s}$ is to scale the time in the extended system; $d\tilde{t} = \tilde{s}\,dt$. Thus, the velocities of particles in the extended system can be written as $\dot{\tilde{r}} = \tilde{s}^{-1}\dot{r}$. The Lagrangian for the extended system can be written as:

$$L = \sum_i \frac{1}{2m_i\tilde{s}^2}\dot{\tilde{r}}_i^2 - U(\tilde{r}) + \frac{Q\dot{\tilde{s}}^2}{2} - (N+1)k_BT_0 \ln \tilde{s}$$

The first two terms of equation (2.24) represent the kinetic energy minus the potential energy of the real system, while the last two terms are the kinetic energy minus the potential energy of $\tilde{s}$. At steady state ($\dot{\tilde{s}} = 0$), the system describes the canonical ensemble and the kinetic energy is given by $\frac{3}{2}(N+1)k_BT$ as required by equipartition. The corresponding equations of motion are:

$$\boxed{\ddot{\tilde{r}}_i = \frac{F_i}{m_i \tilde{s}^2} - \frac{2\dot{\tilde{s}}}{\tilde{s}}\dot{\tilde{r}}_i} \tag{A2.4.1}$$

$$\boxed{\ddot{\tilde{s}} = \frac{1}{Q\tilde{s}}\left(\sum_i m_i \tilde{s}^2 \dot{\tilde{r}}_i^2 - (N+1)k_B T_0\right)} \tag{A2.4.2}$$

These can be solved using time integration algorithms. The extended system describes the micro-canonical ensemble, but since the real system is allowed to exchange energy with $\tilde{s}$, it can be shown that in the asymptotic limit, the real system describes the canonical ensemble. In our investigations, we have used the Nose-Hoover thermostat for temperature control.

A2.5 Controlling the pressure

In real systems the pressure is usually well defined, hence controlling pressure is essential during simulation. A number of algorithms exist for controlling the pressure in molecular simulations, one of the simple ones being the Berendsen barostat,[64] in which the pressure is controlled by multiplying the box dimensions by a global factor ζ. The pressure in a system of N particles in a volume V at temperature $T(t)$, is given by

$$P = \rho T(t) + \frac{1}{3V}\sum_i \sum_{j\neq i} \vec{f}(r_{ij}) \cdot \vec{r}_{ij},$$

with ρ the density, $\vec{f}_{ij}$ the force on particle i due to particle j, and $\vec{r}_{ij}$ the displacement vector from i to j. If the target pressure is P_0, then the volume scaling factor can be expressed as:

$$\zeta = 1 - \frac{\Delta t}{3\tau_p}(P(t) - P_0),$$

where $P(t)$ is the current pressure and τ_p is a coupling factor that determines the rate at which the pressure is scaled toward the target pressure P_0. Re-scaling the simulation box volume in this way at every time step of the simulation may lead to strong oscillations of pressure. The more stable Parrinello-Rahman barostat,[50] which uses an extended ensemble approach similar to the Nose-Hoover method, has been used in our investigations.

A2.6 Particle Mesh Ewald (PME) Methods

Electrostatic interactions between atoms or molecules are usually modeled by the Coulomb potential, which is given by:

$$U_{\text{electrostatic}}(r_{ij}) = \frac{1}{4\pi\epsilon_0}\frac{q_i q_j}{r_{ij}}$$

where ϵ_0 is the dielectric constant for vacuum, q_i and q_j are the partial charges on particles i and j, and r_{ij} is the distance between these two charges. Summation of long-range electrostatic potential for infinite neighboring atoms and periodic images are not convergent. To handle this, the charge distribution in the central simulation box is separated into two parts:[51]

$$\rho_i(r) = \rho_i^S(r) + \rho_i^L(r) \tag{A2.6.1}$$

where

$$\rho_i^S(r) = q_i\delta(r - r_i) - q_i G_\sigma(r - r_i), \quad \rho_i^L(r) = q_i G_\sigma(r - r_i).$$

Here, q_i is the charge at position r_i, and $G_\sigma(r - r_i) = \frac{1}{(2\pi\sigma^2)^{3/2}} e^{-\frac{|r|^2}{2\sigma^2}}$ represents a Gaussian fictitious screening charge distribution. The summation for the short-range component is evaluated in real space, while the long-range component is approximated in Fourier space. In practice, the central simulation box is partitioned into a grid, and the point charges are spread across the nearest grid cells via interpolation. This results in a grid of uniformly spaced charges, which allows us to perform the Fast Fourier Transform (FFT) of the periodic images. The inverse fast Fourier transform is then performed to obtain the long-range contribution in real space.

Chapter

3

Dynamics of aqueous suspension of short hyaluronic acid chains near DPPC bilayer*

3.1 Introduction

In the previous chapter we have explored the mechanical response of DPPC lipid bilayer to Hyaluronic acid (HA) chains. We show that the HA-DPPC interaction is water-mediated and they form an interface. We also show that the cancer extracellular vesicles (EVs) with high hyaluronic acid (HA) content are softer than normal EVs with lower HA levels.[19] The organization of the HA chains in the vicinity of cell membranes and the synergy between HA and lipid molecules play vital roles in maintaining the viscoelasticity of the synovial fluids, elasticity of cells, and so on.[20,36,65,66] Moreover, HA provides extreme lubrication to synovial joints along with lubricin and phosphatidylcholine.[67] To understand the interfacial lubrication and viscous properties of HA chains, it is important to study the interfacial dynamics of the molecular constituents at the HA-DPPC interface.

Fluorescence anisotropy and solvent relaxation data indicate that the EVs' flexibility is due to the weak water networks associated with the low-molecular-weight HA chains.[19] Using molecular dynamics (MD) simulation, Zhang et al. have demonstrated recently that short HA chains influence water mobility and permeation rate through aquaporin proteins.[68] The bulk properties of HA solutions are well investigated in literature,[22,23,69] however, to the best of our knowledge, no detailed investigation has been conducted on the dynamic micro-environment near cell membranes in the presence of short HA chains, despite its importance in many contexts including therapeutic development. In this chapter, we examine the interfacial dynamics of water, HA chains, and lipid molecules for varying HA concentrations and HA chain sizes using molecular dynamics (MD)

---

*Based on the publication: **Anirban Paul** and Jaydeb Chakrabarti. Dynamics of an Aqueous Suspension of Short Hyaluronic Acid Chains near a DPPC Bilayer. Phys. Chem. Chem. Phys. 26 (2024): 20440–49. (https://doi.org/10.1039/D4CP01088D) simulation. The dynamics of the DPPC and HA-water interface are studied in detail. We observe that while the HA chains remain slightly apart from the bilayer without making direct contact, water makes direct contact with the bilayer at the interface. At the HA–water and DPPC interface, the residence times of the water molecules are approximately tens of picoseconds (ps), whereas the HA monomers have residence times of hundreds of picoseconds.

We also note that the dynamical behaviors at the interface respond differently to the concentration of the HA monomers and the HA chain size. The water contact layer exhibits sub-diffusive dynamics in translation parallel to the bilayer plane and rotational motion as well. Beyond the contact layer, the motion of the water molecules is diffusive, where both the translational and rotational MSDs increase linearly with time. We find that the translational and rotational diffusion coefficients of water in this region decrease with increasing HA concentration but are not sensitive to HA chain size. Additionally, at the interface, the HA chains show sub-diffusive translation but diffusive rotational motion. With increasing HA concentration, the rotational diffusion coefficient of the chains decreases; however, for large chains, this quantity is independent of HA chain sizes. We also find that the in-plane translational diffusion of the lipid headgroups increases as the concentration of HA increases, but it varies slightly with the size of the HA chain. In contrast, the rotational diffusion of lipid PN vectors decreases with HA concentration but increases monotonically with HA chain size.

3.2 Methods

3.2.1 Force field details and MD simulation

We investigate the interfacial dynamics of the same systems discussed in the previous chapter in *Section* 2.2.1. We follow the same protocol while preparing and simulating the systems as described there. The dynamics data that are reported here, are averaged over three MD trajectories starting from different equilibrium configurations and stored at the time interval of 0.5ps.

3.2.2 Analysis

Residence Time Calculations

We define a function, $P_i(t)$, such that $P_i(t) = 1$ if the z-coordinate of the i-th molecule of a given species stays at the interface and $P_i(t) = 0$, if not. Then the survival probability of species α is defined by[70]

$$S^{\alpha}(t) = \sum_{i=1}^{N_\alpha} \langle \Pi_{t_k=t_0}^{t_0+t} P_i(t_k) \rangle \tag{3.1}$$

Here N_α is the total number of species in the system. Angular bracket implies average over multiple time origin t_0. We fit a bi-exponential function of the form $ae^{-t/\tau_1} + (1-a)e^{-t/\tau_2}$ to the survival probability and obtain the average residence time as $\tau_\alpha = a\tau_1 + (1-a)\tau_2$.

Translational and Rotational Mean Squared Displacements

Translational MSD:
The translational mean squared displacements (MSD) of a chemical moiety α at the HA-water and DPPC interface along the bilayer plane (xy plane in our case) are calculated using the formula:

$$< r_\alpha^2(t) >= \frac{1}{N_\alpha} \sum_{i=1}^{N_\alpha} < (x(t)-x(0))^2 + (y(t)-y(0))^2 > \tag{3.2}$$

Here α =W,α =H, α =P stands for water, HA monomers, and phosphorus atoms of the bilayer respectively. $< r_\alpha^2 >$ is computed over only those molecules which remain at the interface continuously for time t.[52] Their number is indicated by N_α here. The angular bracket denotes the average over multiple time origins. While computing the lateral mean squared displacement of the phosphorus atoms of the lipid bilayer, the COM motion of the respective leaflet is removed for each lipid molecule.[71,72]
Rotational MSD:
The rotational MSD $\langle \phi_\alpha^2 \rangle$ of α, is computed using the following definition[70,73]

$$\langle \phi_\alpha^2(t) \rangle = \frac{1}{N_\alpha} \sum_{i=0}^{N_\alpha} \langle |\vec{\phi}_i(t_0+t) - \vec{\phi}_i(t_0)|^2 \rangle \tag{3.3}$$

Here t_0 is an arbitrary time origin and the vector rotational displacement $\vec{\phi}_i(t_0+t)$ is the sum of infinitesimal angular displacements $\delta\vec{\phi}_i$ of a suitably chosen vector associated with the molecule from $\vec{\phi}_i(t_0)$ to $\vec{\phi}_i(t_0+t)$ in discrete time steps δt. Mathematically, $\vec{\phi}_i(t_0+t) - \vec{\phi}_i(t_0) = \int_{t_0}^{t_0+t} \delta\vec{\phi}_i(t')$.[25,73] For water and HA $\vec{\phi}_i(t)$ ($\vec{\phi}_i(t) \equiv \vec{\phi}_w(t)$ and $\vec{\phi}_i(t) \equiv \vec{\phi}_h(t)$) is calculated from the water dipole vector μ_i^w and HA end-to-end vectors. For lipids, $\vec{\phi}_{pn}(t)$ is calculated using the projection of the P-N vector in the xy plane.[74]

For water, the magnitude of $\delta\vec{\phi}_w$ is $cos^{-1}[\hat{\mu_i^w}(t).\hat{\mu_i^w}(t+\delta t)]$ and its direction is along $\hat{\mu_i^w}(t) \times \hat{\mu_i^w}(t+\delta t)$. Note that any suitably chosen vector other than μ_i^w can be used to describe the rotational diffusion, but they yield the same qualitative conclusion.[73,75,76]

For HA and PN vectors, we follow the same method as well. With this technique $\vec{\phi}_i(t)$ becomes an unbounded variable. N_α in equation 3.3 indicates the number of α species at the interface throughout the time interval of t. $\langle\phi_\alpha^2\rangle$ is fitted with a straight line to acquire the rotational diffusion D_R^α of α at the interface.[70]

$$D_R^\alpha = \lim_{t\to\infty} \frac{1}{4t}\langle\phi_\alpha^2\rangle \tag{3.4}$$

For waters, we also compute rotational correlation time τ_l^W from rotational autocorrelation function.[52] We verified that the product of τ_l^W and D_R^W remains constant.[77]

The error bars for the residence times and diffusion coefficients are derived from the standard deviation of the respective quantities from three separate MD runs divided by the square root of the number of runs.[53] While scaling the data by HA-free cases (see Results), we compute the error bars using the error propagation method of division.[78]

Orientational autocorrelation function

The orientational autocorrelation function ($C(\tau)$) is computed over only those water molecules that continuously stay at the interface. $C(\tau)$ is defined as follows :

$$C(\tau) = \langle\frac{\vec{\mu_i}(\tau).\vec{\mu_i}(\tau)}{\vec{\mu_i}(0).\vec{\mu_i}(0)}\rangle \tag{3.5}$$

where $\vec{\mu_i}(\tau)$, the dipole vector of the ith water molecule at time τ, is defined as the vector pointing from the oxygen atom to the center of mass of two hydrogen atoms.[52] C(τ) is fitted with a bi-exponential function of the form $C(\tau) = a_1 e^{-\tau/t1} + (1-a_1)e^{-\tau/t2} + b$ to obtain different timescales. The parameter b is used to take care of the long-lived tail of the C(τ). The average orientation timescale is obtained by τ^{w} = $a_1 t_1 + (1-a_1)t_2$.

Cross-chain Radial Distribution

We compute cross-chain radial distribution function g_{xy}(r) of the HA monomers the parallel plane to the bilayer (xy plane) using the following formula:[79]

$$g_{xy}(r) = \langle\frac{1}{\rho_N N}\sum_{i=1}^{N}\sum_{j=1}^{N}\delta(|\vec{r_i}-\vec{r_j}|_{xy} - r)\rangle \tag{3.6}$$

Here $\vec{r_i}$ and $\vec{r_j}$ indicates position vector of the com of two HA monomers belonging to different chains at the interface, $r = \sqrt{x^2+y^2}$, $|\vec{r_i}-\vec{r_j}|_{xy} = \sqrt{(x_i-x_j)^2+(y_i-y_j)^2}$ and ρ_N implies the areal monomer density (in xy plane) at the interface. N is the number of beads at the interface. Angular bracket represents average over snapshots.

Persistence Length Calculations

We calculate the persistence length of HA (l_p) the following formula[80] :

$$l_p = \frac{-b}{ln < cos\theta >}$$

Here b is the average distance between the center of masses of the HA monomers. θ is the angle between the center of masses of three consecutive HA monomers. Note that l_p is not defined for HA monomers (N=1).

Hydrogen Bond and Electrostatic Energy Calculations

The number of hydrogen bonds (N_{hb}) between HA and DPPC are obtained using *gmx hbond* module. The conditions to define the hydrogen bonds are as follows: Hydrogen-Donor-Acceptor angle $\leq 30^0$ and Donor-acceptor distance $\leq$ 3.5Å. The short-range electrostatic (V_{el}) energy is calculated using *rerun* option of *gmx mdrun*. To compute V_{el} we use a cutoff distance of 12Å.[81]

3.3 Results & Discussions

3.3.1 Residence time of water and HA chains

We take into account two distinct regions of the interface. Region A, which is made up of only water molecules, extends up to 5Å above the peak of ρ_P(z), while Region B, which is made up of both water and HA chains, extends from 5Å to 15Å above the peaks. Figure 3.1 shows a schematic representation of region A and region B in a typical density profile for n_{HA5}=50. We compute the survival time of water molecules and HA monomers in these regions.

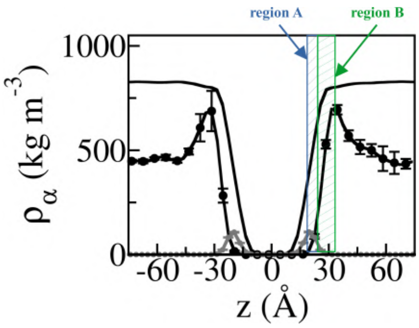

Figure 3.1: A schematic diagram of region A and region B in the density profile of n_{HA5}=50.

We use the water oxygen atom coordinates to calculate the survival probabilities of water S_W(t) in both region A and region B. For varying n_{HA5} and N, S_W(t) data in

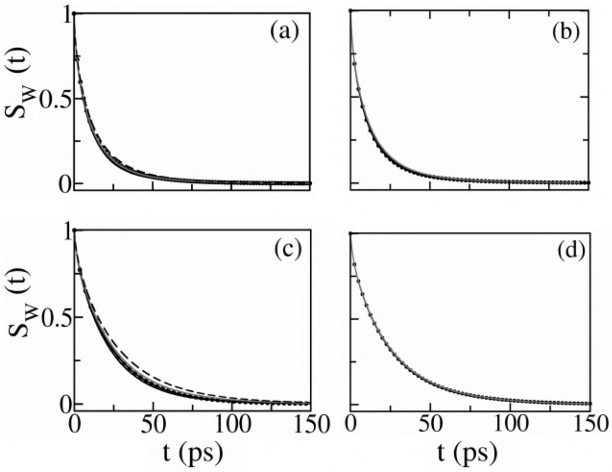

Figure 3.2: (a) Survival probability of water $S_W(t)$ in region A for different HA concentrations: n_{HA5}=0 (*solid black line*), n_{HA5}=10 (*dotted black line*), n_{HA5}=30 (*solid gray line*), n_{HA5}=50 (*dashed black line*) and (b) for varying HA chain size: N=1 (solid black line), N=1 (dotted black line), N=10 (solid gray line). (c) $S_W(t)$ in region B for different n_{HA5} and (d) for different N. The same line type as (a)-(b) is used.

region A is shown in figures 3.2(a) and 3.2(b), respectively. Figures 3.2(c) and 3.2(d) show S_W(t) in region B for different n_{HA5} and N respectively. The mean residence time of interfacial waters in both regions, τ_W^A and τ_W^B, are derived from the respective S_W(t) data (see *Methods*). The residence time of water molecules in regions A and B for the HA-free case is indicated by $\tau_W^{A,0}$ and $\tau_W^{B,0}$, respectively ($\tau_W^{A,0}$ = 10.86 ps and $\tau_W^{B,0}$ = 20.07 ps). Here $\tau_W^{A,0} < \tau_W^{B,0}$, since region B is wider than region A.

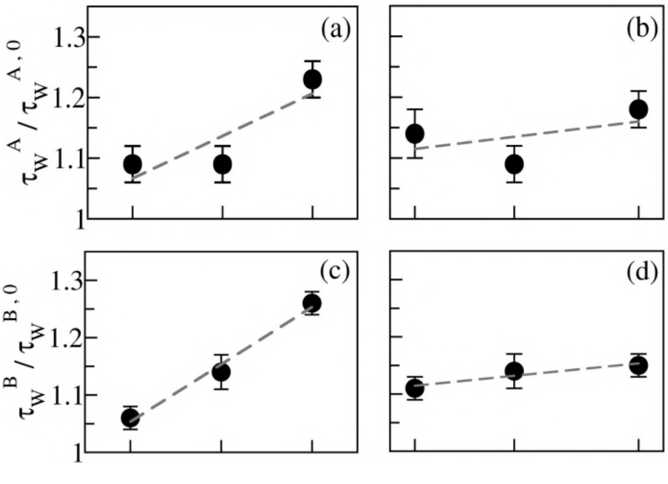

Figure 3.3: (a) The Mean residence time of water molecules in region A (τ_W^A) for varying n_{HA5} and (b) for different N. (c) Mean residence time of water molecules in region B (τ_W^B) for varying n_{HA5} and (d) for different N. The respective residence times are scaled with the quantities for HA-free cases: $\tau_W^{A,0}$ and $\tau_W^{B,0}$.

Figure 3.3(a) and 3.3(b) show $\tau_W^A/\tau_W^{A,0}$ data in region A for different n_{HA5} and N respectively. Figure 3.3(c) and 3.3(d) show $\tau_W^B/\tau_W^{B,0}$ data in region B for varying n_{HA5} and N respectively. In both regions, we find that the dynamics of water molecules get more restricted in presence of HA molecules than in the HA-free case. We also observe that both τ_W^A and τ_W^B increase with n_{HA5}, implying that the dynamics of water at the interface become slower with increasing n_{HA5}. However, both τ_W^A and τ_W^B remain almost the same with N.

It may be noted that region A is depleted from HA chains. We compute the survival probability, S_H(t) of COM of HA chains when at least one monomer of the chains remains within region B of the interface. Figure 3.4(a) and 3.4(b) show S_H(t) for different n_{HA5} and N respectively. The residence time of the HA chains, τ_H, in region B is acquired

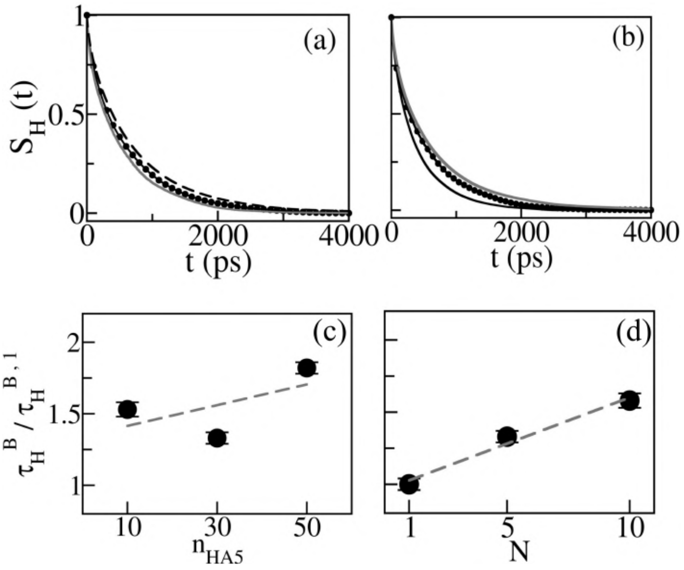

Figure 3.4: Survival probability of HA monomers $S_H(t)$ in region B for (a) n_{HA5}=10 (*dotted black line*), n_{HA5}=30 (*solid gray line*), n_{HA5}=50 (*dashed black line*), and (b) N=1 (*solid black line*), N=5 (*dotted black line*), N=10 (*solid gray line*). (c) The mean residence time of HA chains in region B (τ_H) for different n_{HA5} and (d) for different N. The data are scaled with τ_H^1, the mean residence time of HA monomers (N=1). The best linear fits are indicated by the *dashed gray* lines.

from the S_H(t) data. We find that τ_H is an order of magnitude slower than the water molecules. The finite residence time of HA chains at the interface shows that HA chains interact intermittently with the lipid bilayer, which is consistent with the earlier study.[59] Let τ_H^1 (=372 ps) be HA monomer residence time at the interface for N=1. Figure 3.4(c) and 3.4(d) show τ_H/τ_H^1 data for different n_{HA5} and N respectively. According to our data, τ_H increases linearly with n_{HA5} and N. But the change with N is less pronounced. Thus, as n_{HA5} increases, both the water and HA chains spend more time in the interface, but the residence time does not change much with N.

3.3.2 Dynamics of interfacial water molecules:

Next, we investigate the translational and rotational dynamics of water molecules at the interface of HA-water and DPPC bilayer. First, we calculate the two-dimensional translational mean squared displacements (MSD) of the interfacial waters, $\langle r_W^2 \rangle$ in the plane parallel to the bilayer in both region A and region B.[52,70] Furthermore, we calculate the rotational MSD of the interfacial water molecules, $\langle \phi_W^2 \rangle$ in both regions. To study the interfacial effect, the calculations of $\langle r_W^2 \rangle$ and $\langle \phi_W^2 \rangle$ are performed while the oxygen atoms of the waters reside continuously within a given region.[52]

Figure 3.5(a) and 3.5(b) show $\langle r_W^2 \rangle$ in region A for different n_{HA5} and N, respectively. We fit the log-log data of $\langle r_W^2 \rangle$ versus Δt up to water residence time in region A, $\tau_W^A \approx 15$

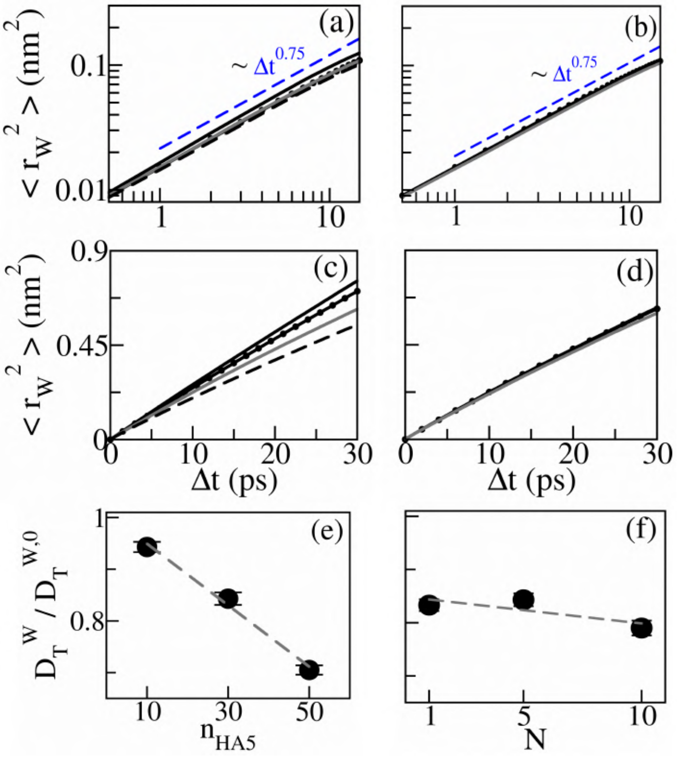

Figure 3.5: (a) Translational MSD of the water molecules ($\langle r_W^2 \rangle$) in region A, in the plane parallel to the bilayer surface, for different HA concentrations: n_{HA5}=0 (*solid black line*), 10 (*dotted black line*), 30 (*solid gray line*), 50 (*dashed black line*) and (b) for varying HA chain sizes: N=1 (*solid black line*), N=5 (*dotted black line*) and N=10 (*solid gray line*). Dashed blue lines indicate the power laws and the sub-diffusive exponents. (c) $\langle r_W^2 \rangle$) in region B for different n_{HA5} and (d) for different N. (e) Two-dimensional diffusion coefficients of the water molecules (D_T^W) in the diffusive region (region B) for different n_{HA5} and (f) N. The values are scaled by $D_T^{W,0}$, the two-dimensional diffusion coefficient of water for the HA-free case. The best linear fits are shown by the *dashed gray* lines.

ps, where we find that $\langle r_W^2 \rangle$ evolves with time with exponents β_W i.e $\langle r_W^2 \rangle \sim t^{\beta_W}$, where β_W in region A is close to 0.75 for all HA concentration and chain size ranges. This indicates the sub-diffusive motion of water molecules in region B which is consistent with the previous studies.[82] $\langle r_W^2 \rangle$ in region B for different n_{HA5} and N are shown in Figure 3.5(c) and 3.5(d) respectively. In this region, using $\langle r_W^2 \rangle$ data up to water residence time $\tau_W^B \approx 30$ ps we find that the β_W values are close to unity, suggesting diffusive dynamics. We fit $\langle r_W^2 \rangle$ data with $4D_T^W \Delta t$ to acquire the two-dimensional diffusion coefficient (D_T^W) of the interfacial waters in the plane parallel to the bilayer.[83] In the absence of HA, the diffusion coefficient of the interfacial water molecules in region B, $D^{W,0}{}_T = 6.19 \pm 0.07 \times 10^{-5}$ cm^2/s. The diffusion coefficients of the interfacial water molecules scaled to the HA free case, $D^W{}_T/D^{W,0}{}_T$ are shown in Figure 3.5(e) and 3.5(f) for different n_{HA5} and N. We note that $D^W{}_T$ for all cases are less than $D^{W,0}{}_T$, implying that HA slows down the translation of the interfacial waters at the interface. We find that $D^W{}_T/D^{W,0}{}_T$ decreases linearly with n_{HA5}. On the other hand, $D^W{}_T/D^{W,0}{}_T$ in Figure 3.5(f) shows a marginal linear decrease with N.

We calculate $\langle \phi_W^2 \rangle$ using the vector rotational displacements $\vec{\phi}_w(t)$ of the water dipole vectors ($\vec{\mu}_w$) in time t[70,75] (see details in Methods). $\langle \phi_W^2 \rangle$ of the interfacial water molecules,

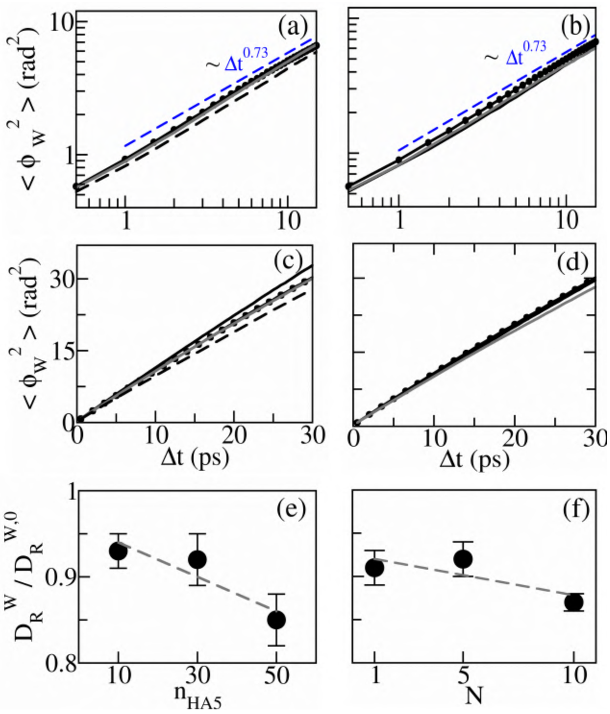

Figure 3.6: (a) Rotational MSD of the water molecules ($\langle r_W^2 \rangle$) in region A for n_{HA5}=0 (*solid black line*), 10 (*dotted black line*), 30 (*solid gray line*), 50 (*dashed black line*) and (b) for N=1 (*solid black line*), N=5 (*dotted black line*) and N=10 (*solid gray line*). Dashed blue lines show the power laws and the rotational sub-diffusive exponents. (c) $\langle \phi_W^2 \rangle$ in region B for varying n_{HA5} and (d) for different N. The same line types as (a) and (b) are used. (e) Rotational diffusion coefficients of water molecules (D_R^W) in region B for different n_{HA5} and (f) N. The values are scaled by rotational diffusion coefficient $D_W^{R,0}$ for HA free case. The *dashed gray* lines show the best linear fits.

in region A for different n_{HA5} and N are shown in Figure 3.6(a) and 3.6(b) respectively. Fitting the log-log data of $\langle \phi_W^2 \rangle$ with a power function up to $\tau_W^A \approx 15$ ps, we find that the corresponding exponent of the temporal dependence γ_W, where, $\langle \phi_W^2 \rangle \sim t^{\gamma_W}$, is close to 0.73, which suggest sub-diffusive rotational motion of water in region A.[82]

In Figures 3.6(c) and 3.6(d), we show $\langle \phi_W^2 \rangle$ for region B for varying HA concentrations and HA chain sizes. Using $\langle \phi_W^2 \rangle$ data up to $\tau_W^B \approx 30$ ps, we observe diffusive rotational motion with the exponent γ_W close to unity, as the translational counterpart. As with translational motion, the rotational diffusion coefficient is derived from the slope of the $\langle \phi_W^2 \rangle$ vs. Δt data in the linear time dependence region (region B)[70,73] We find that, for the HA free case, the rotational diffusion coefficients of the interfacial waters in region B are $D^{W,0}{}_R = 0.27 \text{rad}^2/\text{ps}$. We show $D_R^W/D_R^{W,0}$ data as functions of n_{HA5} in Figure 3.6(e) and N in Figure 3.6(f). In each instance, D_R^W is less than $D_R^{W,0}$. Additionally, D_R^W decreases linearly in both cases implying slower rotational diffusion, although the N dependence is less pronounced than the n_{HA5} dependence as noted in the translational diffusion as well.

Experimental techniques such as infrared absorption, Raman scattering, and NMR, report rotational correlation times of water, t_l^W, where $t_l^W = [l(l+1)D_R^W]^{-1}$ and l corresponding to the l'th Legendre polynomial.[77] We compute the first rank rotational correlation time t_1^W from the rotational autocorrelation function C(t) of the water molecules[52] in region B (Figure 3.7) for different HA concentrations and HA chain sizes (Table 3.1). We find that the rotational auto-correlation time for water increases in presence of HA as observed experimentally.[22,23] We note that $t_1^W \cdot D_R^W = 0.5$ that corresponds to l=1.

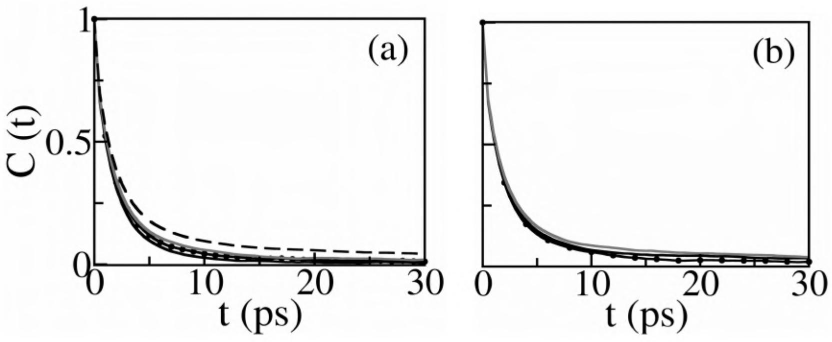

Figure 3.7: Rotational autocorrelation function of the water molecules (C(t)) in region B for different HA concentrations: n_{HA5}=0 (*solid black line*), 10 (*dotted black line*), 30 (*solid gray line*) and 50 (*dashed black line*) (b) $\langle r_W^2 \rangle$ in region B for varying HA chain sizes: N=1 (*solid black line*), N=5 (*dotted black line*) and N=10 (*solid gray line*)

system	t_1^W(ps)	$t_1^W \cdot D_R^W$
n_{HA5}=0	1.84	0.51
n_{HA5}=10	2.13	0.55
n_{HA5}= 30	2.21	0.56
n_{HA5}= 50	2.53	0.59
N=1	2.13	0.53
N=5	2.21	0.56
N=10	2.53	0.60

Table 3.1: First rank rotational autocorrelation time of water molecules, t_1^W in region B (computed from C(t) in Figure 3.7) and the product of t_1^W and rotational diffusion, D_R^W

3.3.3 Dynamics of the interfacial HA chains:

Next, we look into the dynamics of HA chains in region B of the HA-water and DPPC interface. As with S_H, for low HA chain density, we do not take region A into account here. We compute the translational MSD of the HA chains, $\langle r_H^2 \rangle$ in the plane parallel to the bilayer surface and the rotational MSD of the HA chains $\langle \phi_H^2 \rangle$ only in region B. $\langle r_H^2 \rangle$ is computed for only those chains that have at least one monomer at the interface, using the positions of those interfacial monomers until their residence time, in order to understand the interfacial dynamics. In contrast, $\langle \phi_H^2 \rangle$ is computed using the vector rotational displacement $\vec{\phi}_h(t)$ of the HA end-to-end vector in time t (see Methods for details), as long as at least one end monomer of the chain remains at the interface. For N=1, rotational MSD is calculated using the long molecular axis of the interfacial HA monomers.

We show $\langle r_H^2 \rangle$ vs Δt data for different n_{HA5} and N in Figure 3.8(a) and Figure 3.8(b) respectively. The exponents β_H of temporal dependencies of $\langle r_H^2 \rangle$ ($\langle r_H^2 \rangle \sim t^{\beta_H}$) are acquired by fitting a straight line to the log-log data of $\langle r_H^2 \rangle$ vs time Δt up to $\tau_H \approx$ 500ps. $\langle r_H^2 \rangle$ show sub-diffusive behavior at the interface, with β_H in the range of 0.80 to 0.88. Figure 3.8(c) and 3.8(d) show $\langle \phi_H^2 \rangle$ vs Δt plot for different n_{HA5} and N respectively. We observe that the exponents of temporal dependence of $\langle \phi_H^2 \rangle$ upto $\tau_H \approx$ 500ps is close to unity, suggesting that the HA rotational motion is diffusive. The rotational diffusion constants (D_R^H) are calculated from the slope of the $\langle \phi_H^2 \rangle$ vs Δt data. For HA monomers $D_R^{H,1}$ = 205.20 $\pm 1.05 \times 10^{-5}$ rad^2/ps. We show $D_R^H / D_R^{H,1}$ data in Figure 3.8(e) for different n_{HA5}. We note that D_R^H for any n_{HA5} decreases nearly 100 times in magnitude compared to $D_R^{H,1}$ and further decreases linearly with increasing n_{HA5}. HA monomers exhibit faster rotation because of their smaller size and hence higher D_R^H. Figure 3.8(f) describes $D_R^H / D_R^{H,1}$ data for varying N. D_R^H for N=5 and N=10 are two orders of magnitude less than $D_R^{H,1}$, however, our calculation suggests no significant change from N=5 to N=10.

We also compute the first rank rotational auto-correlation time (t_1^H) of the HA chains from D_R^H data for $l = 1$ (Table 3.2). We observe that t_1^H increases as n_{HA5} and N increases, but is less sensitive with N for its higher values. We find that t_1^H are of the order of

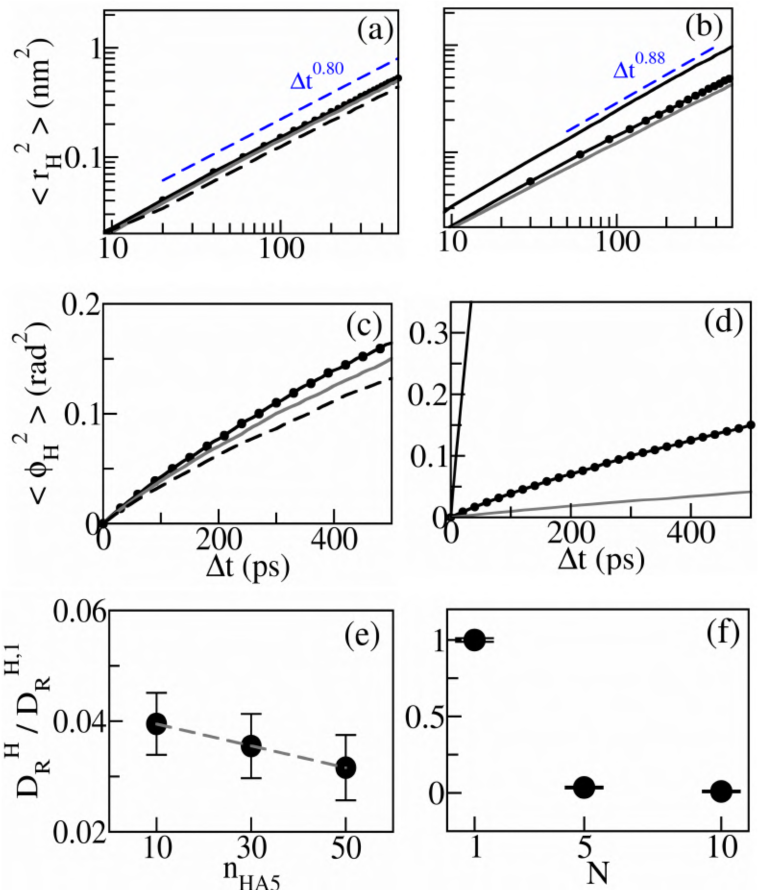

Figure 3.8: (a) Translational MSD of HA chains, $\langle r_H^2 \rangle$, in the plane parallel to the bilayer surface, for n_{HA5}=10 (*dotted black line*), n_{HA5}=30 (*solid gray line*) and n_{HA5}=50 (*broken black line*) and (b) for N=1 (*solid black line*), N=5 (*dotted black line*) and N=10 (*solid gray line*). (c) Rotational MSD of HA chains, $\langle \phi_H^2 \rangle$ for different n_{HA5} and (d) for different N. Same line types as (a) and (b) are used. (e) Rotational diffusion coefficients, $D_R^H / D_R^{H,1}$ data for different n_{HA5} and (f) for different N. The broken line shows the best-fitted straight line. Error bars are smaller than the symbol size.

nanoseconds, where t_1^W of water are in the picosecond range.

system	t_1^H (ns)
n_{HA5}=0	-
n_{HA5}=10	6.1
n_{HA5}= 30	6.8
n_{HA5}= 50	7.7
N=1	0.2
N=5	6.8
N=10	24.6

Table 3.2: First rank rotational autocorrelation time t_1^H for interfacial HA monomers

3.3.4 Dynamics of the lipid head groups

Next, we investigate the influences of HA chains on the lipid headgroup dynamics. We compute the translational MSD of the phosphorus atoms[72,84] and the rotational MSD of the PN vectors of the lipid headgroups.[74] The translational MSD $\langle r_P^2 \rangle$ is calculated in the lateral plane of the bilayer surface. On the other hand, the rotational MSD $\langle \phi_{PN}^2 \rangle$ are computed with the unbounded variable $\vec{\phi}_{pn}$ using their projection vectors on the x-y plane.[74] Figure 3.9(a) and 3.9(b) show $\langle r_P^2 \rangle$ for different HA concentrations and HA chain sizes respectively. We note an initial sub-diffusion in $\langle r_P^2 \rangle$, followed by the diffusive regime, which is also observed in the earlier studies.[72,85] The in-plane translational diffusion coefficients of the phosphorus atoms D_T^P are obtained from the slope of $\langle r_P^2 \rangle$ versus Δt data in the diffusive region. For HA free case, we find the phosphorus diffusion, $D_T^{P,0}$ = 1.33 $\times 10^{-7}$ cm^2/s. We describe $D_T^P / D_T^{P,0}$ data for different n$_{\mathrm{HA5}}$ in Figure 3.9(c). We note that the lipid phosphorus diffusion increases with n$_{\mathrm{HA5}}$ and exceeds $D_T^{P,0}$ at large n$_{\mathrm{HA5}}$. This is quite the opposite to the reduction of lipid diffusion at high sucrose and trehalose concentrations.[86–88] The higher mobility of the phosphorus atoms in presence of HA is consistent with the bilayer flexibility observed previously.[19] The N dependence of $D_T^P / D_T^{P,0}$ in Figure 3.9(d) is weaker showing a maximum around N=5.

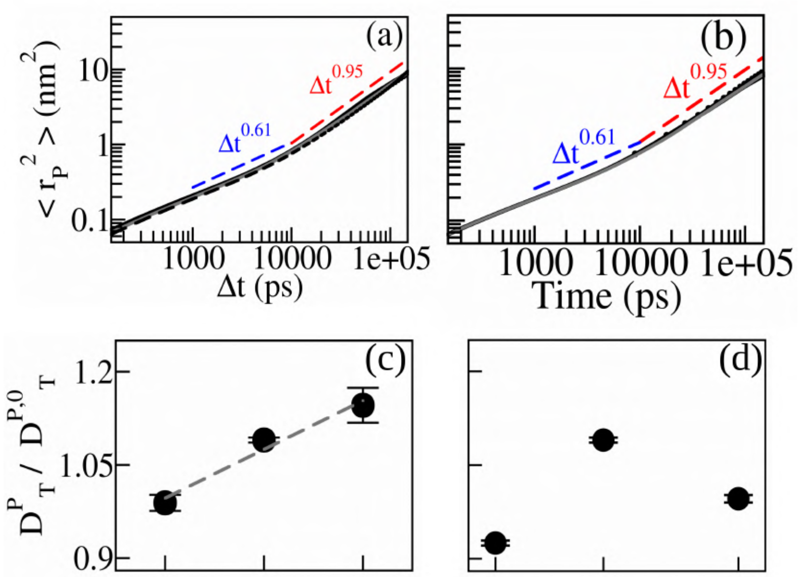

Figure 3.9: (a) Translational mean squared displacements of the Phosphorus atoms ($\langle r_P^2 \rangle$) in the lateral plane of the bilayer for varying HA concentrations: n$_{\mathrm{HA5}}$ = 0 (*solid black line*), 10 (*dotted black line*), 30 (*gray solid line*), 50 (*dashed black line*) and (b) for different HA chain sizes: N=1 (*solid black line*), N=5 (*dotted black line*) and N=10 (*solid gray line*) (c) Lateral diffusion coefficient of the phosphorus atoms of the lipid bilayer (D_T^P) for different HA concentrations and (d) for different HA chain sizes. D_T^P are scaled with the diffusion coefficients $D_T^{P,0}$ for HA free case. Best linear fits are shown by the *dashed gray* lines.

$\langle \phi_{PN}^2 \rangle$ for different n$_{\mathrm{HA5}}$ and N are shown in Figure 3.10(a) and 3.10(b) respectively.

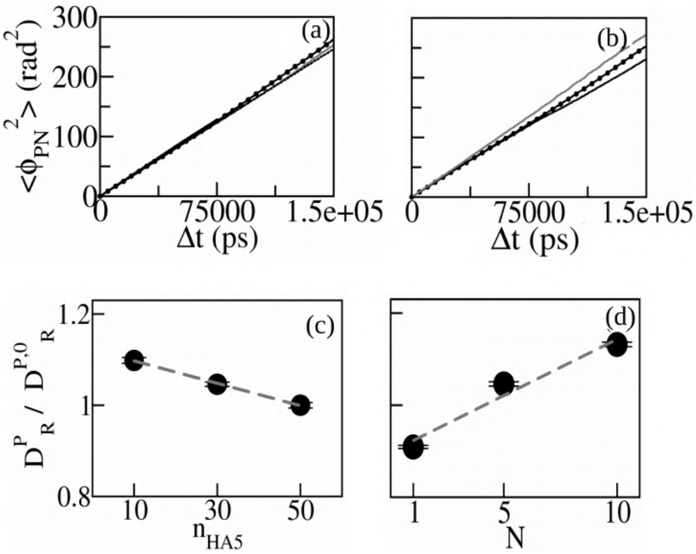

Figure 3.10: (a) Rotational mean squared displacements of the lipid PN vectors ($\langle \phi^2_{PN} \rangle$) for n_{HA5} = 0 (*solid black line*), 10 (*dotted black line*), 30 (*gray solid line*), 50 (*dashed black line*) and (b) for N=1 (*solid black line*), N=5 (*dotted black line*) and N=10 (*solid gray line*) (c)The rotational diffusion coefficients of the lipid PN vectors (D^P_R) for varying HA concentrations and (d) for different chain sizes. D^P_R are scaled with the diffusion coefficients $D^{R,0}_T$ for HA free case. Best linear fits are shown by the *dashed gray* lines.

The exponent of temporal dependence of $\langle \phi^2_{PN} \rangle$ is close to unity in all the cases so that one can extract the rotational diffusion coefficient $D^{P,0}_R$. We obtain the rotational diffusion coefficient of the DPPC bilayer for HA free case, $D^{P,0}_R$ is 0.82 rad^2/ns. Figure 3.10(c) shows that $D^{P,0}_R/D^{P,0}_R$ decreases with n_{HA5}. The reduced rotational diffusion of the PN vector may indicate the increased electrostatic interactions between HA and DPPC.[89] However, unlike the other quantities, $D^P_R/D^{P,0}_R$ in Figure 3.10(d) increases linearly with N.

3.3.5 Discussions

I. Water dynamics. -

We show that as the concentration of HA monomer increases, both the translation and rotation of the interfacial water molecules becomes sluggish. This observation is in general agreement with the water dynamics in the vicinity of HA and other hydrophilic molecules like dextran.[22,23] Crucially, the N dependence of the interfacial dynamics is weak in comparison to n_{HA5}. N only slightly alters the translational and rotational diffusion of water. In order to determine the origin of the distinct concentration and chain size dependence of the water dynamics, we consider the organization of the HA chains via the cross-chain radial distribution[79] of the HA monomers, $g_{xy}(r)$, where r is the distance in the plane parallel to the bilayer between the COM of two HA monomers belonging to two distinct chains. The $g^{xy}(r)$ vs. r plot for various n_{HA5} is shown in Figure 3.11(a). The value of n_{HA5} increases the cross-chain correlation. For varying

N, the $g^{xy}(r)$ vs. r plot is displayed in Figure 3.11(b). For N=1, we observe a clear peak in the $g^{xy}(r)$ profile. The peak vanishes as N increases, suggesting that inter-chain correlations fall with increasing N.

Additionally, we calculate the ratio of persistence length (l_P) of the HA chains[80] to their end-to-end distances (R_e). Higher l_P indicates a more rigid polymer chain, as l_P characterizes the length scale of correlation between the monomers.[90] The magnitude of the vector joining the COM of the terminal monomers determines R_e. In Figure 3.11(c) and Figure 3.11(d), we show the distribution of l_P/R_e, $H(l_P/R_e)$ for various n_{HA5} and N, respectively. For each n_{HA5}, the peak position of the distribution remains constant. This suggests that the flexibility of the HA chains is nearly constant for all HA concentrations. On the other hand, it shifts to a smaller value of l_P/R_e as we increase N. Thus, as HA

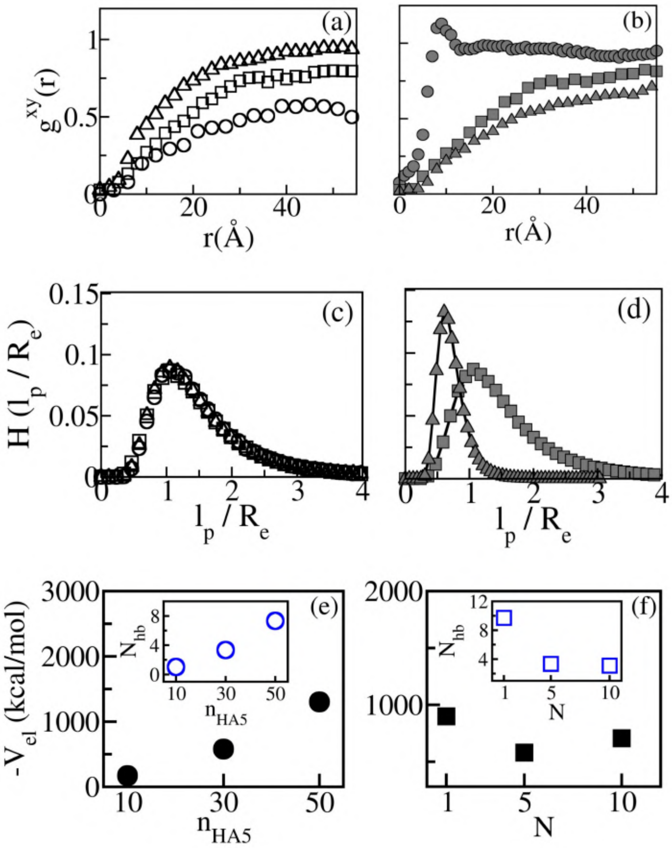

Figure 3.11: (a) Cross-chain radial distribution of HA monomers at the interface $g_{xy}(r)$, in the plane parallel to the bilayer surface, for n_{HA5}=10 (*circles*), n_{HA5}=30 (*squares*), and n_{HA5}=50 (*diamonds*) (open symbols) and (b) for N=1 (*circles*), N=5 (*squares*) and N=10 (*diamonds*) (closed symbols). (c) Histogram of persistence length (l_P) to end-to-end distance (R_e) ratio of the HA chains for different n_{HA5} and (d) for different N. The same symbols as (a) and (b) are used. (e) Electrostatic interaction energy -V_{el} between HA and DPPC for varying n_{HA5}, inset: N_{hb} vs n_{HA5}. (f) -V_{el} for different N. inset: N_{hb} for varying N.

chain size increases, the flexibility of HA molecules increases.[90] As a result, the interchain correlations become weaker because of the increased chain flexibility in Figure 3.11(b). The weak interchain correlation indicates increased space for the water molecules to move at the interface. In polymer gels, the diffusivity of water molecules,[91] polystyrene tracer beads[92] etc. increases with a decrease in network pore size relative to the particle size. Hence, for varying HA chain sizes, the interfacial water molecules experience competition between the hydrophilic interaction with HA and HA chain flexibility. This leads to the dynamics with marginal N dependence. The weak N dependence of the interfacial water dynamics is quite similar to the polyacrylamide solutions, where water orientational relaxation is found to be chain length independent.[93] As polyacrylamide is a hydrophilic molecule and forms hydrogels similar to HA, the marginal N-dependent dynamical characteristics might be typical of hydrophilic molecules.

II. HA chain dynamics. -

HA chains show subdiffusive translation at the interface. Similar subdiffusion is also reported for polyanionic DNA chains adsorbed to lipid bilayer at a short timescale.[94,95] On the other hand, the HA rotational dynamics are diffusive. Since HA chain flexibility remains the same but the chains form a compact network as n_{HA5} increases the rotational diffusion becomes slower with monomer concentration due to less availability of space for movement. We also note that because of the smaller size, the rotational diffusion of HA monomers (N=1) is faster than N=5 and N=10 but it is weakly dependent on N for larger N. HA decamers are more flexible than pentamers. However, decamers spend more time at the interface than pentamers as suggested from the residence time data due to their bulkier size. Competition between these two factors results in the observed weak dependence of HA rotational diffusion on N.

III. Lipid dynamics. -

We note that the lipid headgroups do not show direct coupling with HA. However, the dynamics of the lipid head groups are observed to be sensitive to n_{HA5} and N. To explain the lipid dynamics we compute hydrogen bonds N_{hb} and electrostatic interaction energy V_{el} between HA and DPPC. N_{hb} for varying n_{HA5} is shown in the inset of Figure 3.11(e). The small number of hydrogen bonds is consistent with the water-mediated and intermittent HA-DPPC interactions.[19,59] We find that N_{hb} increases with n_{HA5}. Because HA chains are negatively charged, one expects a significant contribution of V_{el} in HA-DPPC bilayer interaction. Figure 3.11(e) shows -V_{el} between HA and lipids for different n_{HA5}. We observe that V_{el} increases monotonically with n_{HA5}.

Since the number of monomers and hence, the electrostatic charge remain the same for different N, the N dependencies of N_{hb} and -V_{el} are different. N_{hb} for different N is shown in the inset of Figure 3.11(f). N_{hb} decreases for N initially, then does not change much from N=5 to N=10. Figure 3.11(f) shows -V_{el} between HA and lipids for varying N. We find that the V_{el} decreases from N=1 to N=5 when pentamers behave like rigid rods as $l_p/R_e \sim 1$. This is also reflected in the reduction of N_{hb} compared to the N=1 case. For N=10 the HA chains are more flexible ($l_p/R_e < 1$) when we find only a slight increase in -V_{el} and almost no change in N_{hb}. Thus overall the bilayer-HA interaction gets reduced with N for a given number of monomers.

The enhancement of registry between lipid molecules and enhanced area fluctuations reported earlier[19] is consistent with enhanced HA-DPPC interaction with n_{HA5}. The increased bilayer area fluctuation results in enhanced lipid diffusion in the bilayer plane. The higher electrostatic interaction also makes the PN dipoles more ordered, and undergo slower rotational diffusion. As N increases the bilayer-HA interaction is reduced but the time spent by HA in the vicinity of the bilayer increases. These two effects compete to have a maximum of D_T^P at N=5. The reduction in interaction aids in faster dipole rotation.

Atomistic simulations reported here are limited to small HA chains due to computational cost. However, the results match well with experiments involving high molecular weight HA chains[59,96] and are comparable to polyacrylamide hydrogel systems.[93] HA has a wide range of applications such as drug delivery systems like HA-coated liposomes, where HA improves the stability and bioavailability of therapeutic agents.[97–99] The dynamics of HA in the vicinity of cell walls are important for the controlled release of the drugs.[100] Similarly, HA hydrogels are popularly used in the cosmetic industry for their excellent moisturizing and anti-aging properties.[101] The water dynamics within these hydrogels are critical for their effectiveness in cosmetic applications, helping to maintain skin hydration. Our findings suggest that interfacial diffusion is more sensitive to HA concentration than to the HA chain size, which may aid potential improvements in these applications. Furthermore, the results from our atomistic simulations can serve as a benchmark for coarse-grained models,[102,103] which are used to simulate longer HA chains more efficiently.

3.4 Conclusions

To summarize, we study the dynamics of water, short HA chains, and lipids at the interface of HA-water and DPPC bilayer. We observe that the increasing monomer concentration slows down the interfacial dynamics, but the chain size dependence is only marginal. We explain this behavior in terms of the HA network structure and its flexibility at the interface which we expect to hold for all hydrophilic chains. The dynamics we report here are amenable to various spectroscopic experiments, typically in the terahertz (THz) range.

Chapter

4

Dynamic heterogeneity of water at the HA-water and DPPC interface

4.1 Introduction

Organic and inorganic interfaces exhibit chemical and topological heterogeneity, leading to variations in mean residence times and orientational motion of the interfacial molecules.[104,105] These variations result in multiple relaxation timescales in the dynamics, termed 'Dynamic heterogeneity'. Dynamic heterogeneity is commonly associated with glass-like systems where the relaxation timescale of the system exceeds the observation timescale. Nevertheless, water molecules near surfaces, for example the bridging water molecules in protein-DNA complex,[106] the hydration shells of IDPs,[105] inorganic surfaces[24] and lipid bilayer,[107] inside confined geometries[25,108] show slow and heterogeneous dynamics. Previous study shows that dynamic heterogeneity influences diffusion and local viscosity near nano- and bio-surfaces.[24]

Dynamic heterogeneity can be inferred from the self van-Hove correlation function (self vHf), $G(\xi, \Delta t)$, defined by the distribution of displacement of the particles ξ in translation[25] or in rotation[75,76] in the time interval Δt. Mathematically, $G(\xi, \Delta t) = \langle \frac{1}{N} \sum_{i=1}^{N} \delta[\xi - |\vec{\xi}_i(\Delta t) - \vec{\xi}_i(0)|] \rangle$, where N is the total number of tagged particles. For a normal fluid, the self vHf is a Gaussian where width changes linearly with time, the slope being related to the diffusion coefficient D_ξ of ξ.[109,110] In case of heterogeneous dynamics, $G(\xi, \Delta t)$ is marked by deviation from Gaussian. The deviation is characterized by the presence of a distinct tail after the central Gaussian. The tail can be either another Gaussian or an exponential function of ξ.[110] Non-Gaussian self vHf is interpreted by the presence of a distribution $P(D_\xi)$ of diffusion coefficients D_ξ. This is particularly so if the system is observed in a window much shorter than the timescale the system needs to explore the entire phase space.[110] The relationship between non-Gaussian $G(\xi, \Delta t)$ and its underlying distribution of diffusion coefficients $P(D_\xi)$ is modelled via $G(\xi, \Delta t)$=

$\int dD_\xi \ p(D_\xi)g(\xi|D_\xi,t)$ where $g(\xi|D_\xi,t) = \frac{1}{\sqrt{4\pi D_\xi t}}e^{\frac{-\xi^2}{4D_\xi t}}$.[26] In the case of homogeneous dynamics, $P(D_\xi)$ has a very sharp peak at a particular value of D$_\xi$. In case of dynamic heterogeneity, multiple close diffusion coefficients are present in the system, which leads to a largely spread $P(D_\xi)$ and a non-gaussian $G(\xi,\Delta t)$.[26,110] A bimodal distribution $P(D_\xi)$ (i.e. two diffusion coefficients in the system) can result in the Gaussian tail of $G(\xi, \Delta t)$, whereas the exponential tail of $G(\xi, \Delta t)$ comes from the convolution of many single particle Gaussians i.e. multimodal $P(D_\xi)$.[26,109,111] Thus, even with the non-Gaussian $G(\xi, \Delta t)$, the nature of the particle displacement remains diffusive.[110,112] In this case, the diffusion coefficient D$_\xi$ obtained from the (linear) MSD plot is the same as the first moment of the distribution of diffusivity $P(D_\xi)$. In literature, this situation is known as 'Fickian yet Non-Gaussian' dynamics.[112]

In previous chapters, we examine the elastic response of the DPPC lipid bilayer to HA chains and the dynamics of interfacial molecules at the HA-water and DPPC bilayer interfaces. Moreover, the observation time window is limited by the survival time. This leads us to investigate the impact of HA molecules on the dynamic heterogeneity of interfacial water molecules, an aspect which is largely unexplored in theoretical studies. In this chapter, we investigate the dynamic nature of the water molecules in the interface of HA-water and DPPC bilayer by obtaining the translational self van Hove function (tvHf, $G_T(r, \Delta t)$) and rotational self van Hove function (rvHf, $G_R(\phi, \Delta t)$). Here r indicates the translational displacement of water molecules in two dimensions in the parallel plane of the bilayer in time Δt, and ϕ is the rotational displacement in time Δt.[70] We also obtain the underlying distribution of translational and rotational diffusivity. We find non-Gaussian tvHf and rvHf suggesting dynamic heterogeneity in the translation and rotation respectively of the interfacial water molecules. In the subdiffusive region, the tvHf and rvHf show exponential tails, whereas in the diffusive region, tvHf and rvHf show Gaussian tails. Additionally, we observe peaks in the distribution of diffusivities at a very small value of diffusion coefficients in the subdiffusive region. On the contrary, in the diffusive region, the distribution is either broad (for translation) or peaked at multiple diffusion coefficient values (for rotation). This study could be important for a microscopic understanding of the viscoelastic and elastic response of the HA-coated cellular surfaces[20,76]

4.2 Methods

4.2.1 Force field details and MD simulation

We take the same MD trajectory used for investigating the interfacial dynamics in *chapter 3*. See section 3.2.1 and 2.2.1 for details of the simulation methods.

4.2.2 Analysis

Translational and Rotational van hove function calculation

The self part of the translational van Hove function, $G_T(r, \Delta t)$ is given by the following formula:[25]

$$G_T(r, \Delta t) = \langle \frac{1}{N_\alpha} \sum_{i=1}^{N_\alpha} \delta[r - |\vec{r}_i(\Delta t) - \vec{r}_i(0)|] \rangle. \tag{4.1}$$

Here N_α indicates the number of α species that remain at the interface throughout the time interval of Δt. Here r is calculated in two dimensions.

The rotational self van-Hove function is defined[73,76] as

$$G_R(\phi, \Delta t) =< \frac{1}{N_\alpha} \sum_{i=1}^{N_\alpha} \delta[\phi - |\vec{\phi}_i(t) - \vec{\phi}_i(0)|] >$$

Here $\vec{\phi}_i(t)$ is the displacement of i'th molecule in rotational space where $\vec{\phi}(t) = \int_{t_0}^{t} \delta\vec{\phi}_i(t')$. Here $\delta\vec{\phi}_i$ is constructed using the dipole moment $\vec{\mu}_i$ in such a way that its magnitude is given by $cos^{-1}[\hat{u}_i(t) \cdot \hat{u}_i(t + \delta t)]$ and its direction is given by $[\hat{u}_i(t) \times \hat{u}_i(t + \delta t)]$.[25,73] Note that $\vec{\mu}_i$ is defined as the straight line joining the oxygen atom and the center of mass of two hydrogens of the water molecules. We take Δt = 0.5 ps. Note that, $\Delta\phi$ is an unbounded variable and its distribution converges to a Gaussian form at long times.[76,77] Both $G_T(r, \Delta t)$ and $G_R(\phi, \Delta t)$ are acquired using unfolded trajectory.

Functional dependence of $G_T(r, \Delta t)$ on r and $G_R(\phi, \Delta t)$ on ϕ

To infer the presence of any Gaussian or exponential tail in addition to the central Gaussian of $G_T(r, \Delta t)$ and $G_R(\phi, \Delta t)$ after a certain crossover length (r_c) or angle (ϕ_c) we follow method based on.[25,113,114] We consider $lnG_T \sim r^2/\sigma^2$ for $r < r_c$, which corresponds to the central Gaussian part, and $lnG_T \sim r^2/\sigma^2$ or $lnG_T \sim r/\lambda$ for $r > r_c$, which account for a Gaussian or exponential tail respectively. The r_c and nature of the tail, which yields minimum χ^2 are taken to be best fits. The same procedure is followed to extract the tail nature of $G_R(\phi, \Delta t)$ as well. The exponent of the time dependence of r_c, ϕ_c, σ^2, and λ is obtained by averaging and estimating the error bars over three equilibrium trajectories. The error bars are computed by dividing the standard deviation of the quantity by the square root of the number of samples.

Distribution of diffusivity using Lucy's deconvolution method

We compute the distribution of translational diffusivity $P(D_T)$ from $G(r, \Delta t)$ following the prescription defined in Ref.[115] The relation between $P(D_T)$ and $G(r, \Delta t)$ is given by[26]

$$G(r, \Delta t) = \int dD_T \, P(D_T, \Delta t) \, g(r|D_T, \Delta t) \tag{4.2}$$

where $g(r|D_T, \Delta t) = \frac{1}{4\pi D_T \Delta t} \exp\left(-\frac{r^2}{4D_T \Delta t}\right)$. Now, as we have $G(r, \Delta t)$, we follow the Lucy's iterative scheme to compute $P(D_T)$ using the formula:[26,115]

$$P^{n+1}(D_T, \Delta t) = P^n(D_T) \int \frac{G(r, \Delta t)}{G^n(r, \Delta t)} g(r|D_T) dr \tag{4.3}$$

Here $P^n(D_T)$ is the distribution of diffusivity obtained at the n'th iteration. We start with the initial distribution $P^0(D_T) = 1/D_{av} \exp^{-D_T/D_{av}}$. The svhf at the n'th iteration is given by $G^n(r, \Delta t) = \int P^n(D_T, \Delta t) g(r|D_T, \Delta t) dD_T$ following equation 4.2. The same method is used to compute the distribution of rotational diffusivity $P(D_R)$ as well. For rotation in three dimension, we consider $g(\phi|D_R, t) = \frac{1}{(4\pi D_R \Delta t)^{\frac{3}{2}}} \exp\left(-\frac{\phi^2}{4D_R \Delta t}\right)$.

4.3 Results

We compute the translational self vHf (tvHf), $G_T(r, \Delta t)$ and rotational self vHf (rvHf), $G_R(\phi, \Delta t)$ for water molecules at the interface of HA-water and DPPC bilayer. In the previous chapter, we show that the water molecules within the 5Å of d_P (the peak of phosphorus density profile $\rho_P(z)$) exhibit subdiffusive translation and rotation, where water molecules experience a strong interaction with the lipid bilayer. The mean residence time of water at this region $\tau_w^A \approx$ 10ps.[27] Water molecules from d_P + 5Å to d_P + 15Å show diffusive behavior, where the mean residence time of water molecules is $\tau_w^B \approx$ 20ps. We compute G_T(r,Δt) and $G_R(\phi, \Delta t)$ in both of these regions for $\Delta t \lesssim \tau_w^A$ and $\Delta t \lesssim \tau_w^B$ respectively.

The distribution of translational and rotational diffusivity ($P(D_T)$ and $P(D_R)$) is calculated using Lucy's deconvolution scheme described in section 4.2.2. We calculate the distribution of diffusivity at an intermediate time limit where time $\Delta t \approx \tau_w^A/2$ and in the large time limit where $\Delta t \approx \tau_w^A$ (for region A). We perform the same calculation for region B as well. The average diffusion coefficient $\langle D_T \rangle$ or $\langle D_R \rangle$ are calculated from the distribution in the large time limit.

4.3.1 Self van Hove functions of water molecules near lipid bilayer without HA

First, we study $G_T(r, \Delta t)$ and $G_R(\phi, \Delta t)$ of water molecules near the bilayer for HA-free case (n_{HA5}=0).

(a) tvHf $G_T(r, \Delta t)$:
We show $lnG_T(r, \Delta t)$ vs Δt data for the interfacial waters in the subdiffusive region near the bilayer in figure 4.1(a) and 4.1(b) for Δt=5ps and Δt=10ps respectively. $G_T(r, \Delta t)$ shows a central Gaussian followed by an exponential tail in both cases. The time variation of the crossover length in the subdiffusive region r_c is shown in Figure 4.1(c). We find that r_c increases with time as $r_c \sim \Delta t^{0.31\pm0.02}$. As the exponent is less than 1, heterogeneity persists up to the residence time. We also characterize the time variation of the width σ^2 and decay constant λ and describe it in Figure 4.1(d) and 4.1(e) respectively. We find that the $\sigma^2 \sim \Delta t^{0.69\pm0.002}$ and $\lambda \sim \Delta t^{0.42\pm0.01}$

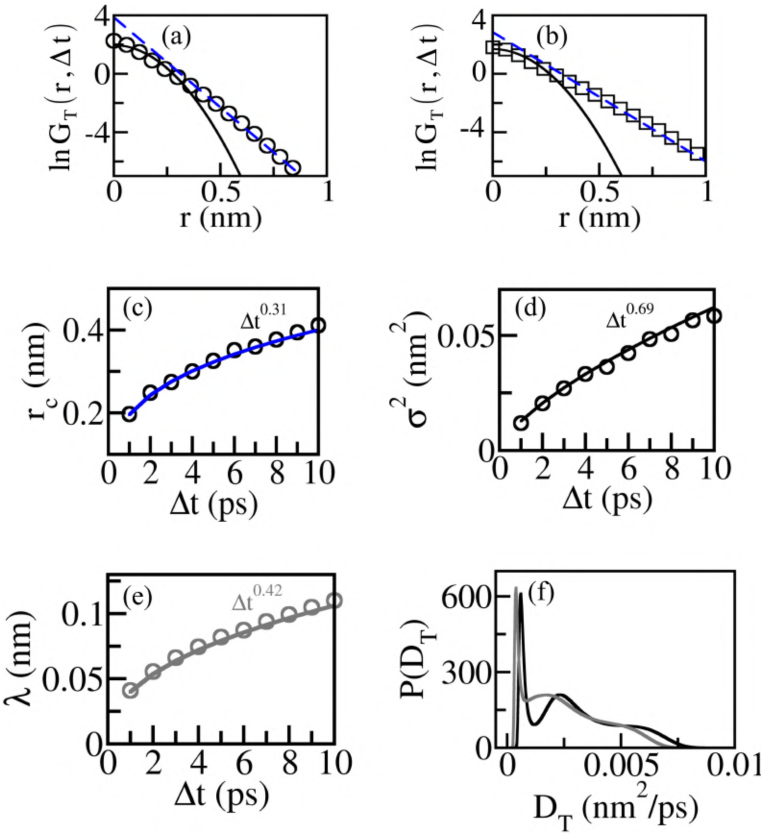

Figure 4.1: ln$G_T(r, \Delta t)$ vs Δt plot for n_{HA5} = 0 for (a) Δt=5ps and (b) for Δt=10ps in the subdiffusive interface. *Solid* lines show the central Gaussian of G_T where *broken* lines imply the exponential tails. (c) r_c vs time Δt (d) Time variation of σ^2 and (e) λ. The solid curves represent the fitted data. (e) The distribution of translational diffusivities $P(D_T)$ at Δt=5ps (black line) and Δt=10ps (gray line).

We also compute the underlying distribution of diffusivity $P(D_T)$ for the subdiffusive region. $P(D_T)$ for the subdiffusive waters at Δt=5ps and Δt=10ps are shown in Figure 4.1(f). A sharp peak is observed in $P(D_T)$ at a very small D_T value with a distribution spanned over a broad range of D_T. The sharp peak at a very small D_T value corresponds to dynamically arrested water molecules near the bilayer. Hence the subdiffusive translational MSD of the interfacial waters, as observed in *chapter 3*, results from the sluggish movement of the interfacial waters with very small diffusion coefficients and large width in the distribution of diffusivity. The peak of $P(D_T)$ is at $4.5 \times 10^{-6}\ cm^2/s$ and the width of the distribution is $\approx 7 \times 10^{-5}\ cm^2/s$. We also note that there is not much change in $P(D_T)$ as time evolves. This is consistent with the observation that the dynamic heterogeneity persists up to the residence time.

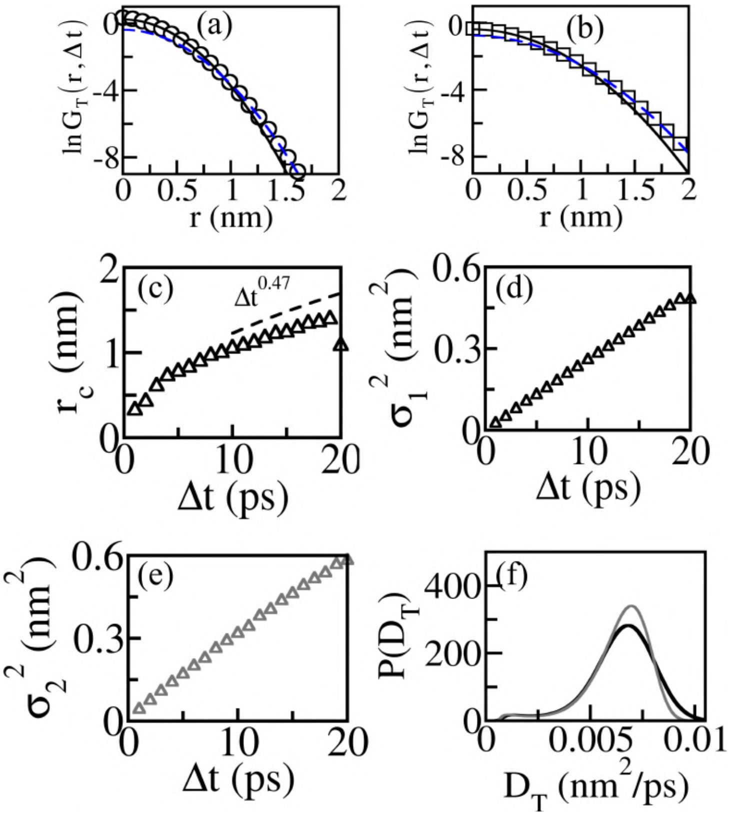

Figure 4.2: ln$G_T(r, \Delta t)$ vs Δt plot for n_{HA5} = 0 for (a) Δt=10ps and (b) for Δt=20ps in the diffusive interface. *Solid* lines show the central Gaussian of G_T where *broken* lines imply the Gaussian tails. (c) r_c vs time Δt. Time variation of σ_1^2 (d) and σ_2^2(e). (f) The distribution of translational diffusivities $P(D_T)$ at Δt=10ps (black line) and Δt=20ps (gray line).

Next, we calculate $G_T(r, \Delta t)$ of the water molecules at the diffusive region of the DPPC-water interface. $G_T(r, \Delta t)$ are shown in Figure 4.2(a) and 4.2(b) for Δt=10ps and 20ps respectively. G_T exhibits a central Gaussian with width σ_1^2 with a Gaussian tail with width σ_2^2. Hence, there are two diffusion coefficients of the water molecules. The time variation of the crossover length r_c is shown in Figure 4.2(c). r_c varies with time as $\sim \Delta t^{0.47 \pm 0.03}$, indicating that heterogeneity persists up to the residence time of the interfacial water in the diffusive region. σ_1^2 and σ_2^2 are shown in Figure 4.2(d). Both σ_1^2 and σ_2^2 grow linearly with time, consistent with the diffusive dynamics. We compute $D_T^1 = 6.00 \pm 0.30 \times 10^{-5}\ cm^2/s$ and $D_T^2 = 7.60 \pm 0.30 \times 10^{-5}\ cm^2/s$ from the slope of σ_1^2 and σ_2^2 vs Δt data respectively. The slower diffusion coefficient D_T^1 is the contribution from water molecules at the inner part of the diffusive region i.e. closer to the bilayer. Nevertheless, we note that D_T^1 and D_T^2 values are close to each other.

We compute the distribution of diffusion constants $P(D_T)$ from G_T. Figure 4.2(f) show the $P(D_T)$ for Δt=10ps (*black*) and 20ps (*gray*). $P(D_T)$ covers a broad range here, which indicates dynamic heterogeneity. We note that the two diffusion coefficients obtained from the time variation of the width of tvHf are not resolved in the $P(D_T)$ profile, as they are very close. With time $P(D_T)$ remains almost the same, consistent with the dynamic heterogeneity persisting till the residence time. We compute the average diffusion constant of water molecules in the lateral plane of the bilayer $\langle D^T \rangle$ from $P(D_T)$ of larger time i.e Δt=20ps. $\langle D^T \rangle = 6.50 \pm 0.07 \times 10^{-5}\ cm^2/s$ which is close to the mean value of D_1^T and D_2^T. $\langle D^T \rangle$ is also comparable to $D_T^{W,0} = 6.19 \pm 0.07 \times 10^{-5}\ cm^2/s$ obtained from MSD data in *chapter 3* (see section 3.3.2).

(b) rvHf $G_R(\phi, \Delta t)$:

Now, we compute $G_R(\phi, \Delta t)$ for water molecules in the subdiffusive region. In figure 4.3(a) and 4.3(b) we show the $G_R(\phi, \Delta t)$ data for Δt=5 ps and Δt=10 ps respectively. We find that rvHf shows exponential tails for both times. We find that the crossover angle ϕ_c remains unchanged with time as shown in 4.3(c). We also note that σ^2 of the central Gaussian vary with time as $\sim \Delta t^{0.27 \pm 0.01}$ whereas the decay exponent of the exponential tail $\lambda \sim \Delta t^{0.30 \pm 0.03}$ (4.3(d)). Figure 4.3(e) and 4.3(f) show the underlying distribution of diffusion constants $P(D_R)$ at Δt=5 ps and Δt=10 ps respectively. $P(D_R)$ exhibits multiple peaks in both cases. The peaks are observed at very small D_R values as well as higher D_R values. The peaks at extremely slow D_R correspond to the rotationally slow water molecules that are stuck to the bilayer. The subdiffusive rotational MSD (see section 3.3.2) may result from these rotationally sluggish water molecules with very small D_R. $P(D_R)$ at Δt=10ps are sharper than Δt=5ps indicating decreasing heterogeneity with increasing observation time.

Next, we investigate the characteristics of rvHf in the diffusive interface of HA-water and DPPC bilayer. We show $G_R(\phi, \Delta t)$ for water molecules in the diffusive interface for Δt=10 ps and Δt=20 ps in Figure 4.4(a) and 4.4(b) respectively. $G_R(\phi, \Delta t)$ shows an exponential tail at Δt=10ps whereas a Gaussian tail is observed at Δt=20ps. We characterize the time dependence of the width σ^2 of the central Gaussian and the λ of the exponential tail in Figure 4.4(c) upto $\Delta t = 10$ps. The width σ^2 of the central Gaussian

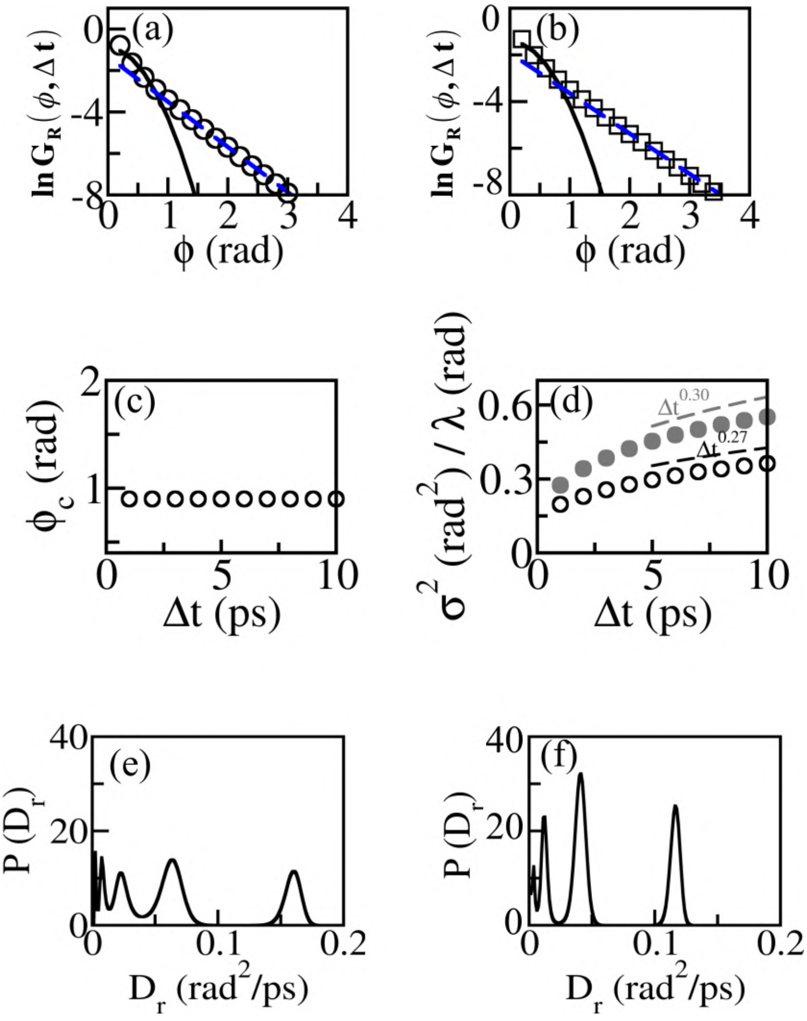

Figure 4.3: ln$G_R(\phi, \Delta t)$ vs Δt plot for n_{HA5} = 0 for (a) Δt=5ps and (b) for Δt=10ps in the subdiffusive interface. *Solid* lines show the central Gaussian of G_T where *broken* lines imply the exponential tails. (c) ϕ_c vs time Δt (d) Time variation of σ^2 (*black* circles) and λ (*gray* circles). (e) The distribution of rotational diffusivities $P(D_R)$ at Δt=5ps and (f)Δt=10ps.

varies almost linearly with time, whereas the decay constant λ of the exponential tail varies as $\sim t^{0.50\pm0.02}$. After 10ps, $G_R(\phi, \Delta t)$ takes a double Gaussian form where σ_1^2 and σ_2^2 of the central and tail Gaussians grow almost linearly with time as shown in Figure 4.4(d). Evolving from an exponential tail at a short time to a Gaussian tail at a larger time infers that the dynamical heterogeneity of the interfacial water rotation decreases as Δt increases. Here also the crossover angle ϕ_c does not change with Δt.

We also obtain the distribution of rotational diffusion $P(D_R)$ from $G_R(\phi, \Delta t)$. Figure 4.5(a) and 4.5(b) show $P(D_R)$ at Δt=10ps and 20ps respectively. We observe a principal peak with small secondary peaks in the $P(D_R)$ profile. The peaks of $P(D_R)$ are present at both Δt and their heights increase as time evolves. Hence, the dynamic heterogeneity persists up to residence time and decreases as Δt increases. The average rotational

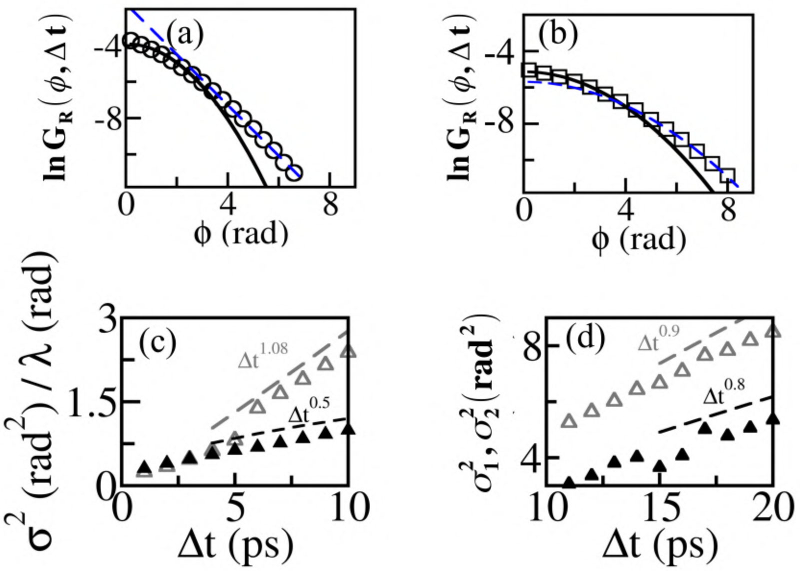

Figure 4.4: (a) ln$G_R(\phi, \Delta t)$ vs Δt plot for n_{HA5} = 0 for Δt=10ps and (b) for Δt=20ps in the diffusive interface. *Solid* lines show the central Gaussian of G_T where *broken* lines imply the exponential/Gaussian tails. (c) Time variation of σ^2 (*gray* triangles) and λ (*black* triangles) up to Δt=10ps. (d) Time variation of σ_1^2 (*gray* triangles) and σ_2^2 (*black* triangles) from Δt=10ps to Δt=20ps.

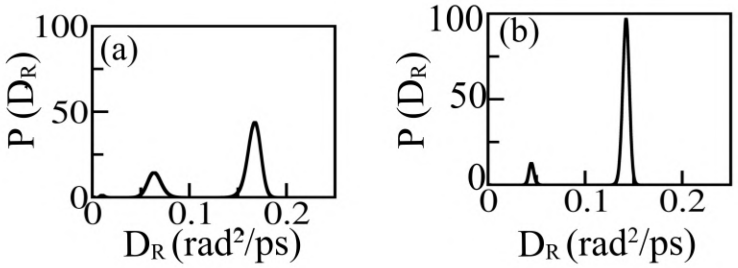

Figure 4.5: (a) The distribution of rotational diffusivities $P(D_R)$ at Δt=10ps and (b) Δt=20ps.

diffusion coefficient of water molecules $\langle D_R \rangle$ at the diffusive interface is computed from $P(D_R)$ is $\langle D_R \rangle$ = 0.13 ± 0.02 rad^2/ps. On the other hand, two diffusion coeffecients D_R^1 and D_R^2 are obtained from the linear σ_1^2 and σ_2^2 vs Δt data from 10ps to 20ps: D_R^1 = 0.10 ± 0.01 rad^2/ps, D_R^2= 0.16 ± 0.02 rad^2/ps. Thus $\langle D_R \rangle \approx \frac{1}{2}[D_R^1 + D_R^2]$. $\langle D_R \rangle$ is also comparable to $D_R^{W,0} = 0.27\ rad^2/ps$ obtained from the rotational MSD data in *chapter 3* (see section 3.3.2)

4.3.2 Self van Hove function of waters at the interface of HA-water and DPPC bilayer for varying HA concentrations

In this section, we describe how translational and rotational dynamic heterogeneity responds to varying HA concentrations.

(a) tvHf $G_T(r, \Delta t)$.-
First, we show ln$G_s(r, \Delta t)$ vs r plot in the subdiffusive interface for n_{HA5}=10, 30 and 50 in Figure 4.6(a), 4.6(b) and 4.6(c) respectively (left panel,L: Δt=5ps, right panel,R: Δt=10ps). For both the observation times, G_T data exhibit central Gaussians with exponential tails

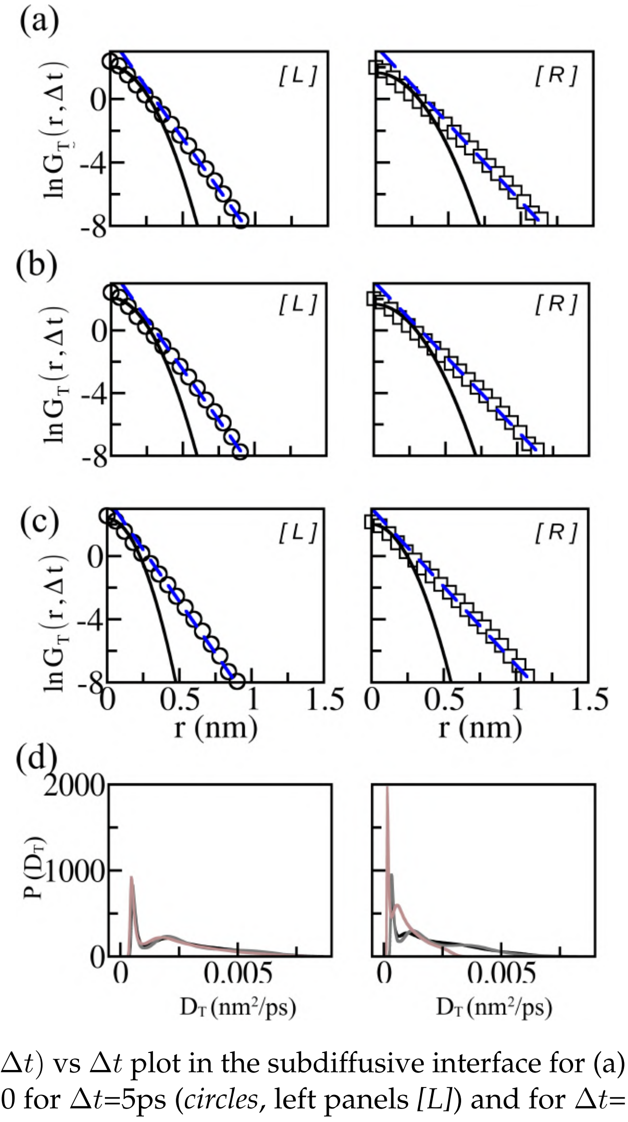

Figure 4.6: ln$G_T(r, \Delta t)$ vs Δt plot in the subdiffusive interface for (a) n_{HA5}=10 (b)n_{HA5} = 30 and (c) n_{HA5} = 50 for Δt=5ps (*circles*, left panels *[L]*) and for Δt=10ps (*squares*, right panels *[R]*). *Solid* and *broken* lines indicate the best-fitted central Gaussian part and the exponential tail respectively. (d) Distribution of diffusivity $P(D_T)$ for n_{HA5}=10(*black*), 30 (*gray*) and 50 (*brown*) for Δt=5ps(left panel *[L]*) and 10ps (right panel *[R]*).

in each case. The crossover length r_c from central Gaussian to exponential tail varies with time for all n_{HA5} as $\sim \Delta t^{0.24\pm0.03}$. As the exponent is less than 1, we can infer that the dynamic heterogeneity persists till the residence of water in the subdiffusive region. The width (σ^2) of the central Gaussian and the decay exponent (λ) of the tail part for all cases vary with time as $\sigma^2 \sim \Delta t^{0.61\pm0.005}$ and $\lambda \sim \Delta t^{0.42\pm0.02}$ respectively. Furthermore, we compute the underlying distribution of translational diffusivities $P(D_T)$ from $G_s(r, \Delta t)$ using Lucy's deconvolution method. $P(D_T)$ for the Δt=5 ps and Δt=10 ps are shown in Figure 4.6(d). We observe that a wide range of D_T contributes to the distribution. The peak at very small D_T is due to the water molecules in the vicinity of the lipid bilayer. At Δt=10ps the peaks get sharper. Importantly, we note that HA concentration has a very negligible effect on the distribution at Δt=5ps. However, the peak of $P(D_T)$ enhances at the small D_T value with increasing n_{HA5} at Δt=10ps.

Next, we inspect how the heterogeneity of the interfacial waters in the diffusive region of the HA-water and DPPC interface modifies as we change HA concentrations. ln$G_T(r, \Delta t)$ vs Δt data for n_{HA5}=10, 30 and 50 are shown in Figure 4.7(a), 4.7(b) and 4.7(c) respectively. The left(L) and right(R) panels show ln$G_T(r, \Delta t)$ vs Δt data for Δt=10ps (circles) and 20ps (squares) respectively. $G_T(r, \Delta t)$ shows a Gaussian central part (solid line) with a Gaussian tail (broken line) for all cases. The double Gaussian nature of G_T indicates two diffusion coefficients of the interfacial waters. The r_c varies with time as $\sim \Delta t^{0.42\pm0.1}$. Thus the heterogeneity persists till the residence time. In addition, the widths of the two Gaussians σ_1^2 and σ_2^2 vary with time almost linearly. From the linear time variation of the widths of respective Gaussians, we obtain two diffusion coefficients: D_T^1 and D_T^2. The slower component is expected from the water molecules interacting with HA chains.

We also derive the underlying probability distributions of diffusivities $P(D_T)$. $P(D_T)$ for different n_{HA5} are shown in Figure 4.7(d) for Δt=10ps (L) and Δt=20ps (R). We note that $P(D_T)$ at both times spans a wide range of diffusivities. In both times, as n_{HA5} increases, diffusivity at smaller D_T value emerges, indicating increasingly sluggish water dynamics, which is in agreement with earlier studies.[27,68] We compute the average diffusivity $\langle D_T \rangle$ from $P(D_T)$. $\langle D_T \rangle$ for different n_{HA5} along with D_T^1 and D_T^2 are shown in Figure 4.8. $\langle D_T \rangle$ is close to the mean value of D_T^1 and D_T^2. We find that D_T^1, D_T^2 and $\langle D_T \rangle$ decrease with increase in n_{HA5}. $\langle D_T \rangle$ for different n_{HA5} are close to the diffusion coefficients obtained from the MSD data in *chapter 3* (see section 3.3.2).

(b) rvHf $G_R(\phi, \Delta t)$.-

Now we compute $G_R(\phi, \Delta t)$ for the interfacial water molecules at the subdiffusive region of HA-water and DPPC interface as HA concentrations vary. ln$G_R(\phi, \Delta t)$ for n_{HA5}=10, 30 and 50 in the subdiffusive interface are shown in Figure 4.9(a)-(c) respectively for Δt=5ps (circles, left panel, L) and Δt=10ps (squares, right panel, R). In all three cases, we observe exponential tails which follow the central Gaussian. The crossover angle ϕ_c does not change with time, hence heterogeneity persists throughout the complete residence time of

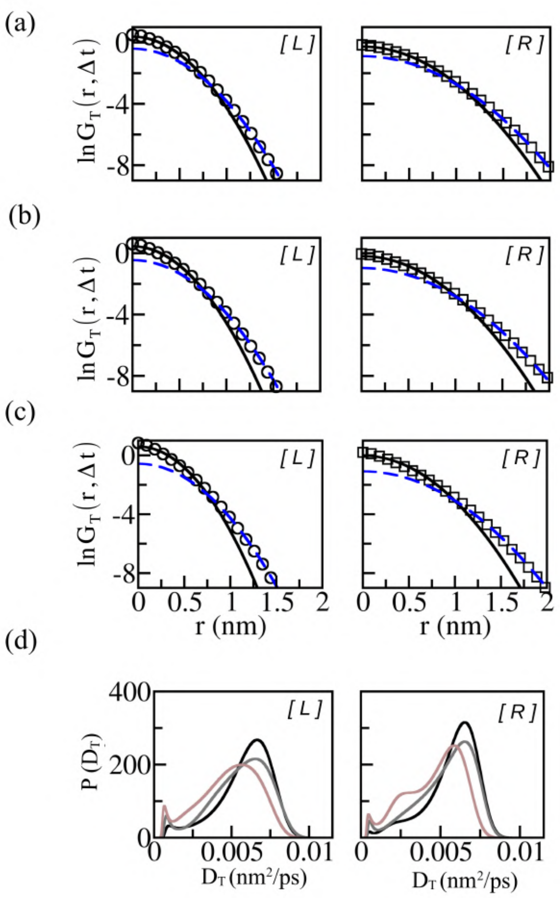

Figure 4.7: ln$G_T(r, \Delta t)$ vs Δt plot in the diffusive interface for (a) n$_{\text{HA5}}$=10 (b)n$_{\text{HA5}}$ = 30 and (c) n$_{\text{HA5}}$ = 50 for Δt=10ps (*circles*, left panels *[L]*) and for Δt=20ps (*squares*, right panels *[R]*). *Solid* and *broken* lines indicate the best-fitted central Gaussian part and the Gaussian tail respectively. (d)$P(D_T)$ in the diffusive interface for Δt=10ps (left panel *[L]*) and 20ps (right panel *[R]*) for n$_{\text{HA5}}$=10 (*solid black line*), 30 (*solid gray line*) and 50 (*solid brown line*).

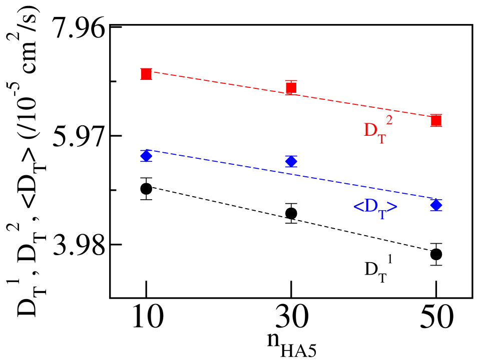

Figure 4.8: D_T^1, D_T^2 and $\langle D_T \rangle$ for different n$_{\text{HA5}}$

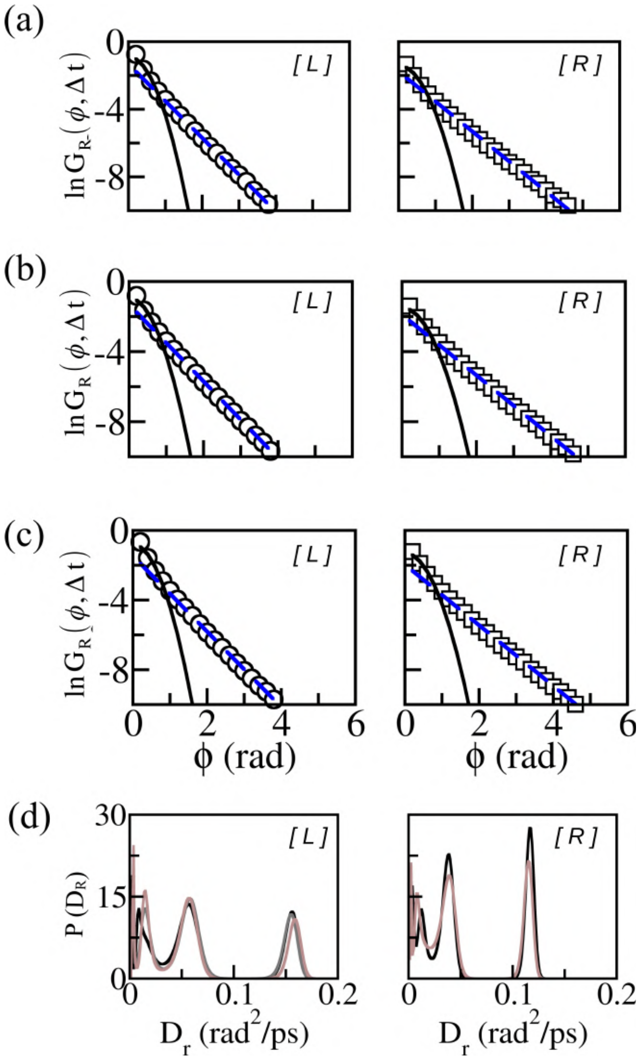

Figure 4.9: ln$G_R(\phi, \Delta t)$ vs Δt plot in the subdiffusive interface for (a) n_{HA5}=10 (b) n_{HA5}=30 and (c)n_{HA5}=50. The left (*[L]*) and right panels (*[R]*) show data for Δt=5ps (*circles*) and Δt=10ps (*squares*) respectively. *Solid* and *broken* line shows the best-fitted central Gaussian part and the exponential tail. (d) $P(D_R)$ for Δt=5ps (left panel *[L]*) and Δt=10ps (right panel *[R]*) for n_{HA5}=10 (*black line*), 30 (*gray line*) and 50 (*brown line*).

water for all n_{HA5}. The width of the central Gaussian σ^2 varies with time as $\sim \Delta t^{0.30\pm0.02}$ and the decay exponent of the exponential tail λ varies with time as $\sim \Delta t^{0.30\pm0.05}$. We also compute the underlying distribution $P(D_R)$ of rotational diffusivity D_R. $P(D_R)$ for Δt=5ps and Δt=10ps are shown in Figure 4.9(d) (left(L) and right(R) panel respectively). In both cases, $P(D_R)$ exhibits multiple peaks. At Δt=10ps, the peaks are less in number and slightly sharper compared to those at Δt=5ps.

Next, we compute $G_R(\phi, \Delta t)$ of the interfacial waters in the diffusive region as HA concentrations vary. ln$G_R(\phi, \Delta t)$ for n_{HA5}=10, 30 and 50 in the diffusive interface are shown in Figure 4.10(a)-(c) respectively for Δt=10ps (circles, left panel,L) and Δt=20ps (squares, right panel,R). For all n_{HA5} $G_R(\phi, \Delta t)$ has a central Gaussian and an exponential tail at Δt=10ps. At Δt=20ps $G_R(\phi, \Delta t)$ takes double Gaussian form. The transition from exponential to Gaussian tail with time essentially indicates lesser heterogeneity in the rotational dynamics. We observe λ of the exponential tail varies with time as $\sim \Delta t^{0.34\pm0.06}$ for all n_{HA5}. On the other hand, the σ_1^2 and σ_2^2 of the central and tail Gaussian of rvhf vary with time almost linearly. We also obtain the distribution of rotational diffusion coefficients, $P(D_R)$ from the rvhf profile. $P(D_R)$ for different concentrations are shown in Figure 4.10(d) for Δt=10ps and Δt=20ps. Multiple peaks are noted in the $P(D_R)$ profile which implies dynamic heterogeneity. However, the peaks at the very small values of D$_R$ are absent in the diffusive region, which was present in the subdiffusive

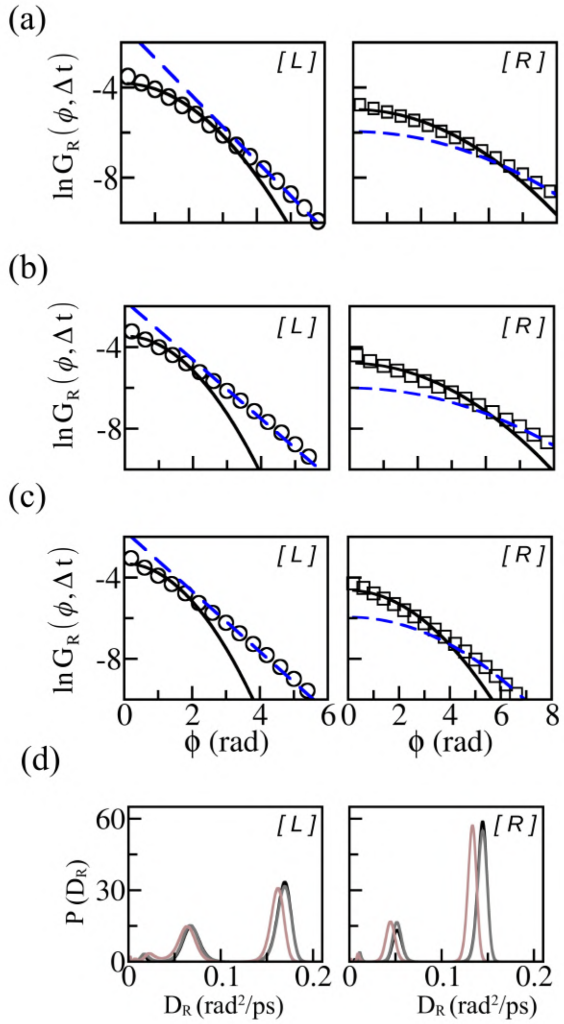

Figure 4.10: ln$G_R(\phi, \Delta t)$ vs Δt plot in the diffusive interface for (a) n_{HA5}=10 (b) n_{HA5}=30 and (c)n_{HA5}=50. The left (*[L]*) and right panels (*[R]*) show data for Δt=10ps (*circles*) and Δt=20ps (*squares*) respectively. *Solid* and *broken* line shows the best-fitted central Gaussian part and the exponential/Gaussian tail. (d) $P(D_R)$ for Δt=10ps (left panel *[L]*) and Δt=20ps (right panel *[R]*) for n_{HA5}=10 (*solid black line*), 30 (*solid gray line*) and 50 (*solid brown line*).

region. At Δt=20ps peaks of $P(D_R)$ are sharper than Δt=10ps. The average rotational diffusivity $\langle D_R \rangle$ for different n_{HA5} in the diffusive interface are shown in Figure 4.11. The $\langle D_R \rangle$ values are comparable to the D_R^W data as shown in Figure 3.6(e) in *chapter 3*.

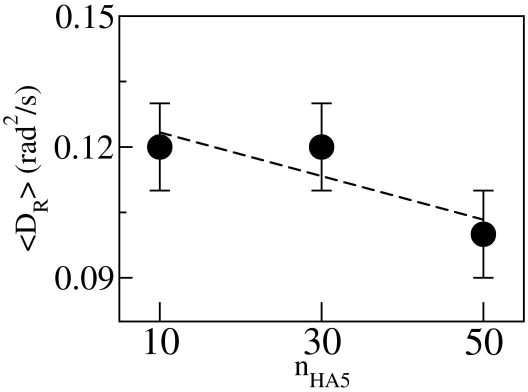

Figure 4.11: $\langle D_R \rangle$ for different n_{HA5}

4.3.3 Self van Hove function of waters at HA-water and DPPC interface for varying HA chain size

Next, we investigate how the dynamic heterogeneity of the interfacial waters in the subdiffusive and diffusive interfaces responds as the HA chain size (N) changes.

(a) tvHf $G_T(r, \Delta t)$.-

Figure 4.12(a), 4.12(b), 4.12(c) describes ln$G_T(r, \Delta t)$ vs Δt data for N=1,5 and 10 respectively in the subdiffusive interface. The left(L) panel shows the data for Δt=5ps, whereas the right(R) panel describes data for Δt=10ps. In both the observation times, $G_T(r, \Delta t)$ shows a central Gaussian with an exponential tail. The crossover length r_c varies with time as $\sim \Delta t^{0.24\pm0.02}$. Hence, the heterogeneity persists till the residence time of water in the subdiffusive region. The width and decay exponent of the central and tail part vary with time as $\sigma^2 \sim \Delta t^{0.60\pm0.01}$ and $\lambda \sim \Delta t^{0.44\pm0.03}$ respectively. We compute the distribution of translational diffusivity $P(D_T)$ from the $G_T(r, \Delta t)$ data. $P(D_T)$ for Δt=5ps and 10ps are shown in the left and right panel of Figure 4.12(d). $P(D_T)$ show peaks at a very small value of D_T and contribution from a wide range of D_T values is noted, which indicates the signature of dynamic heterogeneity. The sharp peak at the very small D_T value implies dynamically arrested water molecules very close to the bilayer.

Next, we discuss $G_T(r, \Delta t)$ in the diffusive interface. Figure 4.13(a), 4.13(b), 4.13(c) describes ln$G_T(r, \Delta t)$ vs Δt data for N=1,5 and 10 respectively. The left(L) panel depicts the data for Δt=10ps, whereas the right panel depicts data for Δt=20ps. In both the observation times, $G_T(r, \Delta t)$ has a central Gaussian with a Gaussian tail. The double

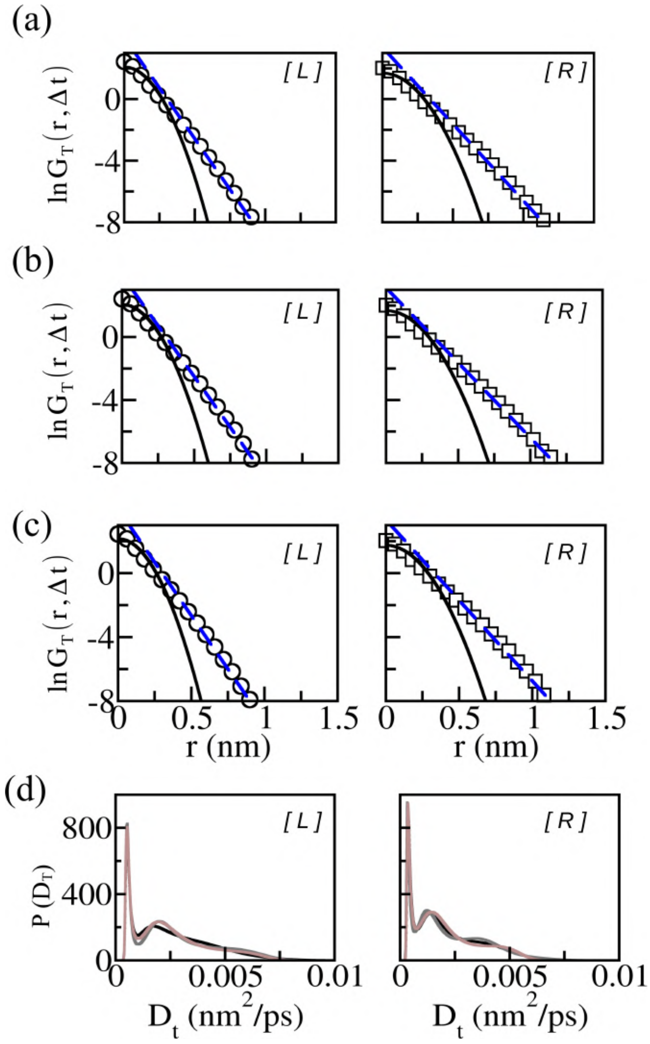

Figure 4.12: ln$G_T(r, \Delta t)$ vs Δt plot for (a) N=1, (b) N=5 and (c) N=10 in the subdiffusive interface for Δt=5ps (*circles*, left panels *[L]*) and Δt=10ps (*squares*, right panels *[R]*). *Solid* lines show the central Gaussian of G_T where *broken* lines imply the the exponential tails. (c) Distribution of translational diffusivities D_T for N=1 (*black line*), N=5 (*gray line*) and N=10 (*brown line*) Δt=5ps (left panel *[L]*) and Δt=10ps (right panel *[R]*).

Gaussian nature indicates heterogeneity in the interfacial water dynamics with two diffusion coefficients. The crossover distance r_c varies with time as $\sim \Delta t^{0.40\pm0.10}$. We note that both the widths of the two fitted Gaussian σ_1^2 and σ_2^2 vary linearly with time. From the linear σ_1^2 and σ_2^2 we compute two diffusion coefficients of the interfacial waters D_T^1 and D_T^2.

The underlying distribution of diffusion constants $P(D_T)$ is also obtained. $P(D_T)$ for Δt=10ps and Δt=20ps are shown in the left(L) and right(R) panels of Figure 4.13(d) respectively. $P(D_T)$ is almost the same for all N values. We note contributions from a broad range of D_T in $P(D_T)$. We also compute the average diffusivity, $\langle D_T \rangle$ from the $P(D_T)$. We show $\langle D_T \rangle$ along with D_T^1 and D_T^2 in Figure 4.14. We find $\langle D^T \rangle$ is close to

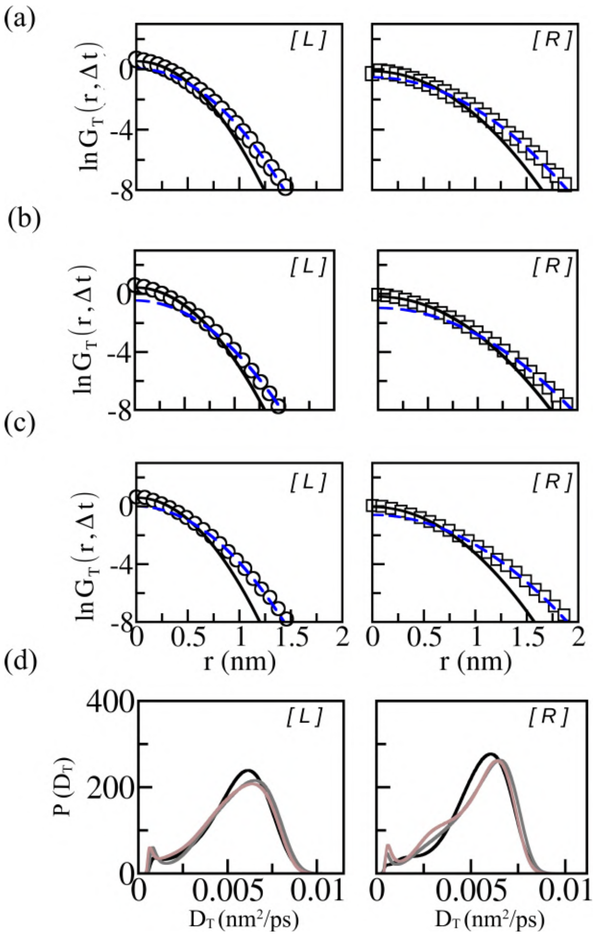

Figure 4.13: ln$G_T(r, \Delta t)$ vs Δt plot for (a) N=1, (b) N=5 and (c) N=10 for Δt=10ps (*circles*, left panels *[L]*) and Δt=20ps (*squares*, right panels *[R]*). *Solid* lines show the central Gaussian of G_T where *broken* lines imply the the Gaussian tails. (c) Distribution of translational diffusivities D_T for N=1 (*solid black line*), N=5 (*solid gray line*) and N=10 (*solid brown line*) Δt=10ps (left panel *[L]*) and Δt=20ps (right panel *[R]*).

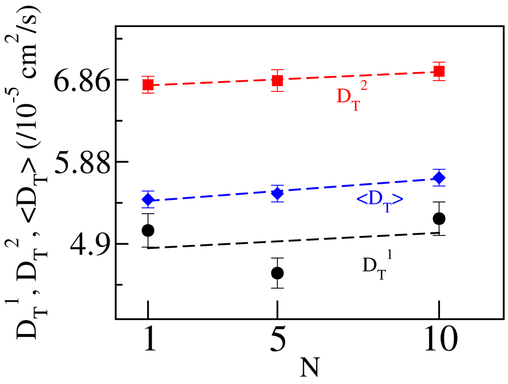

Figure 4.14: D_T^1, D_T^2 and $\langle D_T \rangle$ for different N

the mean value of D_T^1 and D_T^2. The diffusivities are minutely sensitive on N which is consistent with our earlier reports in *chapter 3* (see section 3.3.2).[27]

(b) rvHf $G_R(\phi, \Delta t)$:-

Next, we compute rotational svhf $G_R(\phi, \Delta t)$ at the subdiffusive interface of HA-water and DPPC. ln$G_R(\phi, \Delta t)$ vs ϕ plots for N=1,5 and 10 are shown in Figure 4.15(a), 4.15(b) and 4.15(c) respectively. ln$G_R(\phi, \Delta t)$ for Δt=5 ps and Δt=10 ps are described in the left(L) and right(R) panels respectively. We note the central Gaussian is followed by an exponential tail in all cases. The exponential characteristics of the tail remain the same for both observation times. We find that the crossover angle ϕ_c remains unchanged with time, hence the dynamic heterogeneity persists till the residence time of water at the subdiffusive interface (region B). Moreover, we compute the time dependence

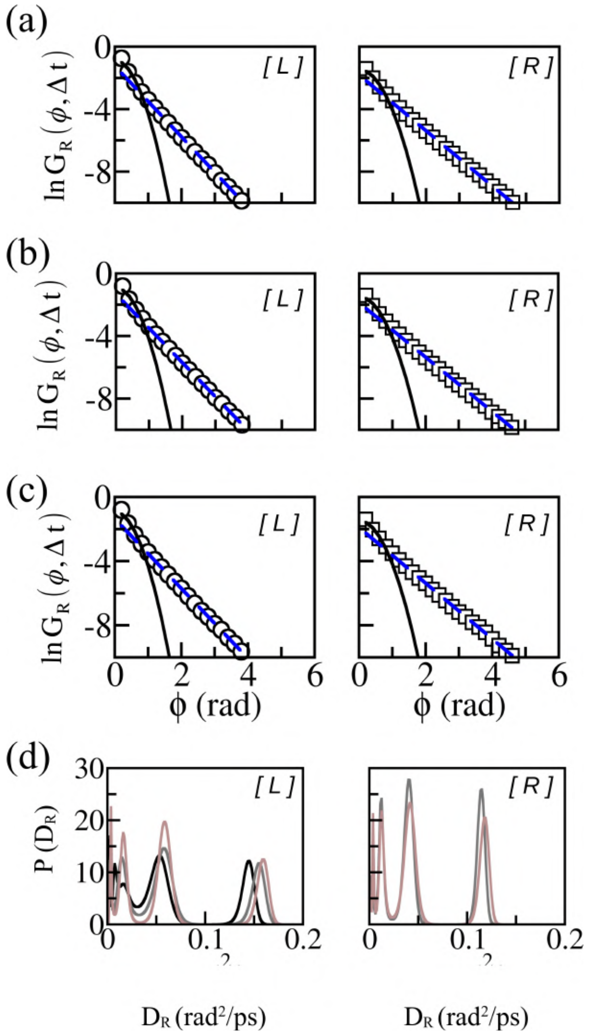

Figure 4.15: ln$G_R(\phi, \Delta t)$ vs Δt plot for (a) N=1, (b) N=5 and (c) N =10 for Δt=5ps(*left* panel *[L]*) and Δt=10ps (*right* panel *[R]*). *Solid* and *broken* line shows the best-fitted central Gaussian part and the exponential tail. (d) $P(D_R)$ for Δt=10ps (*left* panel *[L]*) and Δt=20ps (*right* panel *[R]*). N=1 :*solid black* line, N=5 :*solid gray* line, N=10 :*solid brown* line.

of σ^2 and λ of the fitted central Gaussian and the exponential tail. The exponents are almost the same for all N where $\sigma^2 \sim \Delta t^{0.30\pm0.02}$ and $\lambda \sim \Delta t^{0.32\pm0.02}$. Additionally, we compute the distribution of rotational diffusion $P(D_R)$ at the subdiffusive interface from $G_R(\phi, \Delta t)$ data. $P(D_R)$ for Δt=5ps and 10ps are shown in Figure 4.15(d) (L and R panels respectively). Multiple peaks are observed in $P(D_R)$ at both times which results in the exponential tail of the $G_R(\phi, \Delta t)$. $P(D_R)$ data indicates multiple single-particle Gaussian processes hence dynamic heterogeneity. As time increases the peaks become sharper suggesting lesser heterogeneity.

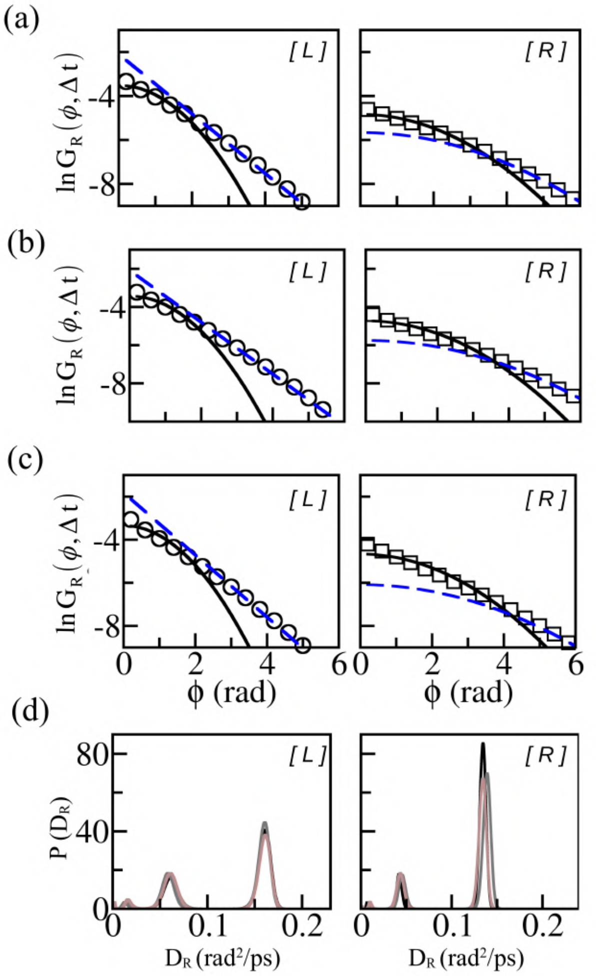

Figure 4.16: ln$G_R(\phi, \Delta t)$ vs Δt plot for (a) N=1, (b) N=5 and (c) N =10 for Δt=10ps(*left* panel *[L]*). Δt=20ps (*right* panel *[R]*). *Solid* and *broken* line shows the best-fitted central Gaussian part and the Gaussian tail. (d) $P(D_R)$ for Δt=10ps (*left* panel *[L]*) and Δt=20ps (*right* panel *[R]*). N=1 :*solid black* line, N=5 :*solid gray* line, N=10 :*solid brown* line.

We also investigate the $G_R(\phi, \Delta t)$ of the water molecules at the diffusive interface of HA-water and DPPC bilayer as N changes. $lnG_R(\phi, \Delta t)$ vs ϕ for N=1, 5 and 10 are shown in Figure 4.16(a), 4.16(b) and 4.16(c) respectively. The data are shown for Δt =10ps

(L) and Δt =20ps (R). $G_R(\phi, \Delta t)$ shows an exponential tail at Δt=10ps for each N which follows a central Gaussian. As time evolves to Δt=20ps, we find that $G_R(\phi, \Delta t)$ exhibits a Gaussian tail. The crossover angle ϕ_c evolves with time with exponents between 0.2 and 0.3 for all N. Hence, dynamic heterogeneity of water molecules persists in the diffusive interface till their residence time. We also compute the time dependence of σ^2 of the fitted Gaussians (both central and tail) and the λ of the exponential tails. The σ^2, be it of the central Gaussian or the Gaussian tail, grows almost linearly with time. On the other hand, λ of the exponential tail grows with time as $\sim t^{0.40\pm0.03}$.

We also obtain the underlying distribution of diffusivities $P(D_R)$ for all the cases. $P(D_R)$ for all N are shown in Figure 4.16(d) for Δt=10ps (L) and Δt=20ps (R). We note $P(D_R)$ at Δt=20ps is more sharply peaked than those at Δt=10ps, implying lesser dynamic heterogeneity as the observation time grows. Average diffusivity $\langle D_R \rangle$ obtained from $P(D_R)$ for different N are shown in Figure 4.17. $\langle D_R \rangle$ remains almost the same for varying N.

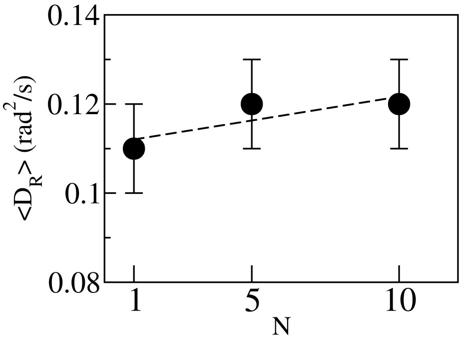

Figure 4.17: $\langle D_R \rangle$ for different N

4.4 Conclusion

In summary, we report here a systematic study of dynamic heterogeneity at the HA-water and DPPC interface and the effect of chain size and concentration of Hyaluronic acid on the dynamic heterogeneity of the interfacial waters. We find that the dynamic heterogeneity persists till the residence time of water in both subdiffusive and diffusive regions of the HA-water and DPPC interface. In the subdiffusive region, we observe multiple peaks and peaks at extremely low diffusion in the distribution of diffusivity for both translation and rotation of the interfacial waters. In the diffusive region, we observe a broad peak in translation. For rotation, we find a sharp principal peak along with small secondary peaks in the distribution. We also note that as n_{HA5} increases, both the mean translational and rotational diffusion coefficients obtained from the diffusion distribution decrease. Whereas, they remain almost the same as we change the values of N, which is consistent with the results obtained from the MSD data the *chapter 3*.[27]

Dynamic heterogeneity controls diffusion at the interface[24] and plays a crucial role in the viscoelastic response of the system.[116] Previous reports show that the alternation of HA concentration and HA chain size modulate the viscous properties and cellular lubrication in pathological conditions.[20,117,118] Our study may help understand the viscoelastic response of HA-lipid complexes from the microscopic point of view.

Chapter 5

Structure and dynamics of a single polyampholyte chain in external magnetic field

5.1 Introduction

A polymer chain containing both positively and negatively charged sites is called a polyampholyte (PA).[119–121] Naturally occurring and synthetic polymers with basic and acidic groups are typical examples of PA chains.[120] Polyampholytes are charge-neutral when the numbers of oppositely charged sites are equal. However, when these numbers are imbalanced, the PA chains acquire an overall charge.[121] This typically happens at pH levels far from the isoelectric point (pI), when the significant charge imbalance causes PA chains to behave like polyelectrolytes.[121,122] Proteins, as natural polyampholytes, also contain positively and negatively charged amino acid residues, with their net charge determined by the surrounding pH.[10] Polyampholytes are biologically significant and have diverse technological applications, including coacervates,[123] low-friction materials for synovial joints,[124] and anti-fouling coatings.[125] Their structural and kinetic features have been extensively studied. Many studies have specifically looked at how the charge patterns and concentration of polyampholytes affect their properties.[126,127]

From classical electromagnetic theory, we know that charged bodies and systems with permanent magnetic moments interact with external magnetic fields.[28] External magnetic fields can affect the structure and functions of biomolecules with charged groups.[11,12] Moreover, numerous technologically significant scenarios have made use of magnetic field effects, such as magnetic tweezers,[128] aligning materials with magnetic susceptibilities,[129] directed self-assembly,[130] and so on. Aligning block co-polymer domains with anisotropic magnetic susceptibilities in a specific direction is one of the primary uses of magnetic fields.[13,14] The alignment of block copolymers is important due to their highly tunable morphologies and functionalities.[15] Rod-coil block copolymers show alignment across a broad range of magnetic field strengths.[13] However, a thorough theoretical understanding of the microscopic behavior of a charged polymeric sample under magnetic fields is still lacking. In this chapter, we investigate the response of a model polyampholyte (PA) chain under the perturbation of an externally applied magnetic field.

MD simulation of a two-dimensional Yukawa plasma system under a magnetic field demonstrates that the field has no effect on the static properties of the system such as radial distribution functions.[30] However, the mobility of the particles is inversely proportional to the applied magnetic field.[30,131] Additionally, it is demonstrated that the magnetic field increases parallel heat transport at high pressure or low temperature and decreases perpendicular heat transport for strongly coupled plasma.[132] According to a recent study, the dynamics of the Rouse dimer are enhanced when an external magnetic field is introduced, displaying transient superballistic behavior.[32]

The MD algorithms used in these studies account for the presence of a magnetic field.[133–135] Nevertheless, these methods are not symplectic, meaning that no conserved quantity exists.[34] Furthermore, they do not reduce to a standard propagation scheme in the absence of the magnetic field and are not suitable for multiple degrees of freedom.[33,34] Very recently a symplectic integrator has been developed within the Liouvillian formulation, where the magnetic vector potential is included in the kinetic energy term of the conserved Hamiltonian.[33,35] In realistic systems, this approach is proven to be accurate and stable.[33] For instance, the transport characteristics of molten NaCl salt are investigated using the integrator.[33] Furthermore, ionic magnetoresistance and the ionic Hall effect are measured for AgI salt using this technique.[34] Nevertheless, this scheme has not been used so far to understand the dynamics of charged polymeric materials under an external magnetic field.

In this chapter, we investigate the dynamics of a single charge neutral polyampholyte (PA) chain with an equal number of positively and negatively charged beads in a Lennard-Jones solvent in the presence of an external magnetic field using the recently developed symplectic integrator.[33–35] The positively and negatively charged beads of the PA chain are arranged here in a block fashion. Unlike other models,[136,137] the chain does not have an explicit magnetic moment. Instead, the charge of the beads interacts with the external magnetic field. The field and the thermal velocities of the polymer beads give rise to the Lorentz force.[28] Here, we study the static and dynamic properties of the PA chain. We find that closed chain conformations get prominent as the field is applied. The induced moment of the chain increases and aligns faster along the field direction as we increase field strength. Moreover, the translational diffusivity of the chain decreases in the perpendicular plane of the field direction and increases along the field direction.

5.2 Model and Simulation details

We consider a bead-spring model of a single 40-monomer polyampholyte (PA) chain in Lennard-Jones (LJ) solvent corresponding to the oxygen atom of water molecules. The PA chain has 20 negatively charged and 20 positively charged beads and is neutral overall. The charged beads are arranged in a block arrangement. Both the beads and the solvents are spherical shapes of diameter σ. The solvent-solvent and polymer-solvent interaction are modeled via 12-6 Lennard-Jones (LJ) interaction of the form: $V_{LJ} = 4\epsilon[(\frac{\sigma}{r})^{12} - (\frac{\sigma}{r})^{6}]$. All non-bonded interactions are truncated at a cut-off length of 3.5σ.

The bonded interactions between the polymer beads consist of harmonic bond potential and bond-angle potential. The harmonic bond potential between the ith and (i+1)th the polymer beads is modeled[138] as $V_b = \frac{1}{2}k_b(r_i - r_{i+1})^2$, where r_i and r_{i+1} is the positions of the ith and (i+1)th beads from a fixed origin. The angular potential between two consecutive bonds is expressed[80] as $V_a = k_\theta(1 - \cos\theta)$ where θ is the angle between two consecutive bonds. We set k$_b$ = $30\epsilon/\sigma^2$ and k_θ = 10ϵ. Excluded volume interactions between any two beads are modeled as the repulsive part of the Lennard-Jones interaction:$V_{LJ}^r = 4\epsilon(\frac{\sigma}{r_{ij}})^{12}$ where r$_{ij}$ is the distance between ith and jth beads. The screened Coulomb interactions between the charged beads are modeled as $V_{el} = V_0\frac{q_iq_j}{r}e^{-r_{ij}/\lambda}$ where the potential strength $V_0 = 5\epsilon$ and Debye screening length $\lambda = 0.5\sigma$.[111,139]

In the simulation, we apply the magnetic field along the z-direction. We solve the equation of motion derived from the Hamiltonian $H = \frac{(\vec{P}-q\vec{A})^2}{2m} + V(r)$ where $\vec{P}$ is the momentum and V is the potential energy.[33,35] Here the Hamiltonian H incorporates magnetic field via vector potential $\vec{A}$. As B is directed along the z-axis, $\vec{A} = -\frac{B}{2}y\hat{x} + \frac{B}{2}x\hat{y}$. The equations of motions for position and momentum are taken from ref.[35] (details of this method are discussed in Appendix A5.1; for the equations of motion used in this study, see equations from A5.1.1 to A5.1.4 of Appendix A5.1). Using the expression from Lorentz force, B is given by $\frac{M\omega_L}{e}$, where M is mass, $\omega_L = \frac{eB}{M}$ is Larmor frequency, and e= 1.6×10^{-19} Coulomb is the electronic charge of the beads.[28] We chose $M = 100$ Dalton representing the typical molecular weight of amino acid residues[140] and defined the time unit for our system $1/\omega_L$ =1 μs. With this choice, the magnetic field B is identical in the reduced and real unit. The reduced temperature of the simulation is fixed at $T^* = k_BT/\epsilon = 1.2$[141] where k_B is the Boltzmann constant and T is the temperature of the system in the real unit. We set Lennard-Jones energy parameter ϵ as the energy unit of our simulation. The bead diameter σ is set as the length unit. The beads and solvents are taken to be of the same mass m for simplicity and it is taken as the mass unit.

We fix the temperature during the simulation via the Nose-Hoover thermostat,[33,35] where the kinetic energy fluctuates around the target value $K^* = \frac{3}{2}Nk_BT$. All simulations are performed in a cubic simulation box of size $16.8 \times 16.8 \times 16.8\sigma^3$ and we use periodic boundary conditions in three directions. The polymer density of the system is kept at $0.008\sigma^{-3}$ and solvent density is $0.86\sigma^{-3}$.[142,143] The integration time-step is set to $dt = 0.001\tau$, and all simulations are performed for 3×10^6 MD steps. Initial 10^4 steps are used for NVE equilibration, followed by another 10^4 steps for NVT equilibration without the field. After this, the magnetic field is applied to the system. We allow the first 10^6 steps for equilibration, and the remaining simulation time is considered the production run.

For all static and dynamic quantities reported here, we take an average over five independent trajectories, each with different initial positions and velocities of the polymer beads.

5.2.1 Analysis

Radius of gyration and end-to-end distance

The radius of gyration of the polymer chain is calculated using the formula: $R_g = \frac{1}{N}\sum_{i=1}^{N}(\vec{r_i} - \vec{r_c})^2$. Here $\vec{r_i}$ and $\vec{r_c}$ is the position vector of the i'th bead and the center of mass of the chain respectively. The end-to-end distance of the polymer is computed using the formula $R_e = |\vec{r}_1 - \vec{r}_N|$, where $\vec{r}_1$ and $\vec{r}_N$ is the position vector of first and last bead of the chain.

Induced magnetic moment

The induced magnetic moment of the PA chain is given by

$$\vec{\mu} = \frac{1}{2}\sum_{i}^{N} q_i(\vec{r_i} \times \vec{v_i}) \tag{5.1}$$

here the sum is over all N number of beads.[144] We examine the components of the induced magnetic moment along the three spatial axes: μ_x, μ_y, and μ_z. The rotational dynamics of $\vec{\mu}$ is investigated by computing the first rank auto-correlation function of $\vec{\mu}$ given by

$$C(t) = \frac{\vec{\mu}(t).\vec{\mu}(0)}{\vec{\mu}(0).\vec{\mu}(0)} \tag{5.2}$$

We fit single exponential function of the form $ae^{-t/\tau} + b$ to C(t) to obtain the rotational timescale τ.

Mean squared displacements

The mean squared displacement (MSD) of the chain in the perpendicular plane (x-y plane) of the magnetic field direction is given by $\Delta r_{\perp}^2(t) = \langle \sum_i^N [\vec{r}_i^{xy}(t) - \vec{r}_i^{xy}(0)]^2 \rangle$. Here, $\vec{r}_i^{xy}(t)$ denotes the position vector of the i'th bead of the polymer in the x-y plane at time t. In the parallel direction of the field (z-direction), we compute MSD of the chain as $\Delta r_{\|}^2(t) = \langle \sum_i^N [\vec{r_i^z}(t) - \vec{r_i^z}(0)]^2 \rangle$. Here, $\vec{r_i^z}(t)$ denotes the z-component of the position vector of the i'th bead of the polymer at time t.

5.3 Results

5.3.1 Polymer conformations in equilibrium for different B values

The equilibration of the MD simulation is confirmed by the saturation of the potential energy P.E of the system and radius of gyration R_g of the PA chain. Figure 5.1(a) and 5.1(b) shows P.E vs. steps and R_g vs. steps plot respectively for the B=0 case after equilibration for a typical MD trajectory. Figure 5.1(a) and 5.1(b) describe P.E vs. steps and R_g vs. steps plot respectively for B=30 case for a typical MD trajectory in equilibrium. We observe that P.E and R_g fluctuate around a mean value. We consider this portion of the trajectory to be the equilibrated trajectory.

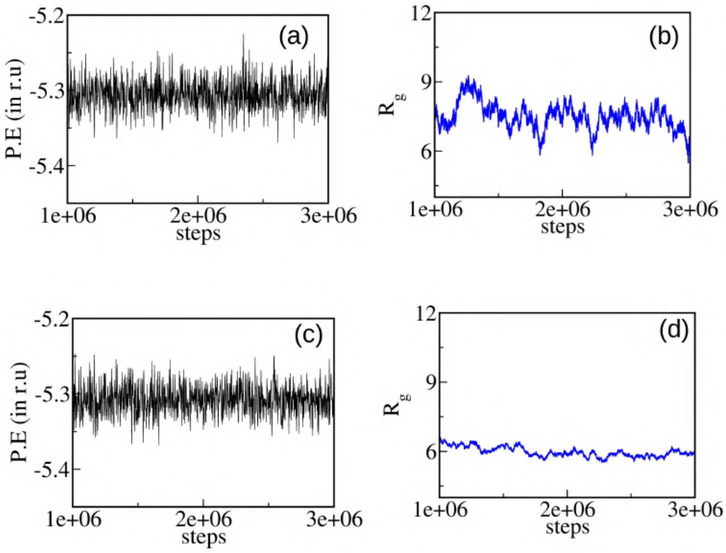

Figure 5.1: (a) Potential energy and (b) R_g vs time steps for B=0. (c) Potential energy and (d) R_g vs time steps for B=0.

Next, we look into different polymer conformations at equilibrium for different B values. We show some snapshots of the chain in Figure 5.2. It is observed that for B=0, the chain takes more extended conformation than other B values in Figure 5.2(a)(1)-(4). The conformations for finite B are shown in Figure 5.2(b)(1)-(4) for B=10, Figure 5.2(c)(1)-(4) for B=20, and Figure 5.2(c)(1)-(4) for B=30. We note closed conformations when magnetic field is applied.

(a) B=0

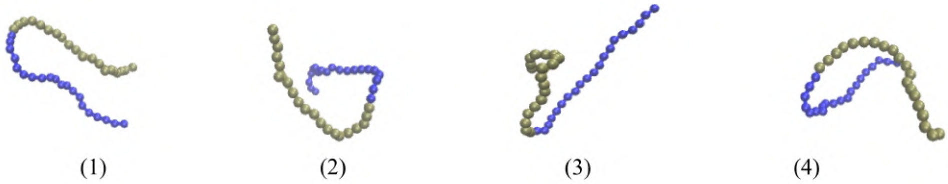

(b) B=10

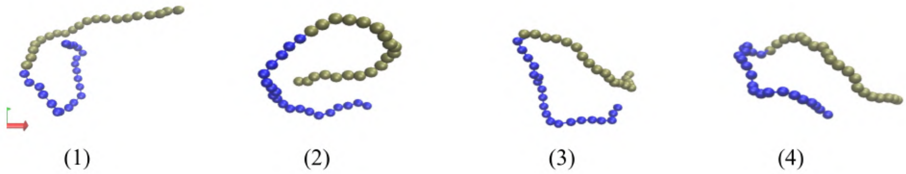

(c) B=20

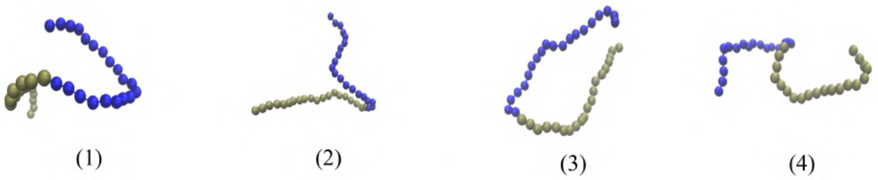

(d) B=30

Figure 5.2: Polymer conformations for (a) B=0, (b) B=10, (c) B=20, and (d) B=30 at (1) 0.5×10^6, (2) 1×10^6, (3) 2×10^6 and (4) 3×10^6 MD steps.

5.3.2 Radius of gyration and end-to-end distance of the polymer chain

Next, we inspect the effect of the magnetic field on the static properties of the polymer. To that end, we compute the distribution of the radius of gyration R_g and end-to-end distance R_e of the chain. Figure 5.3(a) shows the distribution of R_g, $H(R_g)$ for different magnetic field strengths. We observe that the peak of $H(R_g)$ slightly shifts to smaller R_g values as the magnetic field is applied. Therefore, the PA chain takes more compact conformations in presence of external field. We also compute the mean $\langle R_g \rangle$ and show the scaled $\langle R_g \rangle$ with respect to $\langle R_g^0 \rangle = (7.23 \pm 0.03)\sigma$ for B=0 case in Figure 5.3(b). We find that the $\langle R_g \rangle$ decreases compared to $\langle R_g^0 \rangle$ when the magnetic field is applied, but

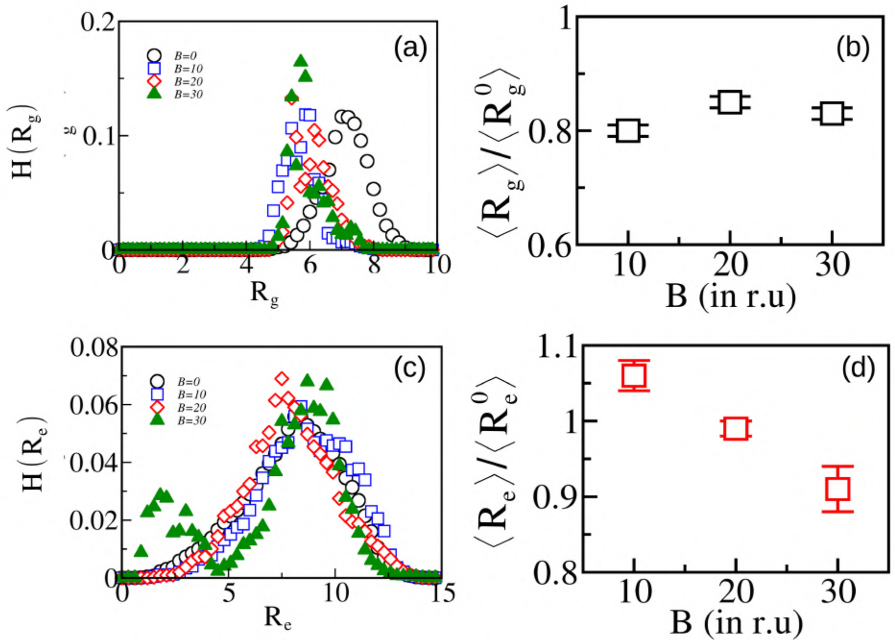

Figure 5.3: Distribution of (a) radius of gyration R_g for B=0 (*circles*), B=10 (*sqaures*), B=20 (*diamonds*), and B=30 (*triangles*). (b) $\langle R_g \rangle / \langle R_g^0 \rangle$ for different B values. (c) end-to-end distance R_e for B=0 (*circles*), B=10 (*sqaures*), B=20 (*diamonds*) and B=30 (*triangles*). (d) $\langle R_e \rangle / \langle R_e^0 \rangle$ for different B values.

remains almost the same as B increases.

We also show the distribution of R_e, $H(R_e)$ for different magnetic field strengths in Figure 5.3(b). The peak of $H(R_e)$ is observed almost at the same R_e values except for B=30. We observe a peak of $H(R_e)$ at a very small R_e value at B=30. We calculate the mean $\langle R_e \rangle$ and show the scaled $\langle R_e \rangle$ with respect to $\langle R_e^0 \rangle = (8.19 \pm 0.03)\sigma$ for B=0 case in Figure 5.3(d). We find that the $\langle R_e \rangle$ decreases linearly as field strength increases.

We further compute the distribution $H(\theta)$ where θ is the angle between the two oppositely charged segments of the PA chains. Figure 5.4 shows $H(\theta)$ for different magnetic field strengths. For B=0, we find that conformations with $\theta \approx 100^\circ$ occur most frequently, as shown in Figure 5.4(a). This implies extended polymer conformations. As the magnetic field is applied, we observe that the peak becomes sharper for B=10 and B=20 in Figure 5.4(b) and Figure 5.4(c), respectively. We also note the emergence of a secondary peak at a smaller θ value, which suggests closed polymer conformations, grows as the field strength increases. This suggests that closed polymer conformations coexist with the extended conformations as B increases. This is consistent with the snapshots shown in Figure 5.2. For B=30, in Figure 5.4(d), we find different chain conformations as there are multiple peaks in the $H(\theta)$. This indicates that the chain conformations change throughout the simulation.

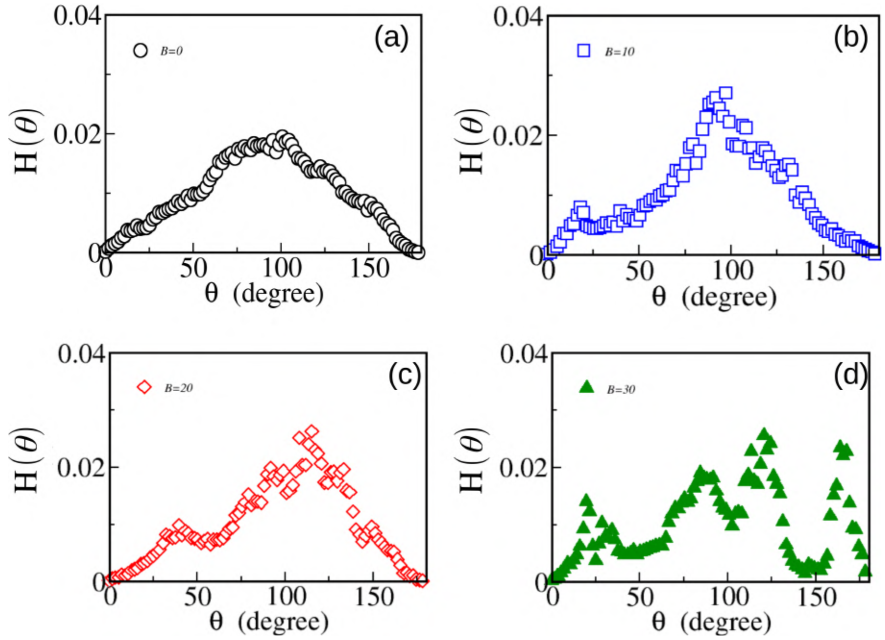

Figure 5.4: Distribution of the angle θ between the two blocks of the polymer for (a) B=0, (b) B=10, (c) B=20, and (d) B=30.

5.3.3 Induced magnetic moment of the polymer chain

The motion of the charged PA chain in presence of the externally applied magnetic field gives rise to induced magnetic moment $\vec{\mu}$ in the system given by $\vec{\mu} = \sum_i^N \vec{r}_i \times (q_i \vec{v}_i)$, where the summation is over the charged beads of the chain. We calculate the components of $\vec{\mu}$ of the PA chain along the three cartesian directions namely μ_x, μ_y, and μ_z. Figure 5.5(a), 5.5(b), and 5.5(c) show μ_x, μ_y, and μ_z respectively of the PA chain for different magnetic field intensities. We find that the chain acquires magnetic moment induced by the external magnetic field. We observe that μ_x, μ_y and μ_z all increase with increasing

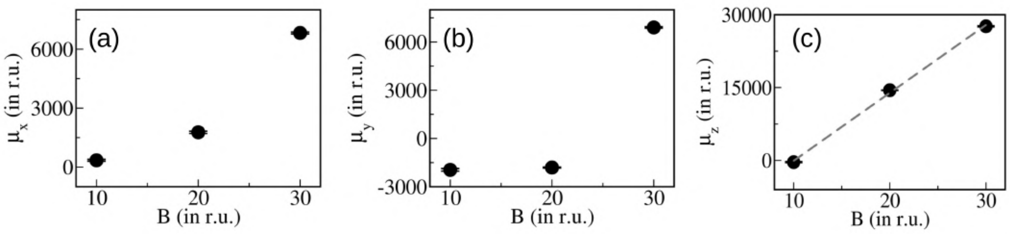

Figure 5.5: (a)μ_x, (b)μ_y and (c)μ_z of the PA chain for different field strengths. The dashed line in (c) shows the best-fitted straight line.

field strength. However, μ_z in Figure 5.5(c) increases linearly and more strongly than μ_x and μ_y with the applied magnetic field. The increase of μ_z can be explained as follows:

the external field is applied along the z-axis. Hence, the Lorentz force acts on the polymer beads in the x-y plane,[28] increasing the velocity of the beads in this plane. Now as the magnetic moment is defined as the cross-product of position and velocity of the polymer beads, the increase in velocity in the x-y plane leads to a rise in μ_z. The slope of the linear dependence is the magnetic susceptibility, χ_z= 1398.

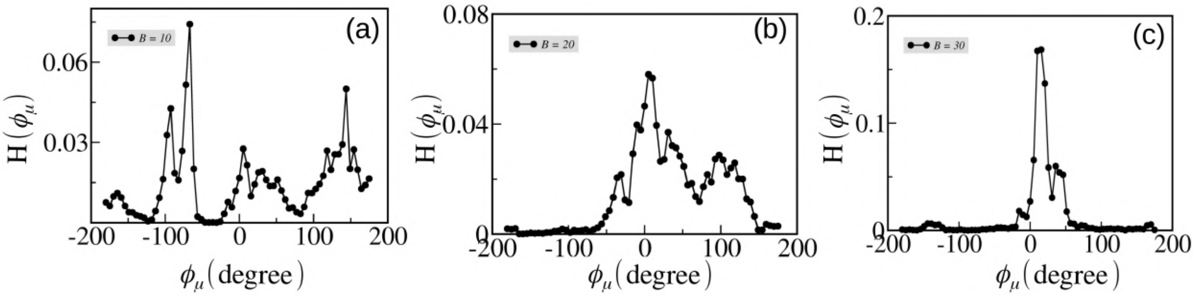

Figure 5.6: Distribution of azimuthal angle ϕ_μ for (a) B=10, (b) B=20 and (c) B=30

Additionally, we investigate the orientation of $\vec{\mu}$ of the chain at various field strengths. For varying field strengths, first we compute the azimuthal angle, ϕ_μ by $\vec{\mu}$ in the x-y plane (perpendicular plane to the applied field) for different B values. The histogram $H(\phi_\mu)$ of the azimuthal angles for the chain varying field strengths are shown in Figure 5.6. We note multiple peaks in $H(\phi_\mu)$ for B=10 in Figure 5.6(a) and B=20 in Figure 5.6(b). For B=30, we find a sharp peak in $H(\phi_\mu)$ in Figure 5.6(c). We also compute the polar angle θ_μ between $\vec{\mu}$ and applied field direction (z-axis), which essentially indicates the alignment of $\vec{\mu}$ along the field direction. Figure 5.7 shows the histogram of the polar angle $H(\theta_\mu)$ for different magnetic field strengths. For B=10 in Figure 5.7(a) we observe multiple peaks in $H(\theta_\mu)$. Now, as the field strength increases to B=20, we find a sharp peak at very small θ_μ values in Figure 5.7(b). For B=30, in Figure 5.7(c) we also note the peak at a very small θ_μ value, indicating alignment of $\vec{\mu}$ along the field direction. The peak in $H(\theta_\mu)$ and $H(\phi_\mu)$ signifies that $\vec{\mu}$ is taking a preferred orientation as field strength increases.

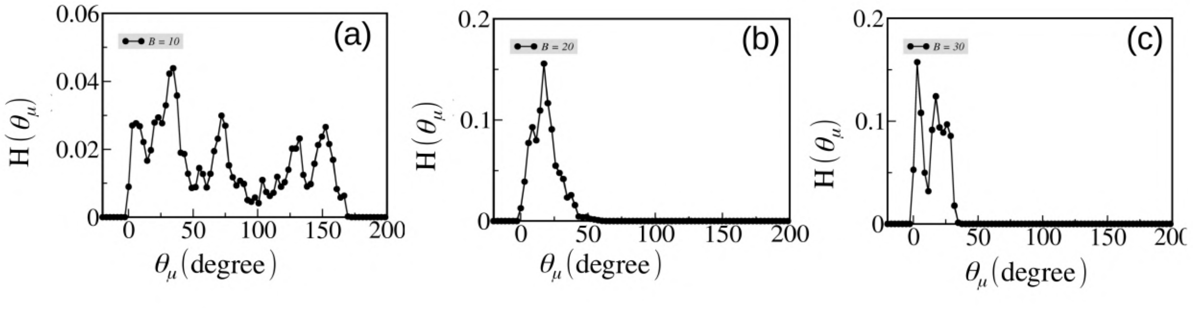

Figure 5.7: Distribution of polar angle θ_μ for (a) B=10, (b) B=20 and (c) B=30.

5.3.4 Rotational dynamics of induced magnetic moment

Next, we study the rotational dynamics of the induced dipole $\vec{\mu}(t)$ of the PA chains for different magnetic field strengths. To that end, we calculate the first rank rotational autocorrelation function C(t) of $\vec{\mu}(t)$ (see Equation 5.2). C(t) for B=10, B=20 and B=30 are shown in Figures 5.8(a), 5.8(b), and 5.8(c) respectively. We find that C(t) decays almost at the same rate for B=10 and B=20. However, it decays faster as the field strength rises to B=30. We also observe anti-correlation in the C(t) plots, which becomes more pronounced as B increases. Now, as C(t) $\sim \vec{\mu}(0).\vec{\mu}(t)$, the anticorrelation arises because the angle between $\vec{\mu}(t)$ and $\vec{\mu}(0)$ is in the second or third quadrant. As the angle $\vec{\mu}(t)$ and $\vec{\mu}(0)$ increases with B, the anticorrelation increases.

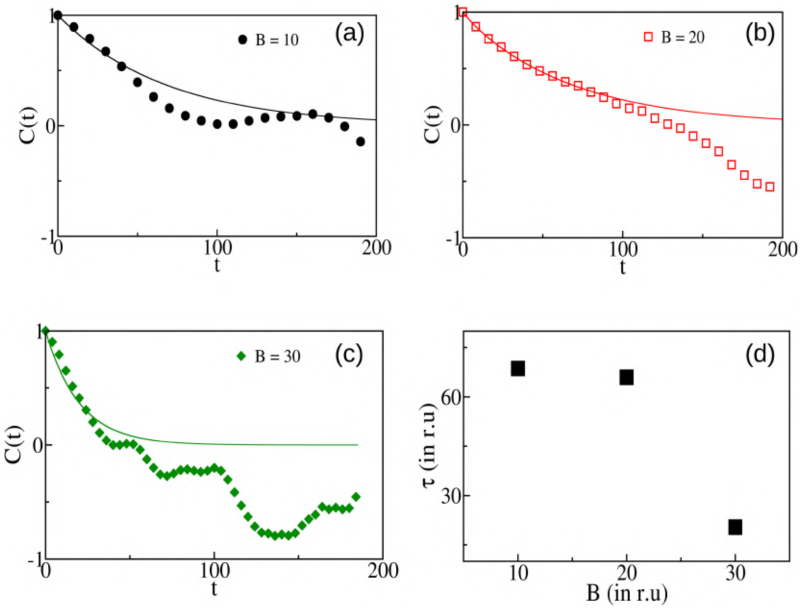

Figure 5.8: C(t) vs t plot (a) B=10, (b) B=20, and (c) B=30. Solid lines show the best-fitted exponential function. (d) Rotational autocorrelation time τ for different magnetic field strengths.

To determine the rotational timescale τ of $\vec{\mu}$, we fit an exponential function of the form $ae^{-t/\tau} + b$ to the initial part of the $C(t)$ vs t plot. The best-fitted exponential function is shown in Figure 5.8(a)-(c) with solid lines. In Figure 5.8(d) we show τ as a function of B. We find that τ is almost the same for B=10 and B=20. But it decreases substantially at higher field strength. Hence, our calculation shows faster alignment of $\vec{\mu}$ along the field direction at higher field strengths.

5.3.5 Mean squared displacement of the PA chain

Next, we study the translational motion of the PA chain in presence of external magnetic fields. We compute the mean squared displacement (MSD) of the chain beads in the

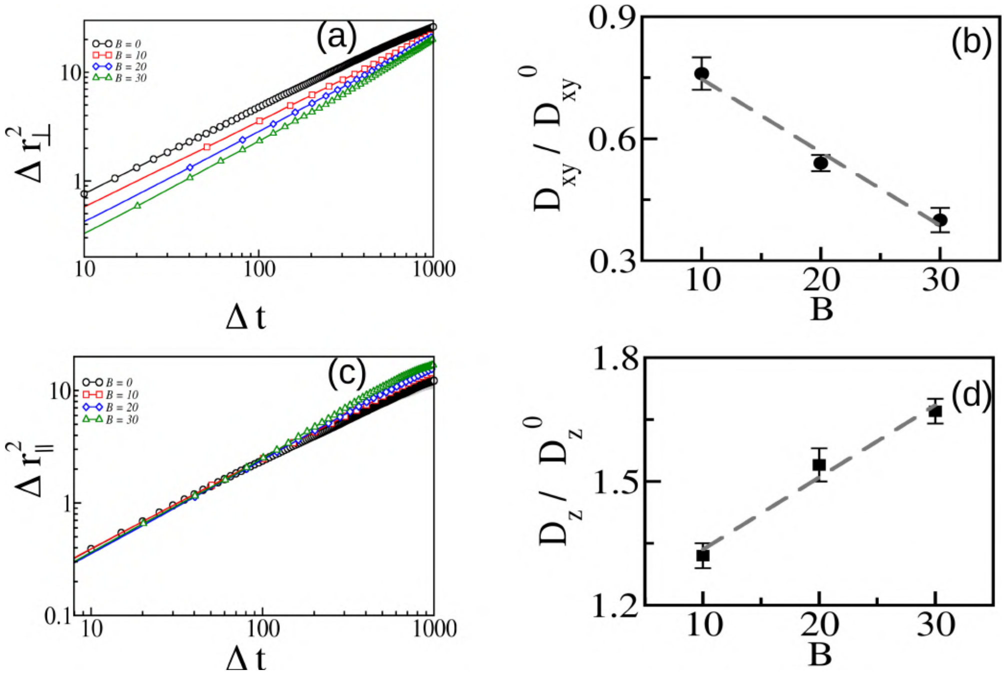

Figure 5.9: (a)$\Delta r_\perp^2$ of the polymer chain for B=0 (*circles*), B=10 (*squares*), B=20 (*diamonds*) and B=30 (*triangles*). (b)D$_{xy}$ for different B values. (c) $\Delta r_\parallel^2$ for different magnetic fields, the same symbols are used as in (a). (d) D$_z$ for different B.

perpendicular plane ($\Delta r_\perp^2$) and along the field direction ($\Delta r_\parallel^2$). Figure 5.9(a) shows $\Delta r_\perp^2$ for different field strengths. We observe that as the field strength increases $\Delta r_\perp^2$ decreases. We fit a straight line of the form $4D_{xy}\Delta t$ to the $\Delta r_\perp^2$ vs Δt plot to obtain diffusion constants D_{xy} in the perpendicular plane to the field. D_{xy}/D_{xy}^0 data for different B are described in Figure 5.9(b). Here, D_{xy}^0 is the diffusion coefficient of the PA chain in the absence of any field, and $D_{xy}^0 = 0.0041\sigma^2/\tau$. We find that as B increases D_{xy} decreases. The translational dynamics in the perpendicular plane of the field can be explained in terms of the Lorentz force. As Lorentz force acts in the perpendicular plane of the applied field direction, there is a swirling motion of the beads in the x-y plane. Due to this motion, diffusivity in the x-y plane decreases. Similar reduced diffusivity is also observed in 2D plasma systems under the influence of a magnetic field.[30] Additionally, charged dimers exhibit reduced diffusivity, but only at short timescales.[32] In contrast, our results demonstrate a reduction in diffusion coefficient at large timescales.

We show $\Delta r_\perp^2$ in Figure 5.9(c) for varying field strengths. We observe that $\Delta r_\perp^2$ increases as field strength increases. We fit a straight line of the form $2D_z\Delta t$ to the $\Delta r_\parallel^2$ vs Δt data to determine the diffusion coefficient D_z in the direction parallel to the applied field. Figure 5.9(d) show D_z/D_z^0 data for different magnetic field. Here $D_z^0 = 0.0037\sigma^2/\tau$ is the diffusion coefficient of the chain in the field-free case. We find D_z increases as B increases. The increase in D_z may be attributed to magnetic field-induced orientation, where alignment along the field direction reduces steric hindrance along the z-axis, allowing the polymer to diffuse more freely in the field direction. Additionally, the restricted conformational freedom in the x-y plane may direct the translational motion of the polymer to become more dominant in the z-direction. This result is consistent with the observed diffusivity behavior in the experimental setups.[145, 146]

5.4 Conclusion

In this chapter, we study the effect of a magnetic field on the dynamics of a block polyampholyte chain. We investigate different polymer conformations for different magnetic field strengths. We find close-shaped chain conformations emerge as the field is applied. We also study different static quantities such as the radius of gyration and end-to-end distances of the polymer chain. We note that the radius of gyration decreases slightly as the field is applied, but remains unchanged as field strength increases. The end-to-end distances of the chain decrease monotonically with field strength. Furthermore, we compute the induced magnetic moment $\vec{\mu}$ of the chain in presence of the magnetic field. We find that $\vec{\mu}$ increases and aligns along the field direction as field strength increases. The reorientation time of the induced dipole moment vector, τ decreases with increasing field strength, which indicates the faster alignment of $\vec{\mu}$ along the field direction. We also observe that the chain diffusivity in the perpendicular plane of the applied field (x-y plane) decreases as field strength increases. The diffusivity along the field direction (z-direction) increases slightly with increasing field strength. This study is important for understanding the microscopic effects of magnetic fields on charged polymeric materials, which may have implications for various technological applications, such as engineering enhanced susceptibilities, controlling magnetic moments, and improving magnetic alignments of a polymeric sample.

Appendix

A5.1 Equations of motion incorporating external magnetic field

We solve the equation of motion derived from the modified Hamiltonian $H = \frac{(\vec{P}-q\vec{A})^2}{2m} + V(r)$ to incorporate the magnetic field in the simulation. Here $\vec{P}$ is the momentum, $\vec{A}$ is the magnetic vector potential and V is the potential energy.[33,35] In all cases, B is directed along the z-axis, hence $\vec{A} = -\frac{B}{2}y\hat{x} + \frac{B}{2}x\hat{y}$. Nose-Hoover thermostat is used to control the temperature during the simulation. The equation of motions for position and momentum are as follows:

$$\frac{dx_i}{dt} = \frac{p_i^x}{m_i} + \omega_i y_i; \qquad \frac{dp_i^x}{dt} = F_i^x + \omega_i(p_i^y - m_i\omega_i x_i) - \xi(p_i^x + m_i\omega_i y_i) \tag{A5.1.1}$$

$$\frac{dy_i}{dt} = \frac{p_i^y}{m_i} - \omega_i x_i; \qquad \frac{dp_i^y}{dt} = F_i^y - \omega_i(p_i^x - m_i\omega_i y_i) - \xi(p_i^y + m_i\omega_i x_i) \tag{A5.1.2}$$

$$\frac{dz_i}{dt} = \frac{p_i^z}{m_i}; \qquad \frac{dp_i^z}{dt} = F_i^z - \xi p_i^z \tag{A5.1.3}$$

$$\frac{dlns}{dt} = \xi; \qquad \frac{d\xi}{dt} = \frac{1}{\tau_{NH}^2}[\frac{K(\Gamma) - K^*}{K^*}] = \frac{\delta K(\Gamma)}{\tau_{NH}^2} \tag{A5.1.4}$$

Here, s and ξ are extended conjugate variables corresponding to the heat bath of the thermostat. τ_{NH} is the characteristic time of the thermostat, set at $\tau_{NH} = 20\tau$, τ being the time unit of our simulation. $K(\Gamma)$ is the kinetic energy during the simulation. K^* is the target kinetic energy given by $K^* = \frac{3}{2}Nk_BT$, N is the number of particles in the system, k_B is Boltzmann constant, T is the temperature of the system in the reduced unit.

Chapter 6 Outlook

In this thesis, we present a detailed study of the Hyaluronic acid (HA)-lipid bilayer complex, focusing on its structural and dynamic properties. We investigate the elastic response of the lipid bilayer to HA chains. Additionally, we analyze the interfacial dynamics at the HA-water and DPPC bilayer interfaces to understand how HA modulates the dynamical properties of these regions. The HA-lipid bilayer complex holds significant relevance in various biomedical contexts such as drug delivery, biomarkers for cancer detection, etc. Hence, these investigations are essential for deciphering the microscopic molecular mechanisms involved in disease progression and therapeutic resistance.

Nevertheless, in physiological conditions, HA chains are polydisperse, meaning they consist of varying chain lengths. Additionally, HA-degrading enzymes such as hyaluronidase are present in the extracellular matrix, while HA-receptor proteins like CD44 or RHAMM are located on the cell membrane. To better capture these biological complexities, the simulation model can be improved by incorporating these cellular components. Such improved simulation model would provide a more realistic representation of the HA-membrane environment. However, in these cases, atomistic simulations may become computationally expensive. To address this, coarse-grained models can be employed as a computationally efficient alternative.

Furthermore, we investigate the response of a polyampholyte (PA) chain to an external magnetic field, focusing on both its static and dynamic behavior. Polyampholytes, which contain both positively and negatively charged monomers, have significant importance in biological and industrial contexts. They are commonly used in applications such as developing low-friction materials, water purification systems, and responsive materials. The application of a magnetic field is often employed to enhance or modify the properties of polymeric materials. Our investigation may be helpful for designing polyampholyte-based systems with tunable properties tailored for specific applications. Instead of block arrangement, a random arrangement of charged beads along the chain can be considered to provide insights into designing charged copolymer sequences with desirable responses to a magnetic field. This approach can help guide the development of novel materials with tailored functionalities.

Additionally, model systems such as polyelectrolyte-polyampholyte complexes, polyampholyte brushes, or melts can be more representative of experimental conditions. These models would enable a closer comparison with real-world systems, providing a deeper understanding of the microscopic mechanisms and enhancing the applicability of the findings.

Bibliography

[1] A. S. Abdelsattar, Y. Mansour, and F. Aboul-ela, "The perturbed free-energy landscape: Linking ligand binding to biomolecular folding," *ChemBioChem*, vol. 22, no. 9, pp. 1499–1516, 2021.

[2] W. Wang, O. Donini, C. M. Reyes, and P. A. Kollman, "Biomolecular simulations: recent developments in force fields, simulations of enzyme catalysis, protein-ligand, protein-protein, and protein-nucleic acid noncovalent interactions," *Annual review of biophysics and biomolecular structure*, vol. 30, no. 1, pp. 211–243, 2001.

[3] L. Skjærven, N. Reuter, and A. Martinez, "Dynamics, flexibility and ligand-induced conformational changes in biological macromolecules: a computational approach," *Future Medicinal Chemistry*, vol. 3, no. 16, pp. 2079–2100, 2011.

[4] S. Panja and M. Halder, "Exploration of electrostatic interaction in the hydrophobic pocket of lysozyme: importance of ligand-induced perturbation of the secondary structure on the mode of binding of exogenous ligand and possible consequences," *Journal of Photochemistry and Photobiology B: Biology*, vol. 161, pp. 253–265, 2016.

[5] P. Patra, R. Banerjee, and J. Chakrabarti, "Effect of biphosphate salt on d ipalmitoylphosphatidylcholine bilayer deformation by tat polypeptide," *Biopolymers*, vol. 113, no. 8, p. e23518, 2022.

[6] E. N. Frigini, J. L. Cascales, and R. D. Porasso, "Molecular dynamics simulations of glyphosate in a dppc lipid bilayer," *Chemistry and physics of lipids*, vol. 213, pp. 111–117, 2018.

[7] W. Kopec, A. Zak, D. Jamróz, R. Nakahata, S.-i. Yusa, V. Gapsys, and M. Kepczynski, "Polycation–anionic lipid membrane interactions," *Langmuir*, vol. 36, no. 42, pp. 12435–12450, 2020.

[8] D. Bochicchio, L. Cantu, M. V. Cadario, L. Palchetti, F. Natali, L. Monticelli, G. Rossi, and E. Del Favero, "Polystyrene perturbs the structure, dynamics, and mechanical properties of dppc membranes: an experimental and computational study," *Journal of Colloid and Interface Science*, vol. 605, pp. 110–119, 2022.

[9] J. Eid, A. Jraij, H. Greige-Gerges, and L. Monticelli, "Effect of quercetin on lipid membrane rigidity: Assessment by atomic force microscopy and molecular dynamics simulations," *BBA advances*, vol. 1, p. 100018, 2021.

[10] M. Y. Laktionov, E. B. Zhulina, and O. V. Borisov, "Proteins and polyampholytes interacting with polyelectrolyte brushes and microgels: The charge reversal concept revised," *Langmuir*, vol. 37, no. 9, pp. 2865–2873, 2021.

[11] P. Liu, M. Hou, Y. Yue, Y. Tong, T. Zhang, Z. Lu, and L. Yang, "Effects of ultrahigh magnetic field on the structure and properties of whey protein," *Lwt*, vol. 177, p. 114590, 2023.

[12] S. M. Darwish, A. S. Darwish, and D. S. Darwish, "An extremely low-frequency magnetic field can affect creb protein conformation which may have a role in neuronal activities including memory," *Journal of Physics Communications*, vol. 4, no. 1, p. 015009, 2020.

[13] B. McCulloch, G. Portale, W. Bras, J. A. Pople, A. Hexemer, and R. A. Segalman, "Dynamics of magnetic alignment in rod–coil block copolymers," *Macromolecules*, vol. 46, no. 11, pp. 4462–4471, 2013.

[14] M. Gopinadhan, Y. Choo, K. Kawabata, G. Kaufman, X. Feng, X. Di, Y. Rokhlenko, L. H. Mahajan, D. Ndaya, R. M. Kasi, *et al.*, "Controlling orientational order in block copolymers using low-intensity magnetic fields," *Proceedings of the National Academy of Sciences*, vol. 114, no. 45, pp. E9437–E9444, 2017.

[15] M. Gopinadhan, P. W. Majewski, E. S. Beach, and C. O. Osuji, "Magnetic field alignment of a diblock copolymer using a supramolecular route," *ACS Macro Letters*, vol. 1, no. 1, pp. 184–189, 2012.

[16] X. Xu, A. K. Jha, D. A. Harrington, M. C. Farach-Carson, and X. Jia, "Hyaluronic acid-based hydrogels: from a natural polysaccharide to complex networks," *Soft matter*, vol. 8, no. 12, pp. 3280–3294, 2012.

[17] M. K. Cowman, H.-G. Lee, K. L. Schwertfeger, J. B. McCarthy, and E. A. Turley, "The content and size of hyaluronan in biological fluids and tissues," *Frontiers in immunology*, vol. 6, p. 261, 2015.

[18] K. L. Schwertfeger, M. K. Cowman, P. G. Telmer, E. A. Turley, and J. B. McCarthy, "Hyaluronan, inflammation, and breast cancer progression," *Frontiers in immunology*, vol. 6, p. 236, 2015.

[19] D. Paul, A. Paul, D. Mukherjee, S. Saroj, M. Ghosal, S. Pal, D. Senapati, J. Chakrabarti, S. K. Pal, and T. Rakshit, "A mechanoelastic glimpse on hyaluronan-

coated extracellular vesicles," *The Journal of Physical Chemistry Letters*, vol. 13, no. 36, pp. 8564–8572, 2022.

[20] Z. Cai, H. Zhang, Y. Wei, M. Wu, and A. Fu, "Shear-thinning hyaluronan-based fluid hydrogels to modulate viscoelastic properties of osteoarthritis synovial fluids," *Biomaterials science*, vol. 7, no. 8, pp. 3143–3157, 2019.

[21] W. Khuntawee, R. Amornloetwattana, W. Vongsangnak, K. Namdee, T. Yata, M. Karttunen, and J. Wong-Ekkabut, "In silico and in vitro design of cordycepin encapsulation in liposomes for colon cancer treatment," *RSC advances*, vol. 11, no. 15, pp. 8475–8484, 2021.

[22] J. Hunger, A. Bernecker, H. J. Bakker, M. Bonn, and R. P. Richter, "Hydration dynamics of hyaluronan and dextran," *Biophysical journal*, vol. 103, no. 1, pp. L10–L12, 2012.

[23] J. Dedic, H. Okur, and S. Roke, "Hyaluronan orders water molecules in its nanoscale extended hydration shells," *Science Advances*, vol. 7, no. 10, p. eabf2558, 2021.

[24] S. Pronk, E. Lindahl, and P. M. Kasson, "Dynamic heterogeneity controls diffusion and viscosity near biological interfaces," *Nature communications*, vol. 5, no. 1, p. 3034, 2014.

[25] E. Tendong, T. S. Dasgupta, and J. Chakrabarti, "Dynamics of water trapped in transition metal oxide-graphene nano-confinement," *Journal of Physics: Condensed Matter*, vol. 32, no. 32, p. 325101, 2020.

[26] S. Sengupta and S. Karmakar, "Distribution of diffusion constants and stokes-einstein violation in supercooled liquids," *The Journal of chemical physics*, vol. 140, no. 22, 2014.

[27] A. Paul and J. Chakrabarti, "Dynamics of an aqueous suspension of short hyaluronic acid chains near a dppc bilayer," *Phys. Chem. Chem. Phys.*, vol. 26, pp. 20440–20449, 2024.

[28] J. D. Jackson, *Classical electrodynamics*. John Wiley & Sons, 2021.

[29] Y. Rokhlenko, M. Gopinadhan, C. O. Osuji, K. Zhang, C. S. O'Hern, S. R. Larson, P. Gopalan, P. W. Majewski, and K. G. Yager, "Magnetic alignment of block copolymer microdomains by intrinsic chain anisotropy," *Physical Review Letters*, vol. 115, no. 25, p. 258302, 2015.

[30] T. Ott, H. Löwen, and M. Bonitz, "Dynamics of two-dimensional one-component and binary yukawa systems in a magnetic field," *Physical Review E*, vol. 89, no. 1, p. 013105, 2014.

[31] Y. Feng, J. Goree, B. Liu, T. Intrator, and M. Murillo, "Superdiffusion of two-dimensional yukawa liquids due to a perpendicular magnetic field," *Physical Review E*, vol. 90, no. 1, p. 013105, 2014.

[32] R. Shinde, J. U. Sommer, H. Löwen, and A. Sharma, "Strongly enhanced dynamics of a charged rouse dimer by an external magnetic field," *PNAS Nexus*, vol. 1, no. 3, p. pgac119, 2022.

[33] F. Mouhat, S. Bonella, and C. Pierleoni, "Charge transport simulations of nacl in an external magnetic field: the quest for the hall effect," *Molecular Physics*, vol. 111, no. 22-23, pp. 3651–3661, 2013.

[34] L. Gagliardi and S. Bonella, "Charge transport in superionic and melted agi under a magnetic field studied via molecular dynamics," *Physical Review B*, vol. 94, no. 13, p. 134426, 2016.

[35] A. Coretti, L. Rondoni, and S. Bonella, "Fluctuation relations for systems in a constant magnetic field," *Physical Review E*, vol. 102, no. 3, p. 030101, 2020.

[36] G. Kogan, L. Šoltés, R. Stern, J. Schiller, and R. Mendichi, "Hyaluronic acid: its function and degradation in in vivo systems," *Studies in natural products chemistry*, vol. 34, pp. 789–882, 2008.

[37] B. Delpech, N. Girard, P. Bertrand, M.-N. Courel, C. Chauzy, and A. Delpech, "Hyaluronan: fundamental principles and applications in cancer," *Journal of internal medicine*, vol. 242, no. 1, pp. 41–48, 1997.

[38] B. Delpech, N. Girard, A. Olivier, C. Maingonnat, G. van Driessche, J. van Beeumen, P. Bertrand, C. Duval, A. Delpech, and J. Bourguignon, "The origin of hyaluronectin in human tumors," *International journal of cancer*, vol. 72, no. 6, pp. 942–948, 1997.

[39] K. Rilla, H. Siiskonen, M. Tammi, and R. Tammi, "Hyaluronan-coated extracellular vesicles—a novel link between hyaluronan and cancer," *Advances in cancer research*, vol. 123, pp. 121–148, 2014.

[40] K.-H. Heider, M. Hofmann, E. Hors, F. van den Berg, H. Ponta, P. Herrlich, and S. T. Pals, "A human homologue of the rat metastasis-associated variant of cd44 is expressed in colorectal carcinomas and adenomatous polyps.," *The Journal of cell biology*, vol. 120, no. 1, pp. 227–233, 1993.

[41] G. Zhang, R. Lu, M. Wu, Y. Liu, Y. He, J. Xu, C. Yang, Y. Du, and F. Gao, “Colorectal cancer-associated˜ á6ákda hyaluronan serves as a novel biomarker for cancer progression and metastasis,” *The FEBS Journal*, vol. 286, no. 16, pp. 3148–3163, 2019.

[42] D. Paul, A. Roy, A. Nandy, B. Datta, P. Borar, S. K. Pal, D. Senapati, and T. Rakshit, “Identification of biomarker hyaluronan on colon cancer extracellular vesicles using correlative afm and spectroscopy,” *The Journal of Physical Chemistry Letters*, vol. 11, no. 14, pp. 5569–5576, 2020.

[43] H. L. Nguyen, V. H. Man, M. S. Li, P. Derreumaux, J. Wang, and P. H. Nguyen, “Elastic moduli of normal and cancer cell membranes revealed by molecular dynamics simulations,” *Physical Chemistry Chemical Physics*, vol. 24, no. 10, pp. 6225–6237, 2022.

[44] E. L. Wu, X. Cheng, S. Jo, H. Rui, K. C. Song, E. M. Dávila-Contreras, Y. Qi, J. Lee, V. Monje-Galvan, R. M. Venable, *et al.*, “Charmm-gui membrane builder toward realistic biological membrane simulations,” 2014.

[45] A. Almond, P. L. DeAngelis, and C. D. Blundell, “Hyaluronan: the local solution conformation determined by nmr and computer modeling is close to a contracted left-handed 4-fold helix,” *Journal of molecular biology*, vol. 358, no. 5, pp. 1256–1269, 2006.

[46] S.-J. Park, J. Lee, Y. Qi, N. R. Kern, H. S. Lee, S. Jo, I. Joung, K. Joo, J. Lee, and W. Im, “Charmm-gui glycan modeler for modeling and simulation of carbohydrates and glycoconjugates,” *Glycobiology*, vol. 29, no. 4, pp. 320–331, 2019.

[47] D. Van Der Spoel, E. Lindahl, B. Hess, G. Groenhof, A. E. Mark, and H. J. Berendsen, “Gromacs: fast, flexible, and free,” *Journal of computational chemistry*, vol. 26, no. 16, pp. 1701–1718, 2005.

[48] O. Guvench, S. S. Mallajosyula, E. P. Raman, E. Hatcher, K. Vanommeslaeghe, T. J. Foster, F. W. Jamison, and A. D. MacKerell Jr, “Charmm additive all-atom force field for carbohydrate derivatives and its utility in polysaccharide and carbohydrate–protein modeling,” *Journal of chemical theory and computation*, vol. 7, no. 10, pp. 3162–3180, 2011.

[49] D. J. Evans and B. L. Holian, “The nose–hoover thermostat,” *The Journal of chemical physics*, vol. 83, no. 8, pp. 4069–4074, 1985.

[50] M. Parrinello and A. Rahman, “Polymorphic transitions in single crystals: A new molecular dynamics method,” *Journal of Applied physics*, vol. 52, no. 12, pp. 7182–7190, 1981.

[51] U. Essmann, L. Perera, M. L. Berkowitz, T. Darden, H. Lee, and L. G. Pedersen, “A smooth particle mesh ewald method,” *The Journal of chemical physics*, vol. 103, no. 19, pp. 8577–8593, 1995.

[52] V. R. Hande and S. Chakrabarty, “How far is “bulk water” from interfaces? depends on the nature of the surface and what we measure,” *The Journal of Physical Chemistry B*, vol. 126, no. 5, pp. 1125–1135, 2022.

[53] R. M. Venable, F. L. Brown, and R. W. Pastor, “Mechanical properties of lipid bilayers from molecular dynamics simulation,” *Chemistry and physics of lipids*, vol. 192, pp. 60–74, 2015.

[54] P. W. Fowler, J. Hélie, A. Duncan, M. Chavent, H. Koldsø, and M. S. Sansom, “Membrane stiffness is modified by integral membrane proteins,” *Soft Matter*, vol. 12, no. 37, pp. 7792–7803, 2016.

[55] Z. A. Levine, R. M. Venable, M. C. Watson, M. G. Lerner, J.-E. Shea, R. W. Pastor, and F. L. Brown, “Determination of biomembrane bending moduli in fully atomistic simulations,” *Journal of the American Chemical Society*, vol. 136, no. 39, pp. 13582–13585, 2014.

[56] P.-L. Chau and A. Hardwick, “A new order parameter for tetrahedral configurations,” *Molecular Physics*, vol. 93, no. 3, pp. 511–518, 1998.

[57] C.-J. Högberg and A. P. Lyubartsev, “A molecular dynamics investigation of the influence of hydration and temperature on structural and dynamical properties of a dimyristoylphosphatidylcholine bilayer,” *The Journal of Physical Chemistry B*, vol. 110, no. 29, pp. 14326–14336, 2006.

[58] S. Malik, S. Karmakar, and A. Debnath, “Relaxation time scales of interfacial water upon fluid to ripple to gel phase transitions of bilayers,” *The Journal of Chemical Physics*, vol. 158, no. 11, 2023.

[59] P. Smith, R. M. Ziolek, E. Gazzarrini, D. M. Owen, and C. D. Lorenz, “On the interaction of hyaluronic acid with synovial fluid lipid membranes,” *Physical Chemistry Chemical Physics*, vol. 21, no. 19, pp. 9845–9857, 2019.

[60] D. Drabik, G. Chodaczek, S. Kraszewski, and M. Langner, “Mechanical properties determination of dmpc, dppc, dspc, and hspc solid-ordered bilayers,” *Langmuir*, vol. 36, no. 14, pp. 3826–3835, 2020.

[61] E. Deplazes, F. Sarrami, and D. Poger, “Effect of h3o+ on the structure and dynamics of water at the interface with phospholipid bilayers,” *The Journal of Physical Chemistry B*, vol. 124, no. 8, pp. 1361–1373, 2020.

[62] N. H. Rhys, D. J. Barlow, M. J. Lawrence, and C. D. Lorenz, "On the interactions of diols and dmpc monolayers," *Journal of Molecular Liquids*, vol. 364, p. 119963, 2022.

[63] M. P. Allen and D. J. Tildesley, *Computer simulation of liquids*. Oxford university press, 2017.

[64] H. J. Berendsen, J. v. Postma, W. F. Van Gunsteren, A. DiNola, and J. R. Haak, "Molecular dynamics with coupling to an external bath," *The Journal of chemical physics*, vol. 81, no. 8, pp. 3684–3690, 1984.

[65] H. K. Vincent, S. S. Percival, B. P. Conrad, A. N. Seay, C. Montero, and K. R. Vincent, "Hyaluronic acid (ha) viscosupplementation on synovial fluid inflammation in knee osteoarthritis: a pilot study," *The open orthopaedics journal*, vol. 7, p. 378, 2013.

[66] C. Liu, M. Wang, J. An, E. Thormann, and A. Dėdinaitė, "Hyaluronan and phospholipids in boundary lubrication," *Soft Matter*, vol. 8, no. 40, pp. 10241–10244, 2012.

[67] J. Seror, L. Zhu, R. Goldberg, A. J. Day, and J. Klein, "Supramolecular synergy in the boundary lubrication of synovial joints," *Nature communications*, vol. 6, no. 1, p. 6497, 2015.

[68] H. Zhang, W. Cai, and X. Shao, "Regulation of aquaporin-3 water permeability by hyaluronan," *Physical Chemistry Chemical Physics*, vol. 23, no. 45, pp. 25706–25711, 2021.

[69] M. K. Cowman, T. A. Schmidt, P. Raghavan, and A. Stecco, "Viscoelastic properties of hyaluronan in physiological conditions," *F1000Research*, vol. 4, 2015.

[70] A. Debnath, B. Mukherjee, K. Ayappa, P. K. Maiti, and S.-T. Lin, "Entropy and dynamics of water in hydration layers of a bilayer," *The Journal of Chemical Physics*, vol. 133, no. 17, p. 174704, 2010.

[71] S. W. Siu, R. Vácha, P. Jungwirth, and R. A. Böckmann, "Biomolecular simulations of membranes: physical properties from different force fields," *The Journal of chemical physics*, vol. 128, no. 12, 2008.

[72] R. M. Venable, H. I. Ingólfsson, M. G. Lerner, B. S. Perrin Jr, B. A. Camley, S. J. Marrink, F. L. Brown, and R. W. Pastor, "Lipid and peptide diffusion in bilayers: The saffman–delbruck model and periodic boundary conditions," *The Journal of Physical Chemistry B*, vol. 121, no. 15, pp. 3443–3457, 2017.

[73] M. G. Mazza, N. Giovambattista, F. W. Starr, and H. E. Stanley, "Relation between rotational and translational dynamic heterogeneities in water," *Physical review letters*, vol. 96, no. 5, p. 057803, 2006.

[74] P. B. Moore, C. F. Lopez, and M. L. Klein, “Dynamical properties of a hydrated lipid bilayer from a multinanosecond molecular dynamics simulation,” *Biophysical journal*, vol. 81, no. 5, pp. 2484–2494, 2001.

[75] M. G. Mazza, N. Giovambattista, H. E. Stanley, and F. W. Starr, “Connection of translational and rotational dynamical heterogeneities with the breakdown of the stokes-einstein and stokes-einstein-debye relations in water,” *Physical Review E*, vol. 76, no. 3, p. 031203, 2007.

[76] Q. Zhang, T. Wu, C. Chen, S. Mukamel, and W. Zhuang, “Molecular mechanism of water reorientational slowing down in concentrated ionic solutions,” *Proceedings of the National Academy of Sciences*, vol. 114, no. 38, pp. 10023–10028, 2017.

[77] T. G. Lombardo, P. G. Debenedetti, and F. H. Stillinger, “Computational probes of molecular motion in the lewis-wahnström model for ortho-terphenyl,” *The Journal of chemical physics*, vol. 125, no. 17, p. 174507, 2006.

[78] `https://www.geol.lsu.edu/jlorenzo/geophysics/uncertainties/Uncertaintiespart2.html`.

[79] R. Karmakar, A. Ghosal, and J. Chakrabarti, “Model studies on motion of respiratory droplets driven through a face mask,” *Europhysics Letters*, 2022.

[80] A. Nikoubashman, A. Milchev, and K. Binder, “Dynamics of single semiflexible polymers in dilute solution,” *The Journal of Chemical Physics*, vol. 145, no. 23, p. 234903, 2016.

[81] K. Sinha, A. Kumawat, and S. Chakrabarty, “Elucidating the microscopic origin of observed anti-correlation between the protein-protein and protein-water interaction energies,” *Chemical Physics Impact*, vol. 8, p. 100421, 2024.

[82] E. Yamamoto, T. Akimoto, M. Yasui, and K. Yasuoka, “Origin of subdiffusion of water molecules on cell membrane surfaces,” *Scientific reports*, vol. 4, no. 1, p. 4720, 2014.

[83] J.-P. Hansen and I. R. McDonald, *Theory of simple liquids: with applications to soft matter*. Academic press, 2013.

[84] E. J. Maginn, R. A. Messerly, D. J. Carlson, D. R. Roe, and J. R. Elliot, “Best practices for computing transport properties 1. self-diffusivity and viscosity from equilibrium molecular dynamics [article v1. 0],” *Living Journal of Computational Molecular Science*, vol. 1, no. 1, pp. 6324–6324, 2019.

[85] M. Javanainen, H. Hammaren, L. Monticelli, J.-H. Jeon, M. S. Miettinen, H. Martinez-Seara, R. Metzler, and I. Vattulainen, “Anomalous and normal

diffusion of proteins and lipids in crowded lipid membranes," *Faraday discussions*, vol. 161, pp. 397–417, 2013.

[86] J. Kapla, J. Wohlert, B. Stevensson, O. Engstrom, G. Widmalm, and A. Maliniak, "Molecular dynamics simulations of membrane–sugar interactions," *The Journal of Physical Chemistry B*, vol. 117, no. 22, pp. 6667–6673, 2013.

[87] G. van den Bogaart, N. Hermans, V. Krasnikov, A. H. de Vries, and B. Poolman, "On the decrease in lateral mobility of phospholipids by sugars," *Biophysical journal*, vol. 92, no. 5, pp. 1598–1605, 2007.

[88] S. S. Stachura, C. J. Malajczuk, and R. L. Mancera, "Does sucrose change its mechanism of stabilization of lipid bilayers during desiccation? influences of hydration and concentration," *Langmuir*, vol. 35, no. 47, pp. 15389–15400, 2019.

[89] X. Lin, V. Nair, Y. Zhou, and A. A. Gorfe, "Membrane potential and dynamics in a ternary lipid mixture: Insights from molecular dynamics simulations," *Physical Chemistry Chemical Physics*, vol. 20, no. 23, pp. 15841–15851, 2018.

[90] M. Rubinstein and R. H. Colby, *Polymer physics*. Oxford university press, 2003.

[91] T. Fujiyabu, X. Li, U.-i. Chung, and T. Sakai, "Diffusion behavior of water molecules in hydrogels with controlled network structure," *Macromolecules*, vol. 52, no. 5, pp. 1923–1929, 2019.

[92] F. Burla, T. Sentjabrskaja, G. Pletikapic, J. Van Beugen, and G. H. Koenderink, "Particle diffusion in extracellular hydrogels," *Soft Matter*, vol. 16, no. 5, pp. 1366–1376, 2020.

[93] S. A. Roget, Z. A. Piskulich, W. H. Thompson, and M. D. Fayer, "Identical water dynamics in acrylamide hydrogels, polymers, and monomers in solution: ultrafast ir spectroscopy and molecular dynamics simulations," *Journal of the American Chemical Society*, vol. 143, no. 36, pp. 14855–14868, 2021.

[94] C.-M. Chang, Y.-G. Lau, S.-C. Ou, T.-Y. Lin, and W.-T. Juan, "Anomalous diffusion of dna on a supported cationic lipid membrane," *Europhysics Letters*, vol. 109, no. 3, p. 38002, 2015.

[95] S. Yu, J. Zhao, R. Chu, X. Li, G. Wu, and X. Meng, "Anomalous diffusion of polyelectrolyte segments on supported charged lipid bilayers," *Entropy*, vol. 25, no. 5, p. 796, 2023.

[96] T. Zander, V. M. Garamus, A. Dédinaité, P. M. Claesson, P. Bełdowski, K. Górny, Z. Dendzik, D. F. Wieland, and R. Willumeit-Römer, "Influence of the molecular

weight and the presence of calcium ions on the molecular interaction of hyaluronan and dppc," *Molecules*, vol. 25, no. 17, p. 3907, 2020.

[97] D. Cosco, N. Tsapis, T. L. Nascimento, M. Fresta, D. Chapron, M. Taverna, S. Arpicco, and E. Fattal, "Polysaccharide-coated liposomes by post-insertion of a hyaluronan-lipid conjugate," *Colloids and Surfaces B: Biointerfaces*, vol. 158, pp. 119–126, 2017.

[98] L. M. Negi, M. Jaggi, V. Joshi, K. Ronodip, and S. Talegaonkar, "Hyaluronan coated liposomes as the intravenous platform for delivery of imatinib mesylate in mdr colon cancer," *International journal of biological macromolecules*, vol. 73, pp. 222–235, 2015.

[99] M. Manconi, M. L. Manca, D. Valenti, E. Escribano, H. Hillaireau, A. M. Fadda, and E. Fattal, "Chitosan and hyaluronan coated liposomes for pulmonary administration of curcumin," *International journal of pharmaceutics*, vol. 525, no. 1, pp. 203–210, 2017.

[100] K. J. Wolf and S. Kumar, "Hyaluronic acid: incorporating the bio into the material," *ACS biomaterials science & engineering*, vol. 5, no. 8, pp. 3753–3765, 2019.

[101] G. G. G. Perera, D. F. Argenta, and T. Caon, "The rheology of injectable hyaluronic acid hydrogels used as facial fillers: A review," *International Journal of Biological Macromolecules*, p. 131880, 2024.

[102] S. Shakibi, P. R. Onck, and E. Van der Giessen, "A one-bead-per-saccharide (1bps) model for glycosaminoglycans," *Journal of Chemical Theory and Computation*, vol. 19, no. 16, pp. 5491–5502, 2023.

[103] S. A. Samsonov, L. Bichmann, and M. T. Pisabarro, "Coarse-grained model of glycosaminoglycans," *Journal of Chemical Information and Modeling*, vol. 55, no. 1, pp. 114–124, 2015.

[104] D. Laage, T. Elsaesser, and J. T. Hynes, "Water dynamics in the hydration shells of biomolecules," *Chemical Reviews*, vol. 117, no. 16, pp. 10694–10725, 2017.

[105] S. Mondal, K. P. Ghanta, and S. Bandyopadhyay, "Dynamic heterogeneity at the interface of an intrinsically disordered peptide," *Journal of Chemical Information and Modeling*, vol. 62, no. 8, pp. 1942–1955, 2022.

[106] S.-H. Chong and S. Ham, "Anomalous dynamics of water confined in protein–protein and protein–dna interfaces," *The journal of physical chemistry letters*, vol. 7, no. 19, pp. 3967–3972, 2016.

[107] A. Srivastava, S. Malik, and A. Debnath, "Heterogeneity in structure and dynamics of water near bilayers using tip3p and tip4p/2005 water models," *Chemical Physics*, vol. 525, p. 110396, 2019.

[108] M. Karzar Jeddi and S. Romero-Vargas Castrillon, "Dynamics of water monolayers confined by chemically heterogeneous surfaces: Observation of surface-induced anisotropic diffusion," *The Journal of Physical Chemistry B*, vol. 121, no. 41, pp. 9666–9675, 2017.

[109] S. Dutta and J. Chakrabarti, "Anomalous dynamical responses in a driven system," *Europhysics Letters*, vol. 116, no. 3, p. 38001, 2016.

[110] B. Wang, J. Kuo, S. C. Bae, and S. Granick, "When brownian diffusion is not gaussian," *Nature materials*, vol. 11, no. 6, pp. 481–485, 2012.

[111] S. Dutta and J. Chakrabarti, "Transient dynamical responses of a charged binary colloid in an electric field," *Soft Matter*, vol. 14, no. 22, pp. 4477–4482, 2018.

[112] A. Cuetos, N. Morillo, and A. Patti, "Fickian yet non-gaussian diffusion is not ubiquitous in soft matter," *Physical Review E*, vol. 98, no. 4, p. 042129, 2018.

[113] S. Dutta, M. Ghosh, R. Karmakar, and J. Chakrabarti, "Dynamic signature of ligand binding over a protein surface," *Physical Review E*, vol. 100, no. 6, p. 062411, 2019.

[114] W. H. Press, *Numerical recipes in Fortran 77: the art of scientific computing*. Cambridge university press, 1992.

[115] L. B. Lucy, "An iterative technique for the rectification of observed distributions," *Astronomical Journal, Vol. 79, p. 745 (1974)*, vol. 79, p. 745, 1974.

[116] E. Tendong, T. Saha-Dasgupta, and J. Chakrabarti, "Viscoelastic response of fluid trapped between two dissimilar van der waals surfaces," *Journal of Physics: Condensed Matter*, vol. 34, no. 19, p. 195101, 2022.

[117] Z. Zhang and G. F. Christopher, "The nonlinear viscoelasticity of hyaluronic acid and its role in joint lubrication," *Soft Matter*, vol. 11, no. 13, pp. 2596–2603, 2015.

[118] Z. Liu, W. Lin, Y. Fan, N. Kampf, Y. Wang, and J. Klein, "Effects of hyaluronan molecular weight on the lubrication of cartilage-emulating boundary layers," *Biomacromolecules*, vol. 21, no. 10, pp. 4345–4354, 2020.

[119] C. Tanford, *Physical chemistry of macromolecules*. John Wiley & Sons, Incorporated, 1966.

[120] E. A. Bekturov, S. E. Kudaibergenov, and S. R. Rafikov, “Synthetic polymeric ampholytes in solution,” *Journal of Macromolecular Science—Reviews in Macromolecular Chemistry and Physics*, vol. 30, no. 2, pp. 233–303, 1990.

[121] A. V. Dobrynin, R. H. Colby, and M. Rubinstein, “Polyampholytes,” *Journal of Polymer Science Part B: Polymer Physics*, vol. 42, no. 19, pp. 3513–3538, 2004.

[122] M. Hara, *Polyelectrolytes: science and technology*. CRC Press, 1992.

[123] A. E. Neitzel, G. X. De Hoe, and M. V. Tirrell, “Expanding the structural diversity of polyelectrolyte complexes and polyzwitterions,” *Current Opinion in Solid State and Materials Science*, vol. 25, no. 2, p. 100897, 2021.

[124] M. Chen, W. H. Briscoe, S. P. Armes, and J. Klein, “Lubrication at physiological pressures by polyzwitterionic brushes,” *science*, vol. 323, no. 5922, pp. 1698–1701, 2009.

[125] J. Koc, E. Schonemann, A. Amuthalingam, J. Clarke, J. A. Finlay, A. S. Clare, A. Laschewsky, and A. Rosenhahn, “Low-fouling thin hydrogel coatings made of photo-cross-linked polyzwitterions,” *Langmuir*, vol. 35, no. 5, pp. 1552–1562, 2018.

[126] P. Mary, D. D. Bendejacq, M.-P. Labeau, and P. Dupuis, “Reconciling low-and high-salt solution behavior of sulfobetaine polyzwitterions,” *The Journal of Physical Chemistry B*, vol. 111, no. 27, pp. 7767–7777, 2007.

[127] K. S. Silmore and R. Kumar, “Dynamics of a single polyampholyte chain,” *The Journal of Chemical Physics*, vol. 155, no. 21, 2021.

[128] I. De Vlaminck and C. Dekker, “Recent advances in magnetic tweezers,” *Annual review of biophysics*, vol. 41, no. 1, pp. 453–472, 2012.

[129] C. Guo and L. J. Kaufman, “Flow and magnetic field induced collagen alignment,” *Biomaterials*, vol. 28, no. 6, pp. 1105–1114, 2007.

[130] Y. Sahoo, M. Cheon, S. Wang, H. Luo, E. Furlani, and P. Prasad, “Field-directed self-assembly of magnetic nanoparticles,” *The Journal of Physical Chemistry B*, vol. 108, no. 11, pp. 3380–3383, 2004.

[131] T. Ott and M. Bonitz, “Diffusion in a strongly coupled magnetized plasma,” *Physical review letters*, vol. 107, no. 13, p. 135003, 2011.

[132] T. Ott, M. Bonitz, and Z. Donkó, “Effect of correlations on heat transport in a magnetized strongly coupled plasma,” *Phys. Rev. E*, vol. 92, p. 063105, Dec 2015.

[133] B. Bernu, “Single-particle motion in the strongly coupled one-component plasma,” *Journal of Statistical Physics*, vol. 21, pp. 447–464, 1979.

[134] R. Johnson and S. Ranganathan, “Exact algorithm for dynamics of charged particles in a magnetic field,” *Physics and Chemistry of Liquids*, vol. 40, no. 5, pp. 527–538, 2002.

[135] “Classical molecular dynamics simulation with the velocity verlet algorithm at strong external magnetic fields,” *Journal of Computational Physics*, vol. 152, no. 1, pp. 102–119, 1999.

[136] D. P. Foster and D. Majumdar, “Critical behavior of magnetic polymers in two and three dimensions,” *Physical Review E*, vol. 104, no. 2, p. 024122, 2021.

[137] A. U. Mahmood and Y. G. Yingling, “All-atom simulation method for zeeman alignment and dipolar assembly of magnetic nanoparticles,” *Journal of Chemical Theory and Computation*, vol. 18, no. 5, pp. 3122–3135, 2022.

[138] R. Karmakar and J. Chakrabarti, “Transport of particles through ro membrane in steady state condition,” *ChemistrySelect*, vol. 9, no. 6, p. e202304343, 2024.

[139] S. Dutta and J. Chakrabarti, “Length-scales of dynamic heterogeneity in a driven binary colloid,” *Physical Chemistry Chemical Physics*, vol. 22, no. 31, pp. 17731–17737, 2020.

[140] P. Tillman, “Determination of nutrient values for commercial amino acids,” *Journal of Applied Poultry Research*, vol. 28, no. 3, pp. 526–530, 2019.

[141] P. Ahlrichs and B. Dünweg, “Simulation of a single polymer chain in solution by combining lattice boltzmann and molecular dynamics,” *The Journal of chemical physics*, vol. 111, no. 17, pp. 8225–8239, 1999.

[142] R. Chang and A. Yethiraj, “Solvent effects on the collapse dynamics of polymers,” *The Journal of Chemical Physics*, vol. 114, no. 17, pp. 7688–7699, 2001.

[143] R. Chang and A. Yethiraj, “Strongly charged flexible polyelectrolytes in poor solvents: Molecular dynamics simulations with explicit solvent,” *The Journal of chemical physics*, vol. 118, no. 14, pp. 6634–6647, 2003.

[144] N. Todorova, A. Bentvelzen, and I. Yarovsky, “Electromagnetic field modulates aggregation propensity of amyloid peptides,” *The Journal of Chemical Physics*, vol. 152, no. 3, p. 035104, 2020.

[145] S.-J. Wang, Y. Wu, X. Zhao, and L. Zuo, “Effect of a high magnetic field on carbon diffusion in γ-iron,” *Materials transactions*, vol. 52, no. 2, pp. 139–141, 2011.

[146] T. Takahashi, T. Ohkubo, and Y. Ikeda, “Montmorillonite alignment induced by magnetic field: Evidence based on the diffusion anisotropy of water molecules,” *Journal of colloid and interface science*, vol. 299, no. 1, pp. 198–203, 2006.